POLITECNICO
MILANO 1863

School of Industrial and Information Engineering
Department of Chemistry, Materials and Chemical Engineering "Giulio Natta"
Master of Science in Materials Engineering and Nanotechnology

Synthesis and characterization of thermotropic liquid crystalline halide perovskites based on fluorinated imidazolium cations

Author: Leonardo Leccioli
Student ID: 966410

Advisor: Prof. Gabriella Cavallo
Co-Advisor: Dr. Anastasios Stergiou

Academic year 2021-2022

Abstract

In recent years, perovskites have found use in numerous fields beginning with photovoltaics and expanding to light-emitting applications and other optoelectronic devices. Despite the competing costs and efficiencies of perovskite-based devices,toxicity issues related to lead-based halide perovskites together with their poor stability in air and moisture still represent the main factors limiting their marketing. It is generally accepted that the presence of defects, both at the surface or in the bulk, is critical for the long-term stability and considerably limits perovskite efficiency. Several strategies have been developed to overcome these limits. Among them, the use of ionic liquids (ILs) as additives to perovskite precursor solution allows to improve the crystallinity of the perovskite, passivate surface structural defects, block non-radiative recombination of the photogenerated ion pairs and impede atmospheric-induced degradation. In particular, perfluoroalkyl-methyl imidazolium ILs have been applied as passivating agents due to their ability to self-assemble on perovskite surface, resulting in the formation of ordered structures and higher film quality with fewer defects. In this work imidazolium cations functionalized with linear or branched perfluoroalkyl chains were applied for the synthesis of new Low Dimensional Halide Perovskites (LDHPs). Fluorination of organic cations offers an intriguing strategy to adjust the optoelectronic properties of LDHPs. In fact, the presence of highly fluorinated saturated molecular fragments in the resulting LDHPs can bestow additional water-repellent properties and superior stability compared to fully hydrocarbon-based cations previously employed. However, to completely exploit the benefits of fluorination in tailoring the physical and functional properties of perovskites, it is essential to better understand how fluorinated ionic liquids influence structure-property relationship. Here a combination of structural and thermal characterization allowed to study effects of perfluoroalkyl chains on the properties of perovskites. Indeed, fluorous-fluorous interactions and segregation of fluorinated moieties have been demonstrated to induce the formation of ordered structures in perovskite containing fluorinated imidazolium cations, resulting in a thermotropic liquid crystalline (LC) behavior.

Keywords: Low dimensional halide perovskites, ionic liquids, liquid-crystals, fluorous-fluorous interactions

Abstract in lingua italiana

Attualmente le perovskiti vengono utilizzate in numerosi campi a partire dal fotovoltaico sino a molteplici applicazioni nei dispositivi optoelettronici. Nonostante la riduzione dei costi e l'ottima efficienza dei dispositivi a base di perovskite, le problematiche di tossicità legate alla presenza del piombo e la scarsa stabilità rappresentano ancora i principali fattori limitanti per la loro commercializzazione. La presenza di difetti, sia in superficie che all'interno del materiale, è nota essere critica per la stabilità a lungo termine e considerevolmente limitante all'efficienza della perovskite. Affinché vengano superati questi limiti sono state sviluppate diverse strategie. Tra queste l'utilizzo di liquidi ionici (ILs) come additivi consente di migliorare la cristallinità della perovskite, passivare i difetti strutturali superficiali, bloccare la ricombinazione non radiativa degli eccitoni foto-generati e migliorare la stabilità contro gli agenti atmosferici. In particolare, i liquidi ionici a base di perfluoroalchil-metil-imidazolo sono stati applicati come agenti passivanti grazie alla loro capacità di auto-assemblarsi sulla superficie della perovskite, portando alla formazione di strutture ordinate con minori difetti. In questo lavoro cationi di imidazolo funzionalizzati con catene perfluoroalchil lineari o ramificate sono stati impiegati per la sintesi di nuove perovskiti a bassa dimensionalità con alogeno (LDHPs). I cationi organici florurati sono considerati un metodo innovativo per regolare le proprietà optoelettroniche delle LDHP. La presenza di frammenti molecolari saturi altamente fluorurati nelle LDHP può conferire proprietà idrorepellenti e una stabilità maggiore. Tuttavia, per sfruttare interamente i vantaggi della florurazone nelle perovskiti, è essenziale comprendere meglio come i liquidi ionici fluorurati influiscano sulla struttura e dunque sulle proprietà del materiale. In questo lavoro è stata effettuata una caratterizzazione strutturale e termica che ha permesso di studiare gli effetti delle catene perfluoroalchilche nelle proprietà delle perovskiti. Infatti è stato dimostrato che le interazioni fluoro-fluoro e la segregazione delle porzioni fluorurate inducono alla formazione di strutture ordinate lamellari nelle perovskiti, dando luogo a un comportamento termotropico liquido cristallino (LC).

Parole chiave: Perovskiti a bassa dimensionalità con alogeno, liquidi ionici, cristalli liquidi, interazioni fluoro-fluoro

Contents

1 | Introduction

After two years of COVID-19 pandemic, the world was hoping for a green recovery as referred by president Joe Biden in his "Build Back Better Framework" [1]. Nevertheless, there has been no global energy transition yet. Projects using renewable energy were postponed in 2021 as a result of pandemic aftershocks, supply chain disruptions, and an increase in commodity prices. Additionally, a recovery in economic activity caused global energy consumption to rise by almost 4%, with fossil fuels providing the majority of that energy, which resulted in record-high carbon dioxide emissions [2]. An unprecedented global energy crisis and commodities shock were caused by the leap in energy prices in the second half of the year, which was followed by the Russian Federation's invasion of Ukraine in early 2022. Governments have responded by putting temporary measures in place to reduce price increases. Due to this circumstance, there are now more urgent climate disasters as well as geopolitical and economic concerns in the world [2]. Moreover, the methane crisis related to the war happening in Ukraine has highlighted how deeply the current society is relying on fossil fuel resources. For this reason the present fossil fuel-based energy system is in crisis, making urgent the need to switch to renewable energy sources in all spheres of society and business. For a more reliable, resilient, affordable and sustainable energy system, only an economy based on renewable and efficient energy sources can alter the current situation [2]. In this scenario, decarbonization, referred to as low-carbon economy, has evolved over the past ten years into a global objective that has sparked the creation of affordable and dependable fossil fuel substitutes. According to last year forecasts based on the sustainable development objectives, solar energy will dominate the expansion of renewable energies in the ensuing years [3]. The silicon-based PV modules, which use the indirect interband transition to transform visible light into useable electrical energy, account for a huge proportion of today's solar energy generation. Even if they are economically advantageous in comparison to their competitors, conventional PV cells have a significant disadvantage due to their limited maximum efficiency.
Recent advancements in the field of perovskite photovoltaics have garnered significant interest from the scientific community, primarily due to the extraordinary light-absorbing properties of these hybrid inorganic–organic materials. One of the primary benefits of

perovskites is their ability to be processed from solutions at relatively low temperatures, resulting in significant cost savings when compared to solar cells made from silicon. In just three years, the reported photoconversion efficiencies of such devices increased from 3.8% to over 25%, with further increases anticipated in the near future. In light of this, there is no doubt that perovskite photovoltaics have the potential to provide a promising future for research in the field of solar cells [4, 5].

The rapid progress of perovskites in photovoltaics has attracted the interest of scientists from a variety of disciplines, and the initial excitement has been bolstered by research into the structural, optical, and electronic properties of perovskites. Perovskites combine the properties of inorganic and organic semiconductors: the chemical tunability of their optoelectronic properties and solution-based deposition recall organics; their relatively high carrier mobility, diffusion length, and radiative lifetime more closely resemble those of polycrystalline semiconductors. These attractive properties have inspired visions that extend far beyond photovoltaics, and research is already underway in sunlight-to-fuel conversion, light-emitting diodes, lasers, and photodetectors [6].

The investigation of the relationship between these materials' properties and structures could lead to a better understanding of how they function and the removal of the obstacles that presently prevent their commercialization. Thus, performance could be enhanced and novel materials whose properties can be determined and controlled by varying the material's composition could be created. This paper provides an overview of the current state of hybrid halide perovskites, as well as their various applications and limitations. Then, low-dimensional perovskites were investigated as an alternative, and the significance of the effect of fluorinated organic cations was examined as a promising alternative. Specifically, the objective of the experimental work is to use fluorinated organic cations in the synthesis of novel types of low dimensional perovskites in order to control the self-assembly and physico-chemical properties of the material and to enhance its resistance to atmospheric agents.

1.1. Perovskite materials

In general, the term "*perovskite*" refers to a mineral species composed of calcium titanate with the chemical formula $CaTiO_3$. Gustav Rose discovered the mineral in the Ural Mountains of Russia in 1839; it is named after by the Russian mineralogist Lev Perovski. Later, the term was applied to any substance with the same crystalline structure as calcium titanium oxide, ABX_3, where A and B are cations (with A typically being larger than B) and X is an anion. In the ideal cubic structure, the B cation has 6-fold coordination and is enveloped by an octahedron of anions. The A cation is in 12-fold cuboctahedral coordination [7].

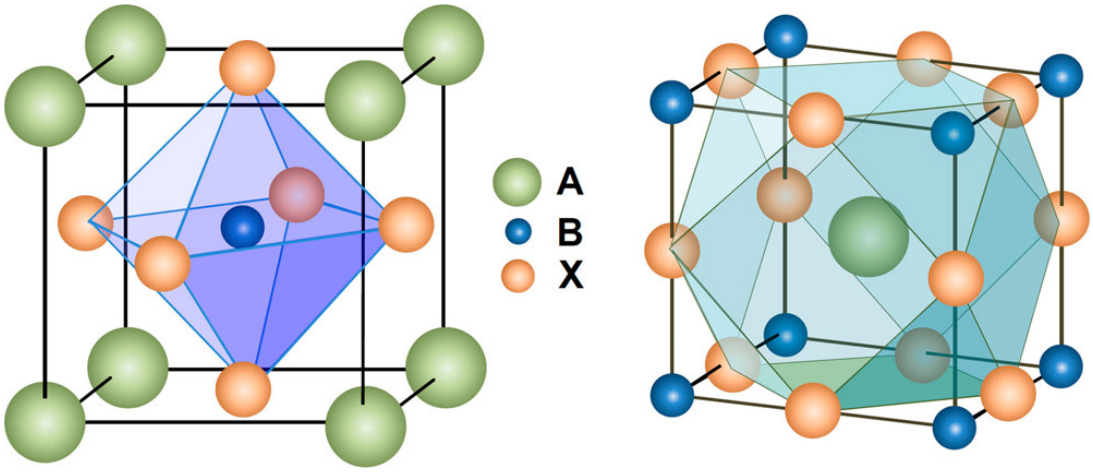

Figure 1.1: ABX_3 perovskite structure showing (left) BX_6 octahedral and (right) AX_{12} cuboctahedral geometry [8].

A preliminary classification can be made by taking into account their chemical nature since many different elements can be mixed to generate perovskite structures. *Halide perovskites* are based on halide anions, such as Cl^-, Br−, or I^-, while *inorganic oxide perovskites* contain O^{2-} anions, just like the original mineral. In the periodic table, B is often a bivalent cation from the IV group, like Ge, Sn, or Pb, whereas A is a monovalent cation from the I group, like K, Rb, or Cs (giving the name of *alkali-halide perovskites*), or an organic molecule (providing *organo-metal halide perovskites*). The relative ion size requirements for stability of the cubic structure are quite stringent, so slight buckling and distortion can produce multiple versions with lower symmetry, in which the coordination numbers of A cations, B cations, or both are reduced. Many of the perovskite's physical properties, such as the electronic, magnetic, and dielectric properties, which are crucial for numerous perovskite applications, depend on the specifics of these distortions. For instance, the distortions caused by cation substitution can be utilized to fine-tune the

physical properties of perovskites. In addition, the selection of each of these components will affect the material's qualities and structure. For a fixed B cation, for instance, a larger halogen will result in a higher lattice parameter and a more covalent character in the B-X bond due to the halogen's lower electronegativity. Consequently, the band gap decreases and the absorption spectrum shifts toward the red. Lead is frequently chosen for its material stability and device efficacy, despite its toxicity raising concerns. Thus, current research focuses on substituting Sn or Ge for Pb to avoid this drawback [9]. The A cation is the species whose chemical-physical characteristics and crystal structure are most amenable to modification. Utilizing organic cations of different diameters, for instance, enables the formation of perovskites with lower dimensionality (i.e., 2D, 1D, or 0D), which has intriguing implications for the material's properties [7, 10].

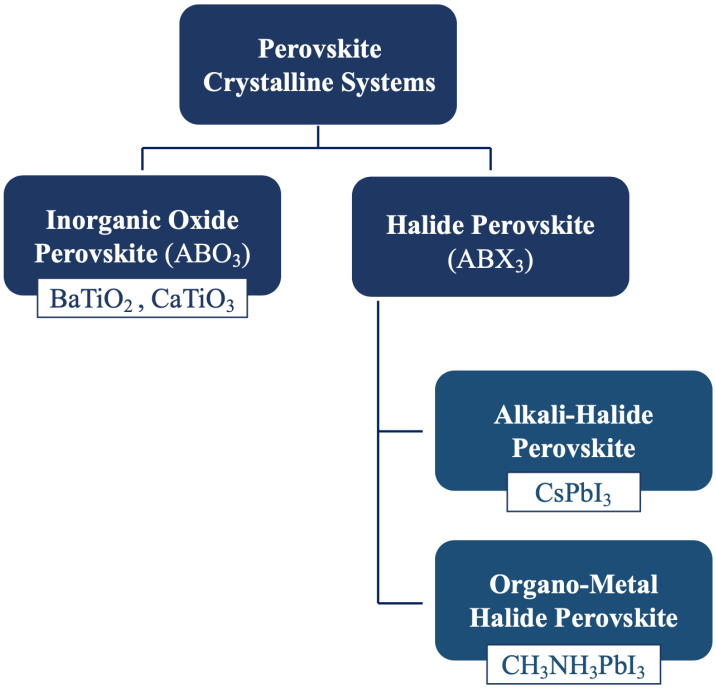

Figure 1.2: Classification of perovskites based on their composition.

1.1.1. Geometrical parameters

Since the composition of the perovskite crystal structure is very flexible, the structural probability and crystallographic stability of the structure can be evaluated by the Goldschmidt tolerance factor (t), which is defined as the ratio of the distance A–X to B–X in an idealized solid-sphere model:

$$\mathrm{t} = \frac{R_A + R_X}{\sqrt{2}(R_B + R_X)} \tag{1.1}$$

where R_A, R_B, and R_X are the ion radii corresponding to A, B, and X ions, respectively.

Generally, orthorhombic, tetragonal, and cubic polymorphs of ABX_3can form during crystallization as shown in Figure 1.3.

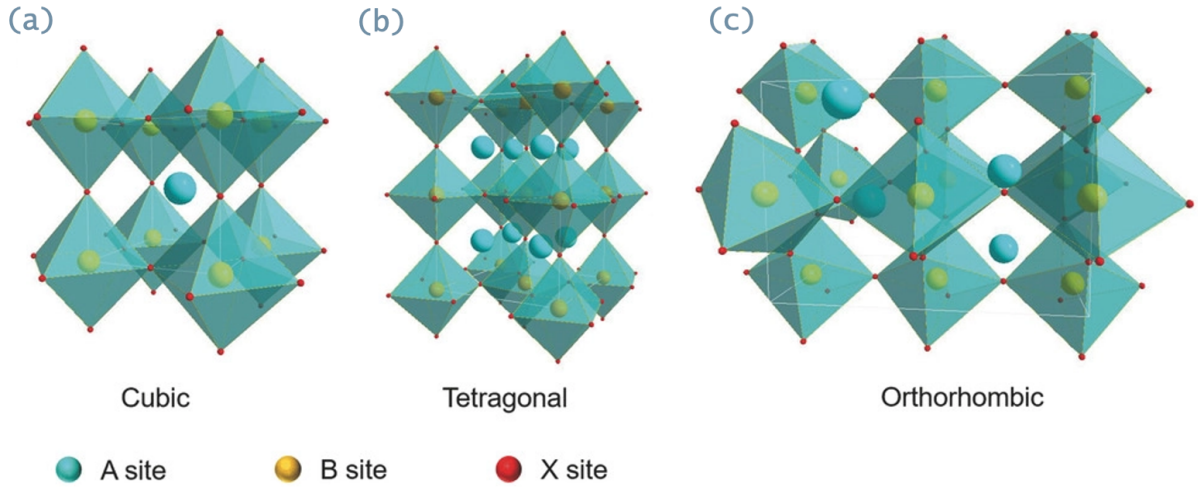

Figure 1.3: The crystal structures of perovskite materials with different symmetries: (a) cubic phase, (b) tetragonal phase, and (c) orthorhombic phase [11].

The tolerance factor has a significant impact on the stabilization of the material in a certain phase. When t is in the rage of $0.8 < t < 1$, ideal cubic perovskite structures or distorted perovskite structures with tilted octahedra are favored. Specifically, $0.9 < t < 1$ favors a cubic perovskite structure while for $0.8 < t < 0.$ 9, a distorted perovskite structure is formed. Values of $t < 0.8$ and $t > 1$ diminish the possibility of formation of perovskite structures. Therefore, it can be expected that t close to the middle of the range from 0.8 and 1, away from both the non-perovskite zones (Figure 1.5), would form a stable perovskite [12]. The smaller the A-site cation, the smaller the t because of the deformation of the octahedral frame due to the lack of support; thus, it cannot completely occupy the space of the BX_6 cubic octahedron. On the other hand, when the t value is

greater than 1, it indicates that the A-site cations are too large to have an octahedral framework and 2D layered structures, one dimensional (1D) chain structures, and even zero dimensional (0D) isolated clusters can be formed [13].

Therefore, measuring the radius of various ions is critical to determine the proper tolerance factor, which allows to estimate through simple geometric consideration whether a stable perovskite structure can be formed. In addition, t is not the only prediction criteria. Octahedral factor μ is another parameter for predicting stable crystal structure of perovskite materials. A μ value between 0.442 and 0.895 usually results in stable perovskite structures. The octahedral factor is given by the formula: $\mu = \frac{R_B}{R_X}$. The parameters of common perovskites are summarized in Figure 1.4.

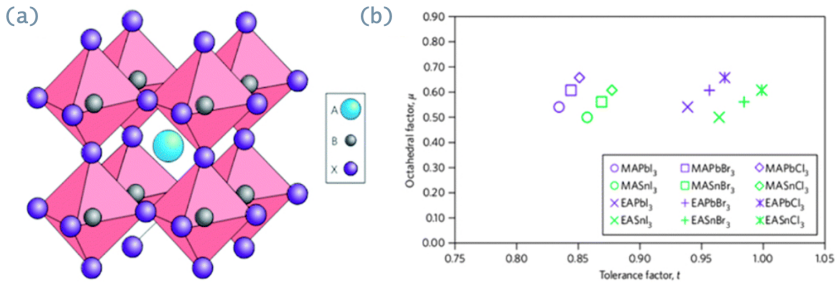

Figure 1.4: (a) Crystal structure of cubic perovskite ABX_3. (b) t and μ factors for 12 common organometal halide perovskites [14].

Figure 1.5 shows the calculated tolerance factors of $APbI_3$ systems where A = Na, K, NH_4, Rb, Cs, MA (methylammonium), FA (formamidinium), EA (ethylamine), and EDA (ethylenediamine).

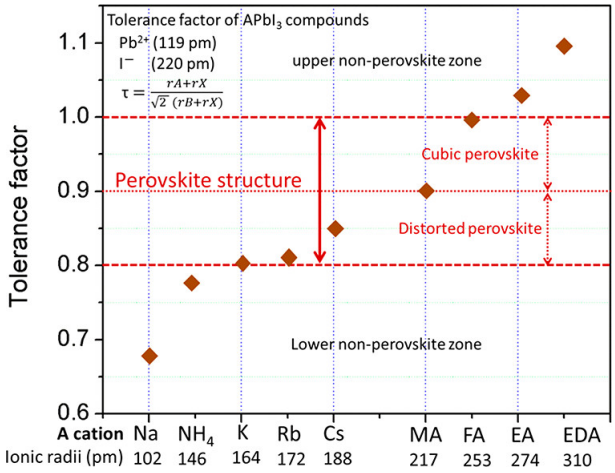

Figure 1.5: Calculated tolerance factors (t) for different cations (A) in APbI3 perovskite system [12].

1.2. Tridimensional Hybrid Halide Perovskites: Properties and Applications

Hybrid organic inorganic halide perovskites have attracted more and more researchers in the last decades because they are direct band gap semiconductors which combine the advantages of both organic (facile and cheap solution processability) and inorganic (high charge carriers mobility) materials, making them competitive with all the other semiconducting materials, especially in optoelectronic field. As shown in Figure 1.6, the physical, electrical, and photophysical properties of *hybrid halide perovskites*, such as their intrinsic ambipolar transport, high optical absorption coefficient, intense PL, changeable band gap, high quantum efficiency, long carrier diffusion and low non-radiative recombination rates make them excellent candidates for optoelectronic devices such as solar cells (SCs), light-emitting diodes (LEDs), light-emitting electrochemical cells (LECs), LASERs (Light Amplification by Stimulated Emission).

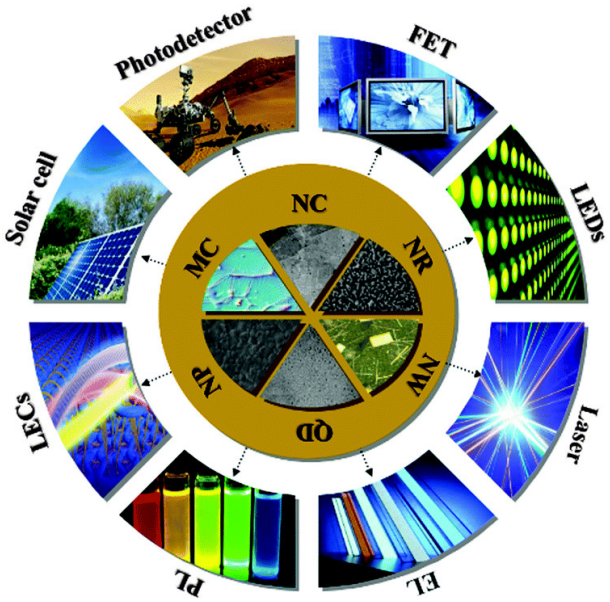

Figure 1.6: Schematic diagram showing the potential optoelectronic properties and applications of typical perovskite ABX_3(acronyms: QD: quantum dots, NW: nanowire, NR: nanorod, NC: nanocrystal, MC: millimeter-scale crystal, NP: nanoparticle, PL: photoluminescence, EL: electroluminescence, LEDs: light-emitting diodes, FET: field-effect transistor and LECs: light-emitting electrochemical cells) [14].

Perovskites have been used as light absorbers in dye-sensitized solar cells because of their tunable narrow band gap (DSSCs, Figure 1.7a). The perovskite absorbers showed superior advantages over traditional dyes by much more strongly absorbing over a broader range,

enabling complete light absorption in films as thin as 500 nm. Due to the material's ionic nature, which makes it simple to dissolve and degrade in an organic liquid electrolyte, the early perovskite solar cells were unstable. These issues were solved by using solid-state electrolytes as hole transport materials (HTL), which raised the devices' power conversion efficiencies (PCE). Perovskite was used to create a new type of solar cells (SCs), distinct from DSSCs, after it was shown to be a strong absorber as well as an effective charge transport material because of its crystallinity (Figure 1.7b,c). Additionally, the lattice's organic cations provide the additional benefits of solution processability and optical property tunability. Rarely does a material so inexpensive and widely accessible perform all three fundamental functions necessary for solar cell operation—light absorption, carrier production, and ambipolar transport. Thanks to molecular engineering of HTL [15] and better crystalline shape of perovskite layer [16], power conversion efficiencies (PCEs) have surpassed values of 25%.

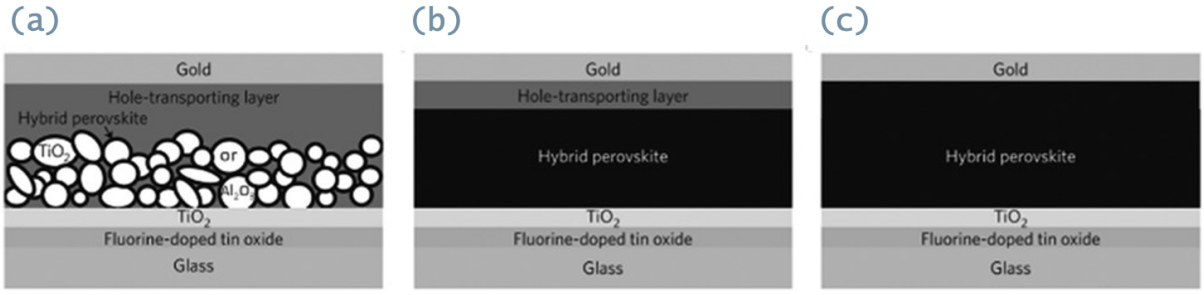

Figure 1.7: Architectures of typical perovskite solar cells. (a) Hybrid perovskite solar cell on n-type or inert mesoporous metal oxide; (b) planar hybrid perovskite solar cell; and (c) heterojunction perovskite solar cell.

Another possible use of perovskites in solar cells can be found in tandem solar cells, which are constituted by different stacked light-absorber layers, including almost one made from perovskite. Tandem solar cells can cover entire solar spectrum thanks to the change in composition of perovskite absorber layer (PCE 12.3%) or the use of other absorbers (efficiency around 22%), which keeps a semi-transparent perovskite layer on top [17, 18]. Despite these solar cells provide high Voc and PCE, fabrication remains an important issue, provided by different temperature and processing techniques for different layers and their electrical discontinuity at interfaces [17].
Despite all these advantages, diffusion of perovskite solar cells is limited by some important drawbacks concerning the toxicity of lead and its derivatives and the stability of devices. In fact, one of the main issues related to perovskite solar cells is the intrinsic instability of the perovskite material upon exposure to environmental moisture and oxygen,

high temperature and radiation. So, perovskite solar cells have shorter lifetime, ranging from few days to months and maximum up to a year, much lower than 25 years silicon solar cells lifetime [7, 19].
Thanks to their optoelectronic properties, metal halides perovskites have been studied also as easy-processing alternative for photodetectors. Picosecond-time exciton dissociation and good ambipolar charge transport, lead to investigation of these materials with good results on the main photodetection parameters. General photodetectors are essential for a range of commercial and scientific applications, including optical communications, environmental monitoring, day- and night- time surveillance, chemical and biological sensing. They achieve this by converting incident light into electrical signals.
Furthermore, organic inorganic halide perovskites display outstanding performance in lasing thanks to their high exciton binding energy and low defect density, they are an excellent material for implementing nanostructured lasers in a variety of applications, including nanophotonics, optical computing, and chemical/biological sensing. This is due to the wide tunability of emission color across the visible spectrum and the simple solution growth technique. Nowadays Perovskite lasers are under investigation by analyzing quantum structures made with 3D perovskites. Optically and electrically pumped lasers have been fabricated, but with limitations attributable to Auger recombination and low stability [19–21]. 3D perovskites have been studied also for X-ray detection, thanks to the presence of high atomic number elements, with two methods:

1. Direct conversion: this method converts x-ray photons directly into electrical charges. Single perovskite crystals give good results, despite some growth limitations on large areas [22].

2. Indirect conversion: with an intermediate step, x-ray photons are converted into visible light by a scintillator prior to conversion into electrical charges by a photodiode. Perovskite NCs have been investigated for this application [22].

New studies are also investigating the application of perovskite for resistive switching application, thanks to low voltage switching along with high on/off ration and fast switching speed. However, these studies are still at the beginning, even some improvements have been obtained using low dimensional perovskites [22].
Hybrid organic inorganic perovskites are appropriate for LEDs and LECs because they have excellent photoluminescence and emission optical characteristics. Halide perovskites can surmount the limitations of both traditional LEDs (suboptimal color quality) and emerging LEDs based on quantum dots (slow response time) and organic emitters (low maximum brightness) by producing bright, cost-effective, and high-color-purity LEDs. Moreover, solution processing technique (easier thanks to defect-tolerance of perovskites)

allows PeLEDs (perovskite light emitting diodes) to be competitive in future, thanks to lower costs of raw materials compared to OLED and III-IV semiconductors LED. Then, these materials allow to tune emission wavelength with chemical composition [20, 23]. Perovskite in LED can be used to obtain two different types of devices:

1. Optically pumped perovskite LED: perovskites act as phosphors for down-conversion from UV light;
2. Electrically pumped perovksite LED (EL-PeLED): perovskite act as an active layer between HTL and ETL for light emission.

In electrically pumped perovskite LED (shown in Figure 1.8), under forward bias, carriers are injected into the perovskite layer through HTL and ETL, respectively, and then the radiative recombination happens [24].

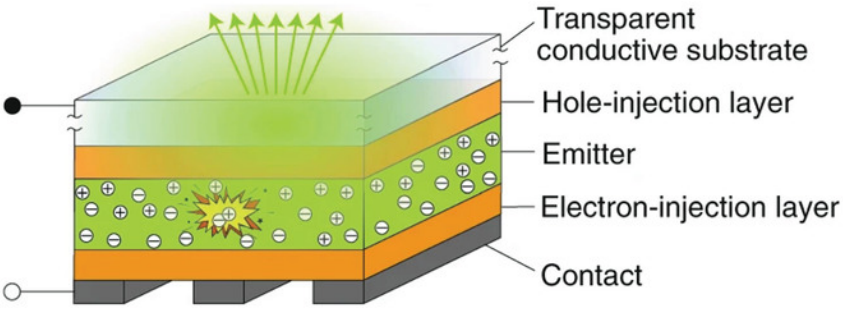

Figure 1.8: Schematic of an archetypical p-i-n PeLED. Note that the electron-injection and hole-injection layers can be interchanged to form an n-i-p architecture [20].

Optically pumped LEDs with perovskites have been studied as alternative (with a different architecture made from a InGaN chip as light source and a phosphor, shown in Figure **??**) for white PeLEDs. In these devices perovskite materials were studied as down-conversion phosphor for a UV light to obtain visible light [20].

However, there are still a number of problems and obstacles to address, such as thermal instability, particle aggregation, anion exchange, ligand dissociation, and photostability. In order to solve these issues, numerous surface treatments for perovskite have been developed, including compositional engineering, surface engineering, matrix encapsulation, and device encapsulation [25]. Low-dimensional perovskites have been investigated as an alternative to improve the stability of PeLED [25, 26].
Hybrid halide perovskites can be deposited on a wider variety of substrate materials, including plastics, thanks to the low-temperature solution technique than standard inorganic semiconductors, providing new prospects for versatile electrical and photonic

applications [7, 14]. Finally, they incorporate the advantages of organic and inorganic materials in terms of excitonic characteristics, which are fundamental because exciton transitions dominate the optical properties near and below the band gap. Excitons correspond to a bound state of one electron and one hole and can be created by light (SCs) or by relaxation processes of free electrons and holes, which can be induced electrically, for instance (LEDs). The two primary models used to classify these quasi-particles are the Wannier-Mott exciton with a large radius and low energy for inorganic semiconductors and the Frenkel model with a small radius and high energy for molecular crystals. The difference in excitonic radius (electron-hole distance) and, consequently, exciton binding energy between organic and inorganic materials is primarily caused by the screening potential difference. Hybrid structures, in which Frenkel and Wannier excitons are in resonance with each other and coupled through their dipole–dipole interaction at the interface, can combine both large radius of Wannier excitons, leading to good transport of charge carriers, and high oscillator strength of Frenkel excitons, as demonstrated by D. Basko et al. at a covalent-semiconductor/molecular-solid interface [27, 28].

1.3. Tridimensional halide perovskites limitations

Despite all characteristics and properties matching the requirements in optoelectronic field, there are still some obstacles to surmount. First of all, how to fabricate large areas and high quality devices, since usually their energy conversion efficiencies decline quickly with the increased active areas. In addition, the presence of lead in perovskite materials is one of the most significant limitations, and in order to surmount this issue, researchers are currently investigating alternative solutions based on tin and manganese, although their performance and stability are not yet comparable. The other main issue related to the use of perovskite materials in optoelectronic device is their stability, hence phase stability tuned with A-cations selection should be considered.

Stability issues can be classified in two main categories (According to Jena et al. classification [12]):

1. Structural intrinsic stability;
2. External/environmental stability.

Structural intrinsic stability issues concern perovskite structure and their use in optoelectronic devices:

- Ion migration: intrinsic ion migration persists to occur under the influence of electric field, either generated under sunlight or biased externally in dark. This phenomenon is correlated with anomalous J-V hysteresis, phase segregation, and is driven by presence of vacancies in perovskite lattice, with the mechanism described in Figure 1.9. This effect can be reduced thanks to perovskites with mixed organic-inorganic composition or alkali metals in interstitial position.

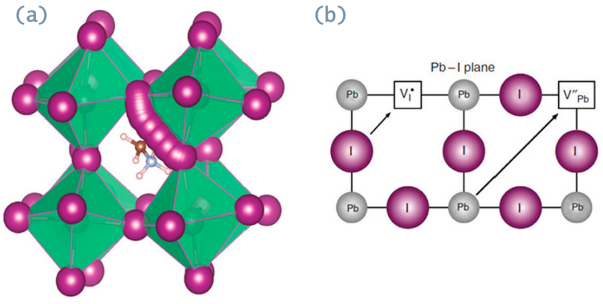

Figure 1.9: (a) Proposed migration path of I^- ions along the $I^- - I^-$ edge of the PbI_6^{4-} octahedron in the $MAPbI_3$ crystal. (b) Illustration of the migration paths for I^- and Pb^{2+} ions in the Pb−I plane [12].

- Interface degradation: In optoelectronic devices, the interfaces between perovskite and other layers play a crucial role in charge collection. At the interface, undercoordinated halogen atoms distort the tetragonal crystal structure and produce pinholes and irregularities. These irregularities may also function as recombination sites, thereby reducing charge transport [29]. Enhancing crystallinity can aid in increasing the stability. This can be achieved by passivating undercoordinated sites with additives. In addition, using confined structures for optoelectronic applications like QDs introduces the problems related to quantum structure stability [19].
- Thermal strain and strain induced degradation given by annealing or deposition (shown in Figure 1.10). These strains can cause ferro-elasticity, with phase transition under the applied stress. Strain-induced degradation should be also considered in perovskite design for enhancing overall stability of devices.

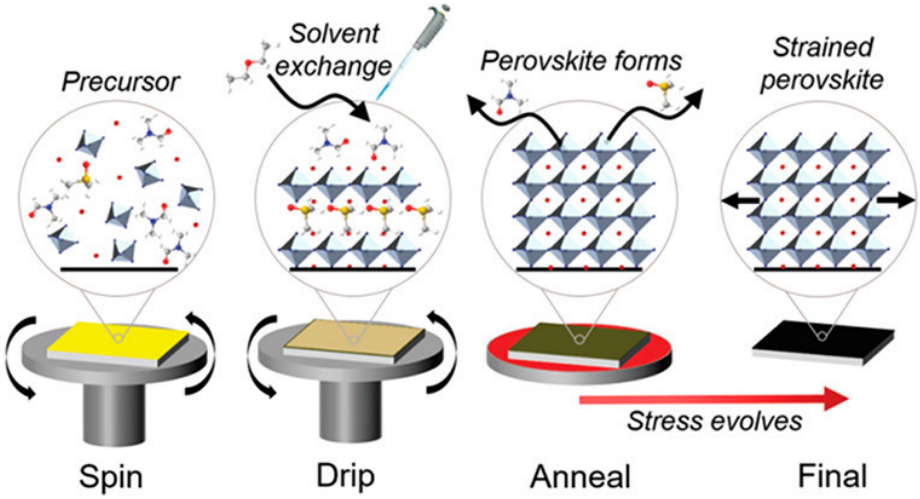

Figure 1.10: Schematic illustrating the stages of film formation and stress evolution in the film [12].

External/environmental stability is more related with interaction with external factor: light, moisture, heat and oxygen. Here are described the main phenomena affecting perovskites:

- Moisture induced decomposition: Water molecules can easily bind to perovskite by hydrogen bonding to form hydrated compounds, which alter local perovskite properties [12]. The losses can be reversed, but further entrance of water can cause irreversible degradation of perovskite to PbI_2 and other components, as described by the cycle depicted in Figure 1.11b. A key step is made from the formation of hydrated compounds more prone to degrade in (CH_3NH_2), HI, and PbI_2. This type

of degradation is reduced by encapsulation of device to avoid contact. Hydrophobic layers or passivation are new promising strategies.

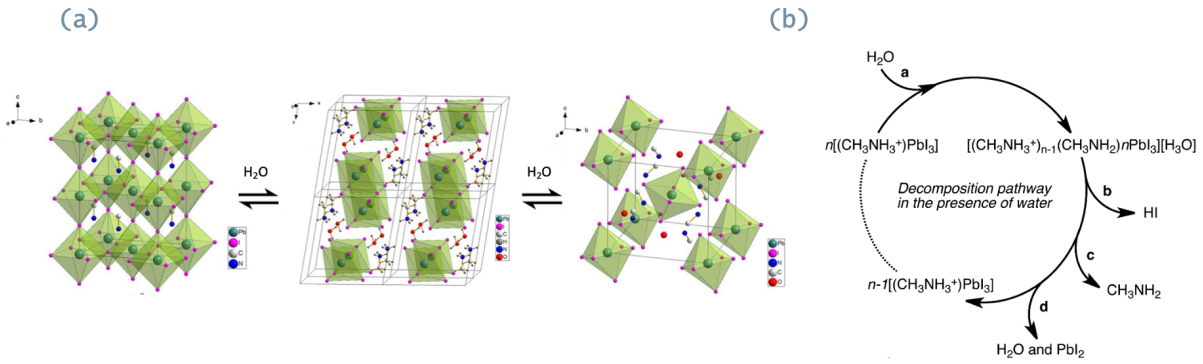

Figure 1.11: (a) The cubic, monohydrate and dihydrate phase of the MAPbI3 perovskite with the structural evolutions. [30] (b) Possible decomposition pathway of hybrid halide perovskites in the presence of water [31].

- Oxygen degradation: oxygen in contact with perovskite is absorbed on the surface passivating the trap state, thus creating an enhancement of luminescence. But, with the formation of superoxide ions in presence of light, perovskites undergo a degradation, through a process made by 4 steps, shown in Figure 1.12 leading to perovskite decomposition in PbI_2, H_2O, I_2 and CH_3NH_2 [32].

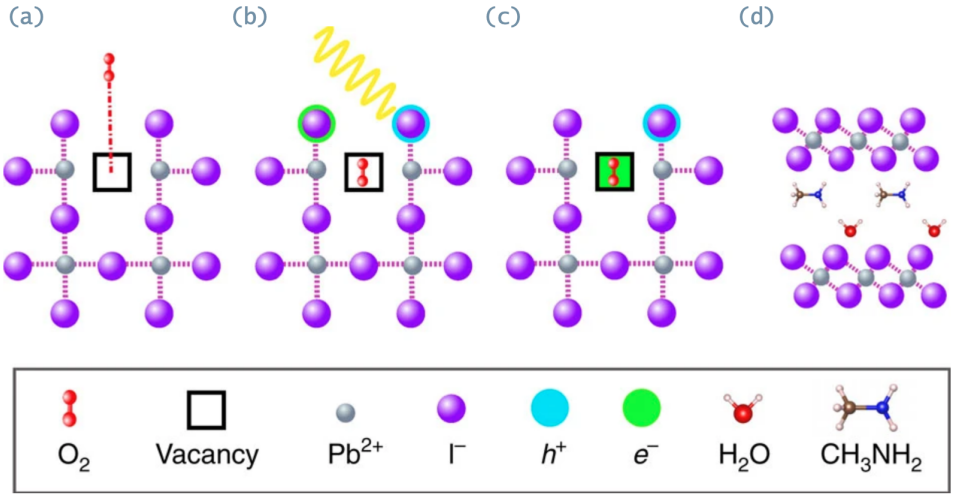

Figure 1.12: Schematic representation of the oxygen-induced decomposition (a) Oxygen diffusion and incorporation into the lattice, (b) photoexcitation of $CH_3NH_3PbI_3$ to create electrons and holes (c) superoxide formation from O_2, and (d) reaction and degradation to PbI_2, H_2O, I_2 and CH_3NH_2.

These products are decremental to charge transfer and can be avoided using less-acid cations, such as formamidinium (FA^+) or inorganic cations (Cs^+).

- Light induced degradation: light influences or intensifies all chemical, physical, and electronic processes. Regarding perovskite materials, photo-induced phase segregation generates a halide-rich region, resulting in a trap state with a low bandgap that influences the optoelectronic properties. Light accelerates perovskite's decomposition into PbI_2 and HI. The organic component can then be broken down into volatile compounds via reversible reaction. PbI_2 degrades in the presence of light due to the decomposition of molecular iodine and metallic lead [29]. Alternate solutions include the elimination of particle boundaries and the selection of cations that decrease volatility. Additionally, the reduction of halogen defects decreases the likelihood of these capture states occurring [12]. Regarding devices, the degradation between charge transport layers and perovskites, which plays a crucial role in charge collection, causes the majority of issues [29].
- Thermal degradation: Organic–inorganic hybrid and all-inorganic perovskites possess a good thermal stability, with degradation around 200°C for organic part and over 500°C for sublimation of PbX_6 octahedra [12]. However, the oxygen and moisture induced decomposition are accelerated and amplified at high temperature. And dehydration/hydration reaction enhances decomposition with temperature [12, 19].

Next chapters will focus primarily on the use of low-dimensional perovskites and the passivation of surfaces with functionalized molecules, specifically fluorinated molecules, among all techniques for improving perovskite stability.

1.4. Low-Dimensional Perovskites (LDPs)

By increasing the size of the A cation, thus increasing tolerance factor (eq. 3.1), the structure reduces its symmetry, arranging in lower dimensionalities. With respect to the 3D ones, the 2D, 1D and 0D perovskites are getting more and more attractive because of their higher stability and tunability. The dimensionality is given by the quantum confinement of the inorganic sublattice, since it is possible to model the alternated organic and inorganic layers of 2D perovskites with quantum wells, the inorganic chains of 1D perovskites as quantum wires and the isolated octahedrons of 0D ones as quantum dots.

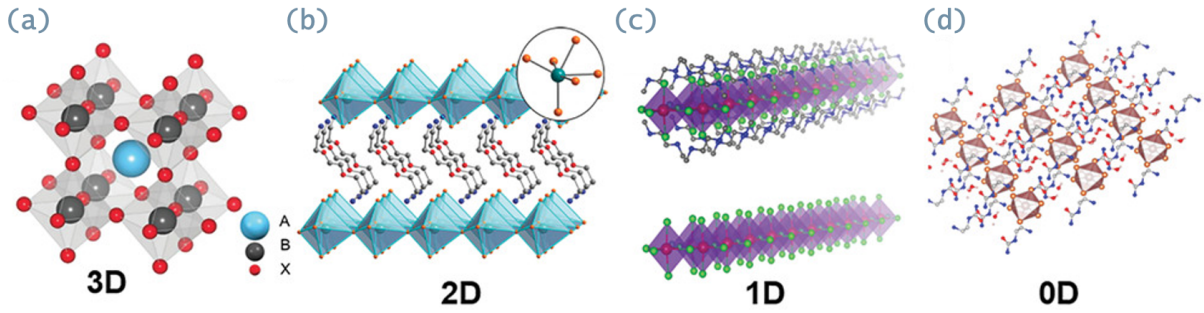

Figure 1.13: Typical low dimensional perovskites structures and their confinement effect. Respectively: (a) 3D cubic structure (b) 2D quantum wells, (c) 1D quantum wires, and (d) 0D molecules/clusters [33].

The important advantages of low dimensional hybrid organic–inorganic perovskites, which currently makes them a scrutinized material in view of their enormous potential for optoelectronic applications, can be summarized as:

- **Tunable bandgap** can be obtained by structure modification. The level of dimensionality and geometrical parameters of inorganic sublattice can be tuned by the selection of A organic cations. The wider selection of A cations allows to expand the energy gap tunability and to introduce further intermolecular interactions that can strengthen and stabilize the structure [34].
- **Different photophysical properties** given from effects such as STEs (Self Trapped exciton, photphysical phenomenon that will be explained later) and exciton binding energy modification given from quantum confinement [35].
- **Enhancement of perovskite stability**, made from higher formation energy of perovskite (lower formation energy with respect to precursors was reported as dangerous for perovksites stabilty). A higher stability with respect to 3D is also given by the lower volatility of the bigger organic cations and by the metal halide isolation,

which slow down the material degradation. With lower dimensionality perovskites incorporation of bulky cations dynamically stabilize metal halide structures and separate them from environment. In fact organic cation, thanks to their hydrophobic nature act as barrier against degradation induced by oxygen and moisture. In addition, organic moieties enhanced stability by interacting with other components in the crystal lattice at both ground states and excited states. Therefore, intrinsic chemical stability (bigger cations can be less volatile, reducing degradation), strong ionic and other supramolecular interactions, and high formation energy for the bulk crystal, stabilized excited states, are critical requirements to achieve high thermal and photo stabilities of organic metal halide hybrids [36, 37].

- **Easy processing** like 3D perovskites but with a wider selection of cations [35].

The higher crystallinity of 3D perovskites makes them the most effective charge-transport materials, despite the fact that lower dimensionalities offer numerous advantages, such as readily tunable photo response, faster response time, and improved stability. One of the highest reported PCE values in 2D perovskite SCs is approximately 18%, which is still significantly lower than that of 3D perovskite SCs (25%). As a result, rather than being used directly as solar cell absorbers, low-dimensional perovskites can be integrated into 3D perovskite-based devices to improve the surface properties of 3D perovskite grains and coatings. For instance, the fabrication of solar cells with a 2D/3D hybrid perovskite active layer is frequently favored due to its greater stability and high efficiency. Incorporating 2D layers into the lattice neutralizes the undercoordinated species and strengthens the interactions. Consequently, they will be located where undercoordinated species congregate: at the surface, forming an interlayer between 3D perovskite and HTL and facilitating charge transport across the device, as shown in Figure 1.14, and at the grain boundaries, preventing the accumulation of defects that can act as trap sites for charges moving across the perovskite grains (Figure 1.15).

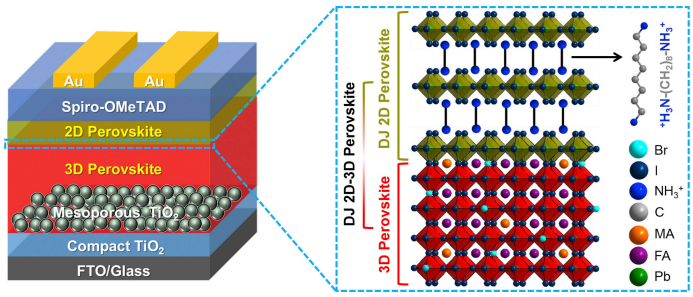

Figure 1.14: Schematic illustration of 2D-3D perovskite and SC architecture [38].

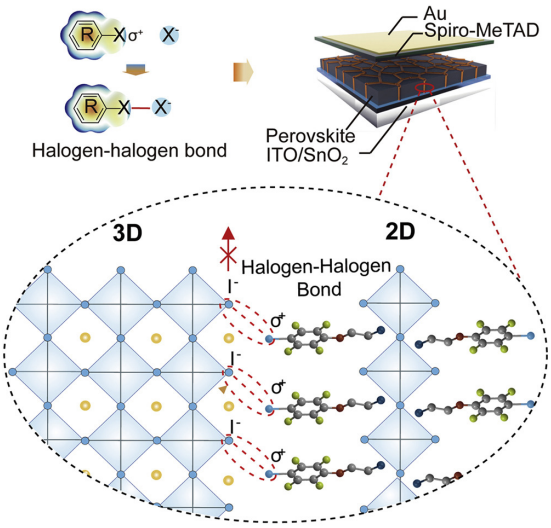

Figure 1.15: Schematic illustration of 2D-3D perovskite interactions and SC architecture [39].

Due to the size effect and significant differences in dielectric constants between the organic and inorganic parts, excitons in low dimensional perovskites are spatially confined. This suppresses the separation of excitons and greatly improves the radiation recombination efficiency. Therefore, organic–inorganic low dimensional perovskites are considered to be good candidate materials for stable LEDs with high photoluminescence quantum yield (PLQE). Some 0D hybrid perovskite nanocrystals have been reported as efficient broadband phosphors (Figure 1.16a), showing great light-emitting performance up to 85% of PLQE and excellent thermal stability, and making the materials attractive candidates also for white light-emitting diodes (WLEDs) manufacturing. 2D hybrid perovskites have also showed broadband white-light-emitting (Figure 1.16b,c; N−MEDA = N1−methylethane−1,2−diammonium; EDBE = 2,2−(ethylenedioxy)), with emission almost covering the entire visible spectrum and PLQE up to 18%, due to the formation of self−trapped excitons in the deformable lattice [33].
Exciton self−trapping occurs in a wide variety of materials in presence of a deformable lattice. They form when excitons couple with the soft lattice, inducing elastic structural distortions that lower the system's energy (Figure 1.17), similarly to small polarons. Unlike free exciton states (FE) PL, STE luminescence is typically broad and significantly Stokes shifted from the FE absorption. The distortion of the self−trapped state with respect to the ground state (given by the HuangRhys parameter, S) broadens the emission. Both S and the stabilization of the self−trapped state with respect to the untrapped state (self−trapping depth) contributes to the Stokes shift [40].

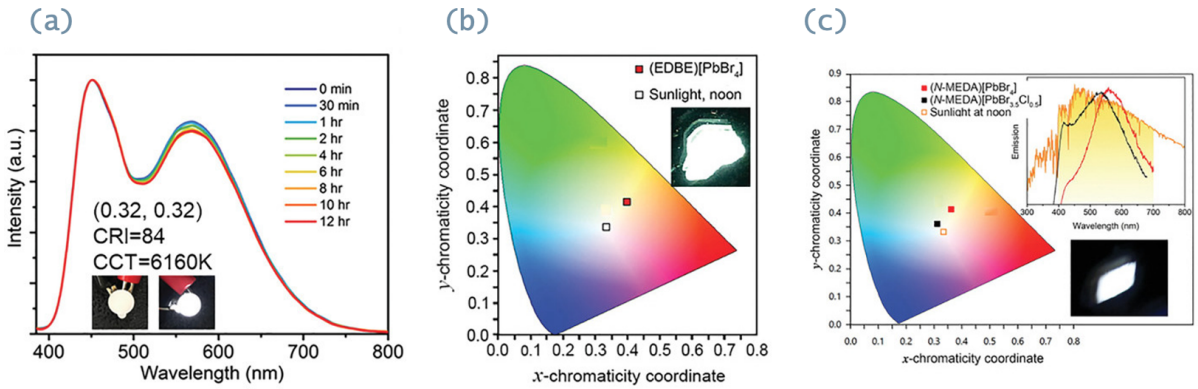

Figure 1.16: (a) Emission stability and luminous performance of 0D $(C_4N_2H_14Br)_4SnBr_3I_3$ LED. (b) CIE coordinates of (EDBE)($PbBr_4$) and sunlight at noon. Inset is a photograph of (EDBE)($PbBr_4$) under 365 nm irradiation. (c) CIE coordinates and emission spectrum of white-light emitters and sunlight at noon. Inset is a photograph of (N-MEDA)($PbBr_4$) under 380 nm irradiation.

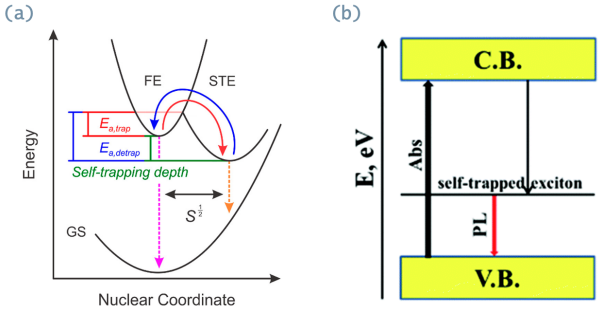

Figure 1.17: Two examples of energy diagram representing self-trapped exciton [40, 41]

.

Finally, it has been shown that low-dimensional perovskites have higher PCEs, quicker decay, and larger Stokes shifts than 3D ones. In the disciplines of medical imaging, non-destructive detection, and space exploration, these benefits demonstrate their potential for large-area, low-cost scintillator devices. Due to the high exciton binding energy, some 2D perovskites exhibited less thermal quenching than their 3D counterparts, allowing a moderate light yield to be obtained at ambient temperature. 2D perovskite-based scintillators have been utilized for alpha particle detection, X-ray imaging, and alpha particle and gamma ray separation. In addition, low dimensional perovskites have shown promise in the transducer field due to their tunable structural phase transition and fluorescence emissions, with 0D hybrid perovskites being used as acetone gas sensors [33].

1.5. LDPs based on fluorinated cations

Fluorination of organic cations is an intriguing strategy for tuning the self-assembly and optoelectronic properties of low-dimensional perovskites. The presence of highly fluorinated saturated molecular fragments in the resulting low dimensional perovskite can impart an additional water-repellent character and superior stability with respect to fully hydrocarbon-based cations used so far. With the systematic modulation of the size and molecular structure of fluorous cations, the optoelectronic properties of 2D HPs are altered [42]. As described before, low dimensional hybrid perovskites are versatile materials, whose electronic and optical properties can be tuned through the nature of the organic cations. A model adopting bulky fluorous cation (Fluo = $(CF_3)_3CO(CH_2)_3NH_3^+$) that intercalates in between single inorganic layers adopting a pure 2D $(Fluo)_2PbI_4$ structure shows that electrostatic effects associated with fluorination, combined with the steric hindrance due to the bulky side groups, drive the formation of spatially dislocated charge pairs with reduced recombination rates [43].
In the work done by Inés García-Benito et al. [42] they synthesized a new series of fluorous organic cations and shaped them to form tunable and stable 2D HPs (Figure 1.18).

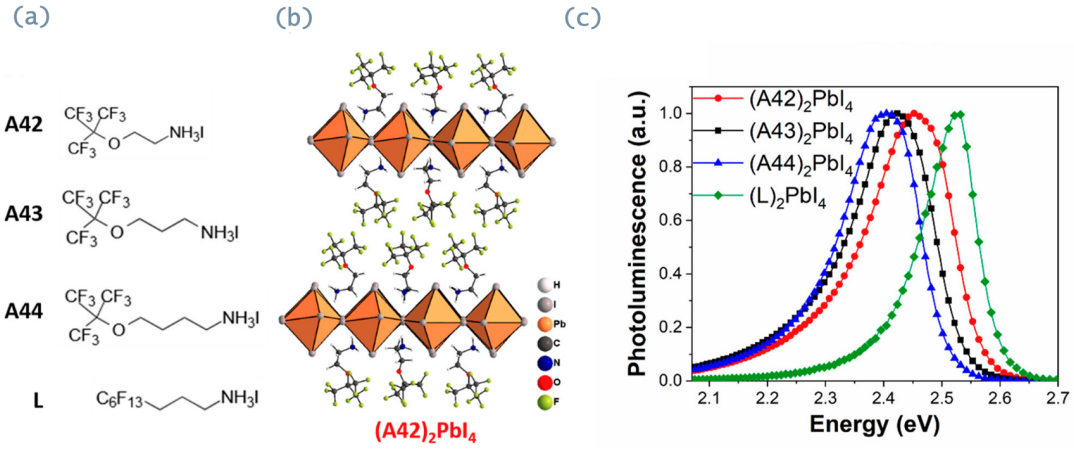

Figure 1.18: (a) Molecular structure and abbreviated name of the studied fluorous cations. (b) Schematic structure of 2D HP with A42 as the organic spacer between the inorganic PbI_6 layer. (c) Normalized PL spectra ($\lambda_{excitation}$ = 367 nm) of $(A42)_2PbI_4$, $(A43)_2PbI_4$, $(A44)_2PbI_4$, and $(L)_2PbI_4$ in thin films at room temperature [42].

The fluorous cations impart extreme stability of the 2D HPs upon exposure to atmosphere conditions and enhance the water-repellent character of the 2D HP surface. It was demonstrated that the size and shape of the organic cation modulate the 2D HP structure, electronic, and optical properties. Despite the fact that the organic spacers do not

participate in the electronic structure, they influence the perovskites electronic structure via an indirect structural effect on the inorganic sheet, inducing a variation of the band gap and exciton binding energy. These local distortions affect the binding energy more than local dielectric mismatch. The longer the cation, the smaller the band gap. This results in a lower exciton binding energy and smaller effective masses, pointing toward a better transport for the elongated fluorous chains. This new family of stable 2D HPs not only shows the large extent of tuning the optoelectronic properties by simple shaping of the fluorous organic spacer, but, importantly, it shows a remarkably high structural stability kept intact even upon a one-month air exposure. Overall, these attributes make this fluorous 2D HP an exciting candidate for stable perovskite optoelectronics [42].
Fluorination was also exploited to change the electron distribution in aromatic compounds, thanks to their strong electronegativity. As computed from DFT calculation by Wang et al.[44], degree of fluorination and position of fluorine in aromatic cations create different electron distribution in phenylethylamine (PEA), as shown in Figure 1.19. This results in different packing of these cations in 2D perovskite layers. Better results in terms of PCE and stability for solar cells were obtained with fluorination, thanks to strong dipole moment that reduce charge recombination. Moreover, moisture is enhanced by hydrophobicity induced by fluorine atoms.

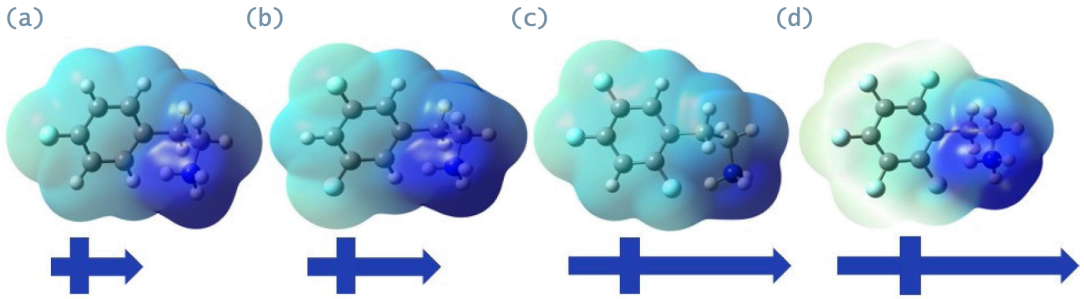

Figure 1.19: DFT calculation results of the ammonium salt, with electrostatic surface potential of PEAI (a), F_2PEAI (b), F_3PEAI (c), and F_5PEAI (d) (blue arrow length is the molecular dipole moment).

Effect on fluorine substituents on aromatic ring were investigated for ortho-, meta-, para- and per-fluorinated benzylammonium 2D perovskites. They exhibit different structural symmetries and packing, due to the larger steric hindrance between adjacent cations, together with enhanced phase transition temperature and changed polarization. Due to the changes in intermolecular forces and dipole moments, ortho-substitution and per-fluorination exhibited a high piezoelectric response and exceptional ferroelectricity [45, 46]. Zhang et al. [47] compared in 2D perovskite 4-fluorophenethylammonium (F-PEA)

instead of phenethyl ammonium (PEA). Fluorination results in a different electron density distribution over aromatic cation. This effect results in a different intermolecular packing of aromatic cations, with slip-stacked rings induced by fluorination effect on π interactions (Figure 1.20a). While phenethyl ammonium cations are organized in edge-to-face order (Figure 1.20b). As a result, conductivity between lead iodide planes was enhanced, also given by perovskite sheets alignment.

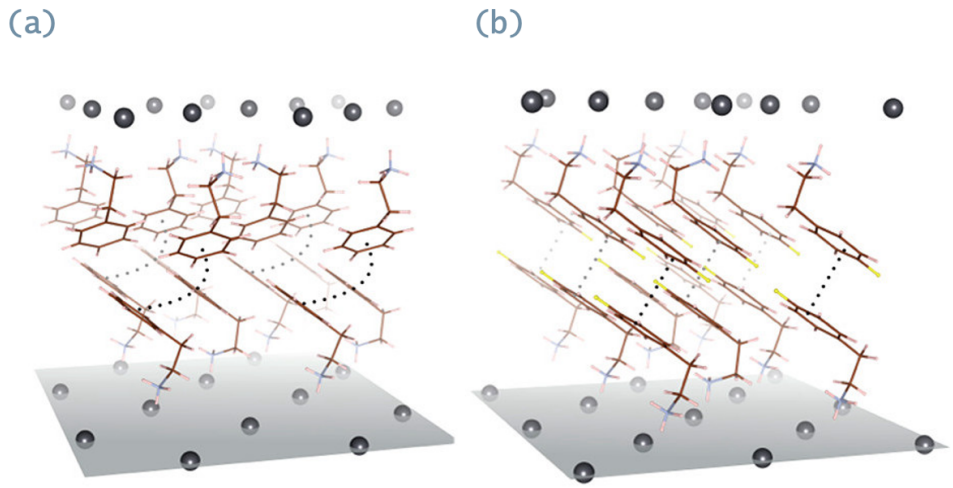

Figure 1.20: Structures of (a) $(PEA)_2PbI_{4-}$ and (b) $(F\text{-}PEA)_2PbI_{4-}$ single-crystal [47].

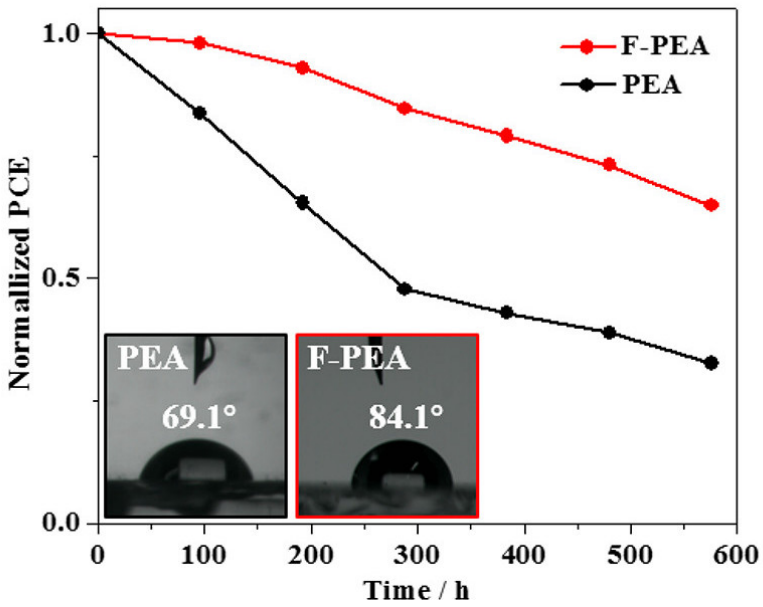

Figure 1.21: Thermal stability comparison of PEA- and F-PEA-based PSCs tested at 70 °C in ambient environment, dark storage, without any encapsulation. Inset shows the contact angles between corresponding perovskite films and water [47].

Moreover, fluorinated aromatic rings with halogen atoms were used to exploit halogen bond in perovskite, thanks to the strongly electronegative fluorine atoms. They attract the delocalized electronic cloud of the aromatic ring and induce the formation of a region of positive potential along the same direction of the halogen bond, rendering the interaction highly directional [48, 49]. Another study made by Binbin Luo et al. [50] highlights the critical role of interlayer supramolecular interaction such as hydrogen bonding in determining the optoelectronic properties: Saturated cations with fluorination have been reported to create an hydrogen bond network that reduce lead halide distortion. Because of the formation of inter- and intramolecular hydrogen bonding, the magnitude of octahedral distortion and interlayer distance are varied dramatically. This effect result in a lower bandgap. In particular, a series of unsubstituted ethylammonium (EA) and F-substituted EA including 2-fluoroethylammonium (FEA), 2,2-difluoroethylammonium (2FEA), and 2,2,2-trifluoroethylammonium (3FEA) are successfully incorporated into 2D LHPs, which are denoted as 0FP, 1FP, 2FP, and 3FP, respectively. Because of the formation of inter- and intramolecular hydrogen bonding, the magnitude of octahedral distortion and interlayer distance are varied dramatically. 1FP shows the lowest bandgap and best photoconductivity among the four prepared 2D LHPs because of the smallest interlayered distance. An intense broadband emission with 12.3% photoluminescence (PL) quantum yield (QY) is observed in 2FP, attributed to the great out-of-plane distortion of inorganic layers [50].

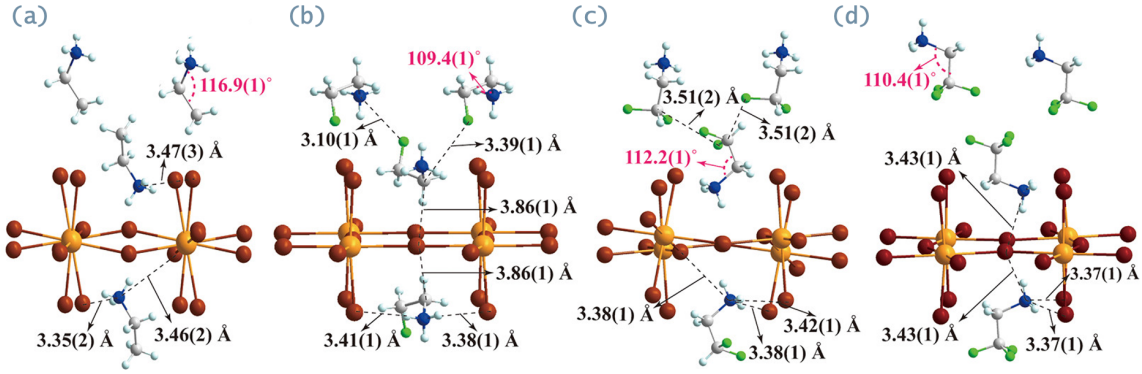

Figure 1.22: Hydrogen bond (dashed lines) interaction between adjacent organic cations and at the organic–inorganic interface for (a) 0FP, (b) 1FP, (c) 2FP, and (d) 3FP samples [50].

Owing to the hydrophobic nature of the F–C bond and intermolecular hydrogen bonding, all three F-substituted 2D LHPs exhibit moisture stability that is better than that of 0FP. This is an intriguing strategy for tuning the optoelectronic properties of low-dimensional perovskites.

1.6. Imidazolium in perovskites

As previously mentioned, the stability of perovskite materials under different degradation stresses is still the bottle-neck for the application of perovskites in solar cells. To overcome these challenges, several strategies have been proposed, which include low-dimensional perovskites, surface treatment, and additives in precursors. Additive-assisted perovskite processing has been reported with respect to modulating the crystallization dynamics, which leads to the achievement of larger perovskite grain sizes and higher film qualities with less defects. Typically, these additives in the perovskite precursors compete in interactions with other precursor components, which slows the crystallization rate. These additives also passivate the dangling bonds on the surface of the perovskite film and suppress the formation of surface defects. Ionic liquids have emerged as a promising kind of additives due to their unique properties, such as low volatility, high ionic conductivity, and electrochemical stability, to improve the device performance. Among others, imidazolium derivatives have been used to bind undercoordinated halide anions in the precursors. The imidazolium unit can also be introduced with different alkyl or fluorocarbon chains, which have been revealed to produce important hydrophobic effect in the film [51]. 1-alkyl-methyl-imdiazolium iodides are a well-known family of ionic liquids [52]. Increasing the length of alkyl chain it is possible to tune thermal and functional properties of such materials. In fact, with alkyl chains longer than 11 carbon atoms it is possible to obtain a liquid crystalline behavior. 1-dodecyl-3-methyl-imidazolium ($C_{12}ImMetI^-$) iodide exhibits a liquid crystalline behavior with a smectic A phase (melting point 80°C) which is a consequence of the dodecyl chains interdigitation. These materials thanks to their good conductivity and good thermal stability have been reported for electrolyte in DSSC, thanks to alignment of alkyl chain that creates a path for iodine ions [53, 54].
Another interesting alternative is given from perfluoroalkyl-methyl-imidazolium salts. Inside this category, 1-Methyl-3-tridecafluoroctyl-imidazolium iodide Figure 1.23a and 1-Methyl-3 tridecafluorononyl-imidazolium iodide (Figure 1.23b) undergo to a phase transition to smectic phase respectively at 94°C and 86°C [55, 56]. These transitions were attributed to an increase in order for these structures induced by fluororous-fluorous interaction of perfluoroalkyl chains. Therefore, these materials offer a thermotropic liquid crystalline behavior mediated by interdigitation of fluorocarbon chains [56]. This effect with an ordered liquid crystal phase improves the charge transfer dynamics at the TiO_2^- dye/electrolyte interface and the transport in the electrolyte solution. These results make perfluoroalkyl functionalized imidazolium interesting cations for the design of new low dimensional perovskites [55, 56]. Moreover, HOMO and LUMO are affected from perfluoroalkyl chains effect [47, 57].

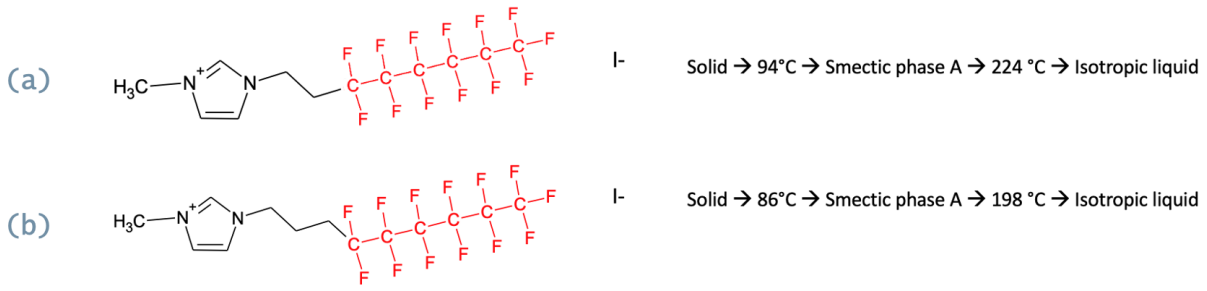

Figure 1.23: 1-Methyl-3-tridecafluoroctylimidazolium iodide (C8F13ImMetI-) and 1-Methyl-3-tridecafluorononylimidazolium iodide (C9F13ImMetI-) and their phase transitions [55, 56].

1.6.1. Surface and defects passivation with imidazolium salts

Imidazolium iodide has been investigated as a passivating agent for 3D perovskites due to the possibility of passivation provided by N atoms acting as Lewis's base to passivate uncoordinated Pb on the perovskite surface. As a result of their positive charge, substituted imidazolium salts were utilized to passivate defects with a negative charge. In the case of imidazolium, the formation of H bonds with halogen atoms has also been linked to improved charge transport and particle size. This effect also diminishes the migration of iodine ions, a significant issue in perovskite solar cells. With the addition of a controlled amount of imidazole to methyl-ammonium lead halide perovskite, the material's stability was improved by Tomulescu et al. [58] with $MA_{0.94}IM_{0.06}PbI_{2.6}Cl_{0.4}$ perovskite. Moreover Salado et al. [59] demonstrated higher time for relaxation of photoluminescent adding 5% of imidazolium, with improved and more stable PCE (from 18.6% to 20%), thanks to effect on vacancies and grain boundaries [59].

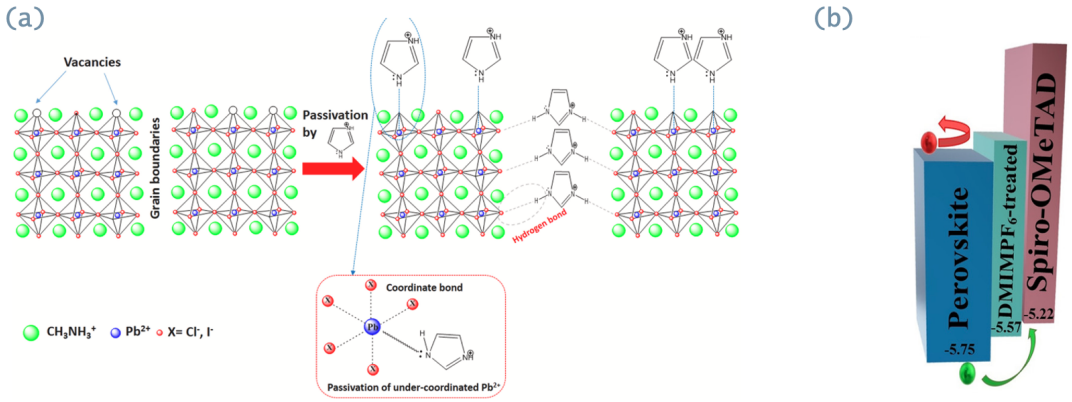

Figure 1.24: (a) Mechanism for passivation of $MA_{1-x}IM_xPbI_{2.6}Cl_{0.4}$ defects by IM doping (b) Energy band diagram of the perovskite device passivated with $DMIMPF_6$ [58, 60].

Hence, imidazolium salts has been used as passivator of 3D lead iodide perovskite, thanks to their nature of ionic liquid that can passivate (with their counterions) perovskite surface defects. This passivation keeps good conduction between layers, with good matching of energy levels, as shown in Figure 1.24a [60]. Alkylated imidazolium salt, such as butyl-methyl imidazolium tetrafluoroborate, propyl-methyl imidazolium bromide or dimethyl imidazolium hexafluorophosphate ($DMIMPF_6$), were used to passivate 3D perovskite surface to enhance stability and efficiency of solar cells. On one hand passivation of surface defects reduces trap-assisted recombination. This effect combined with good conduction of imidazolium salts increases charge transport with charge transport layers. This result in an increase of power conversion efficiency for controlled amount of these salts [61]. On the other hand, these ionic liquids possess hydrophobic alkyl chains that protect from moisture degradation, as confirmed by stability of power conversion efficiency over longer time with these passivating salts, even at higher temperatures [62]. In addition, these salts give higher values with respect to pristine perovskites of photoluminescence and photoluminescence time of relaxation. This phenomenon indicates suppression of charge recombination [63]. Another solution for passivation was investigated with imidazolium cations with fluorinated chains. In the work of Xindong et al. [51] methyl-imidazolium with perfluoroalkyl substituent in position 3 was studied as salt with tetrafluoroborate (Figure 1.25). Different length for fluorinated part were investigated, obtaining a hydrophobic effect over perovskite surface. Then, for 1-methyl-3-(3,3,4,4,4 pentafluoro-butyl) imidazolium tetrafluoroborate (MFIM-2), better results in terms of crystal growth, lower PbI_2 impurities and performances of solar cells were obtained. The results reveal that MFIM-2 suppressed the formation of PbI_2 crystals during crystallization, enlarged the grain size, and reduced the defect density, which led to an increased photovoltage of 1.12 V and efficiency of 19.4%.The main effects of these cations are made from passivation of undercoordinated sites and hydrophobic stable phase that enhance device lifetime. As previous passivation cases, PL was enhanced in terms of PLQY and relaxation time [51].

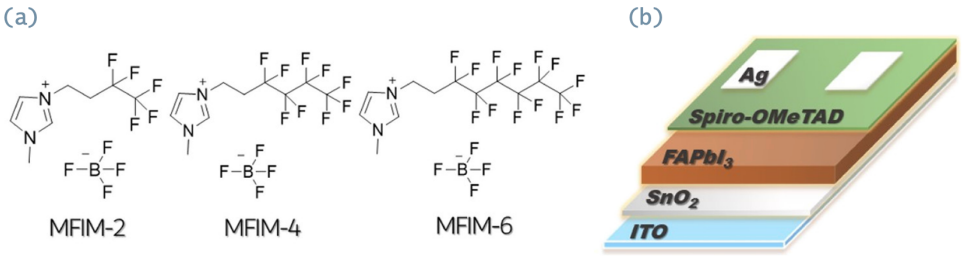

Figure 1.25: (a) Molecular structure of ionic liquids MFIM-2 (b) Schematic architecture of the device, elaborated from Xiangdong Li et al. [51].

1.6.2. Imidazolium in low dimensional perovskites

Imidazolium (and its related salts) has been studied also as organic cation in low dimensional perovskite [64]. Imidazolium perovskites usually exhibited 1D structure, with face sharing lead halide octahedra surrounded by imidazolium cations. Some exceptions are given from imidazolium and ammino-propyl-imidazolium le ad bromides that create 2D perovskites, because of strong templating effect of double ammonium group with lead bromide sublattice. In addition, butyl-methyl-imidazolium lead bromide has a cluster 0D structure templated by hydrogen bonds among butyl chains [51]. As reported by Seth et al. [65], Imidazole reaction with PbI_2 creates a 1D perovskite ($C_3N_2H_5$) PbI_3 by obtaining yellow crystals. This compound is characterized by 1D lead iodides chains surrounded from imidazolium cations, as shown in Figure 1.26. These cations create H-bonding between H of their C1 and iodine of inorganic chains [65].

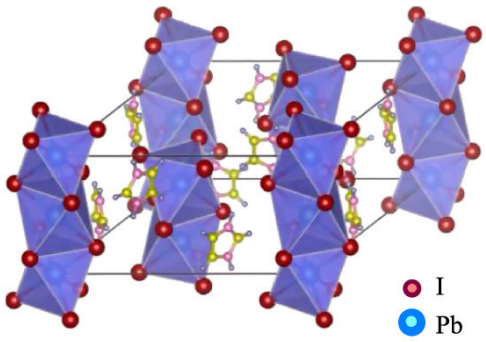

Figure 1.26: Imidazolium perovskite crystalline structure from Seth et al. [65]

Despite differences between imidazolium lead halides (lead bromide was reported as 2D perovskite), 1-alkyl-3-methyl-imidazolium perovskites has been reported as 1D structures with different halogen atoms (Cl and Br).The most significant example is given from ethyl-methyl-imidazolium (C_2ImMet) lead halides, with reported resolved single crystal structures for lead chloride, bromide and iodide [66, 67]. C_2ImMet cations separates lead halide chains, creating hydrogen bond with them and among organic cations. In ethyl-methyl-imidazolium $PbCl_3$ and $PbBr_3$ hydrogen bonds between H atoms are related to C atoms. These bonds template distorted lead chloride structure as shown in Figure 1.27. These results allow to make comparison among different 1D lead halide's structure, considering halogen effect in terms of dimensionality and electronegativity [66, 67].

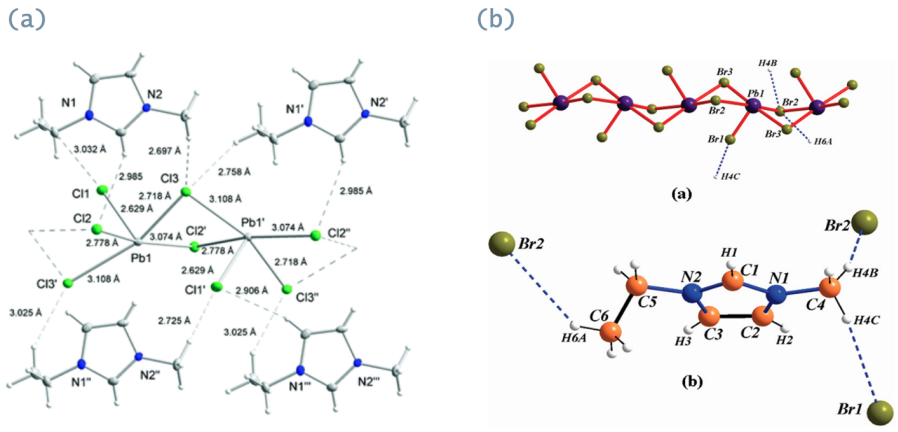

Figure 1.27: 1-ehtyl-3-methyl-imidazolium (a) lead chloride and (b) lead bromide [66, 67].

Lead was found in a pentacoordinate state with different length given by distortion, creating an orthorhombic unit cell with space group Pnma, for lead bromide. While P_{212121} space group was found for lead chloride. This difference is made by different strength and template of hydrogen bonds between inorganic sublattice and C_2ImMet cations. Hydrogen bond templating effect was found effective also with longer chains as described from single crystal structure of lead bromide 1D perovskites with methyl substituted imidazolium salts with propyl, pentyl, and hexyl as substituent in position 3. These interactions are mediated by hydrogen bonding that can interest H related to primary carbon of alkyl substituent in position 3. These atoms are more prone to hydrogen bonding with halogen of inorganic chains thanks to electron delocalization induced by the nearest N atoms. Increasing alkyl chain length, hydrogen bond of CH_3 group in alkyl chain becomes less important, with interdigitation among alkyl chain more dominant. However, butyl-methyl imidazolium lead bromide exhibits a 0D clustered structure thanks to hydrogen bonds among imidazolium cations. [66] So, even with alkyl-methyl imidazolium perovskites some unexpected changes in dimensionality can occur, 1D structures were reported. This effect results in different optoelectronic properties [68–70].
Temperature affects crystalline structure with phase transitions that occur at low temperature because of arrangement of alkyl chains of imidazolium. These phase transitions affect dielectric permittivity at different frequencies evaluated at different temperatures. In fact, over a certain temperature, dielectric relaxation shifts dielectric peak to higher frequencies. This dielectric relaxation can be ascribed to phase transition over the previously mentioned temperature. Under this temperature dipole motion is suppressed leading to a dielectric permittivity with temperature [68–70]. Distortion parameters of lead halides chains are affected by different packing and interaction of imidazolium cations. These parameters will affect photoluminescence with similar STEs broadband wavelength.

1.7. Perfecta and its derivatives

Since multibranched fluorinated Perfecta derivatives will be used in the experimental work, a general introduction to this molecule and its application has been provided. Perfecta (1,3-Bis[2,2,2-trifluoro-1,1-bis(trifluoromethyl)ethoxy]-2,2-bis[[2,2,2-trifluoro-1,1-bis(trifluoromethyl)ethoxy]methyl] propane) is a novel superfluorinated molecular probe for 19F-magnetic resonance imaging.

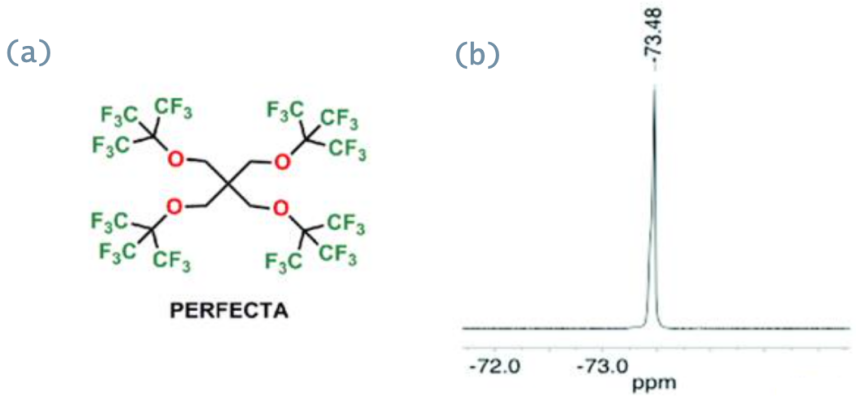

Figure 1.28: a) Chemical structure of Perfecta, a 36 equivalent fluorine atoms containing 19F-MRI-active probe, and b) the 19F-NMR spectra of its oil in water formulation [71].

The interest in using short polyfluorinated chains with a high number of equivalent fluorine atoms has attracted the attention of lot of scientists. In recent years much attention has been focused on the use of tri-perfluoro-tert-butoxyl-functionalized pentaerythritol (27F) derivatives, Figure 1.29 displays the chemical structure of 27F.

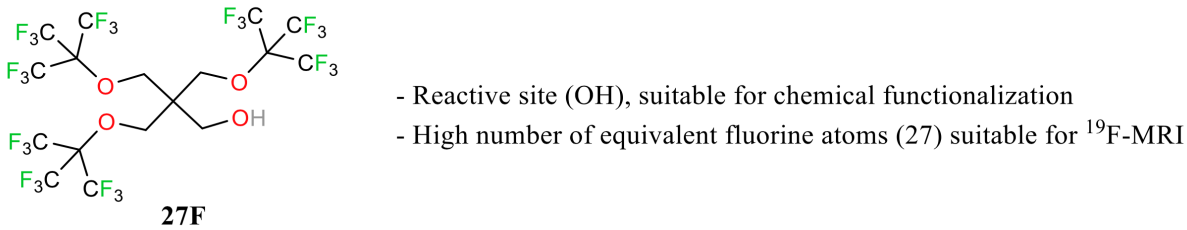

Figure 1.29: Chemical structure of tri-perfluoro-tert-butoxyl-functionalized pentaerythritol (27F). The presence of a free hydroxyl group makes the molecule suitable for the construction of new 19F-MRI-active probe.

The presence of 27 equivalent fluorine atoms coming from -CF_3 chemical groups generates

a single peak at 19F-NMR, a promising characteristic for the construction of good 19F-MRI probes. Furthermore, 27F shows a free hydroxyl group which is suitable for chemical functionalizations. From the first 27F derivatives reported by Bruce Yu and coworkers in 2007 [72], the library of derivates has increased and applications have been various, as shown in Figure 1.30. In 2011 S. Caramori and collaborators have developed a zinc phthalocyanine complex functionalized with three hydroxyl-terminating 27F derivatives; this yielded the possibility to tune electronic distribution and anti-aggregating properties of the photosensitizing dye suitable to application in dye-sensitized solar cells (DSCs) [73].

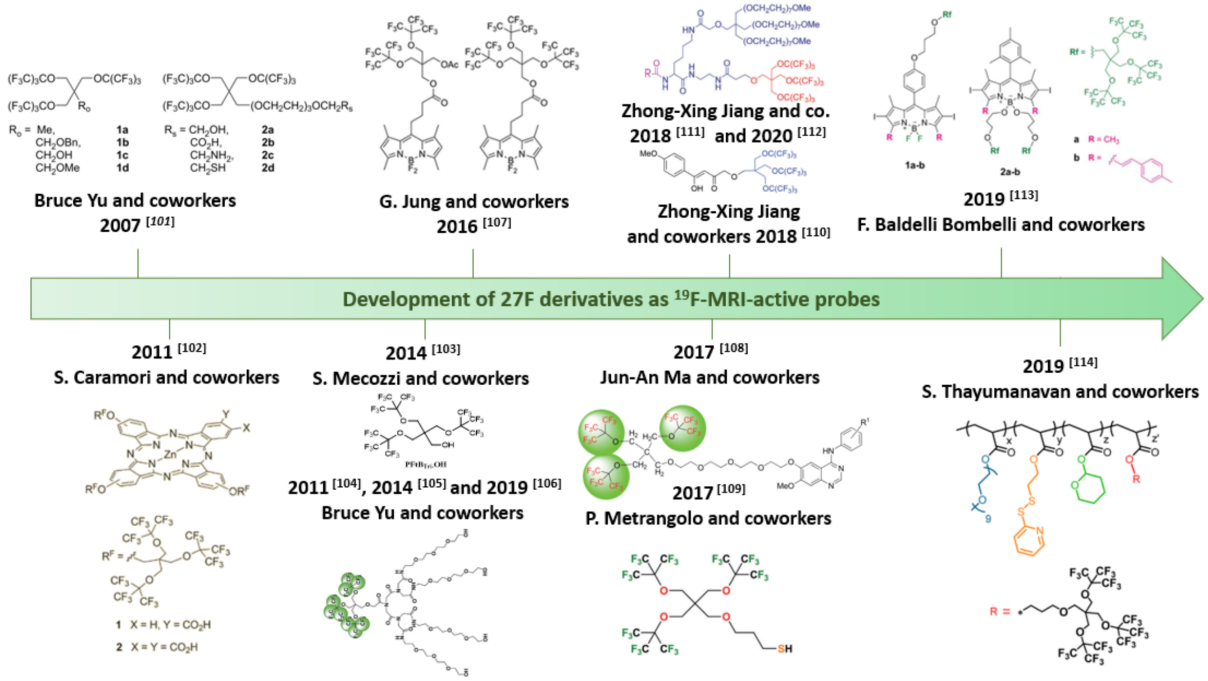

Figure 1.30: Development of new fluorinated 19F-MRI active probes with 27 equivalent fluorine atoms (27-F) [72–85].

2 | Purpose of the research

Due to their excellent photovoltaic performances and low fabrication costs, Perovskite Solar Cells (PSCs) are considered the most promising next-generation photovoltaics for large-scale commercialization. Their power conversion efficiency (PCE) has rapidly improved to 25.2% in only one decade [5]. The rapid advancement of perovskites in photovoltaics has captured the interest of scientists from a variety of fields, and the initial enthusiasm has been bolstered by research into their structural, optical, and electronic properties. Despite all characteristics and properties matching the requirements in optoelectronic field, there are still two main challenges to overcome: the toxicity, caused by the presence of lead in perovskite, and their low stability to atmospheric agents. Due to these main limitations PSCs have not yet met the requirements for commercialization, making it difficult for researchers to create devices that are both efficient and stable [12]. It is generally accepted that the presence of defects, both at the surface or in the bulk, is critical for the long-term stability and considerably limits perovskite efficiency. In order to realize PSCs with both high photovoltaic performance and operational stability, various functional materials have been developed to assist in obtaining high-quality perovskite films. Ionic liquids (ILs), which are essentially a class of salts with a melting point below 100 °C, have recently been investigated for use in PSCs, with remarkable progress made. ILs are novel alternatives to conventional materials. Notably, they have been extensively studied in the field of PSCs and various functions (Figure 2.1) in realizing efficient and stable PSCs devices, such as nucleation and crystal growth control, reduced interface-related energy loss, stability improvement have been demonstrated [86]. Furthermore, fluorinated ionic liquid crystals (ILCs) are promising materials for applications as quasi-solid electrolytes in dye-sensitized solar cells [87] and many other optoelectronic devices. Fluorination is a powerful tool for controlling the self-assembly behavior of materials, which has a positive effect on charge mobility. As previously described, these functional groups take advantage of the self-assembly effect induced by the interaction of the fluorinated phase. In fact, fluorinated cations can accumulate on the surface of perovskite at grain boundaries, where polyfluoroalkyl chains form a hydrophobic barrier against moisture, thereby delaying decomposition processes. Moreover, imidazolium salts with

perfluoroalkyl chains are used as passivating agents for low dimensional perovskites in order to adjust their optoelectronic properties and increase their stability. Perfluoroalkyl chains are interesting functional groups thanks to their effect on electronic structure on conjugated cations [47, 57].

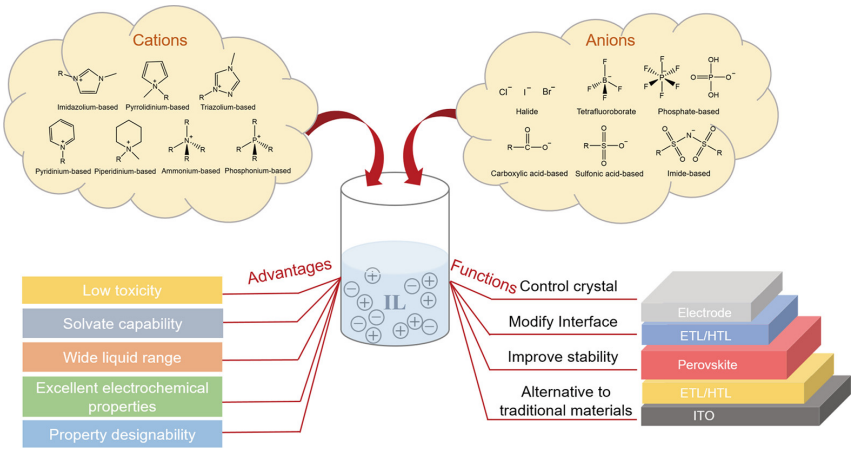

Figure 2.1: Composition, characteristics, and functions of ILs in PSCs are illustrated [86].

Despite the enhanced performance, the mechanism of passivation and the structural implications of the perovskite's crystal structure remain poorly understood. In addition, the inherent liquid-crystal properties of imidazolium-based fluorinated ionic liquids in conjunction with metal halide perovskites have not yet been investigated. To completely exploit the beneficial effect of fluorination in tailoring the physical and functional properties of perovskites, a deeper understanding of how fluorinated ionic liquid crystals (FILCs) influence perovskite structure-property relationships is essential. Perfluoroalkyl-methyl imidazolium molecules were chosen due to their previously analyzed self-assembly properties, which result in the liquid crystal (LC) behavior described for imidazolium iodide salts. The objective of this experimental work is to examine these cations within perovksite structures. The aim is to synthesize and thoroughly characterize low-dimensional lead iodide perovskites containing perfluoroalkyl imidazolium cations. In particular, the linear perfluoroalkyl-methyl imidazolium iodide salt (LinF-MeIMI, Figure 2.2) was the first to be synthesized because it is a well-known compound that our research team (Supra-BioNanoLab, Politecnico di Milano) had previously obtained and studied [88]. The LC properties of the LinF-MeIMI salt are known, but it has never been utilized as a cation in perovskites. Therefore, the objective was to determine whether the known tendency of fluorinated chains to segregate can influence the crystallization processes of perovskites.

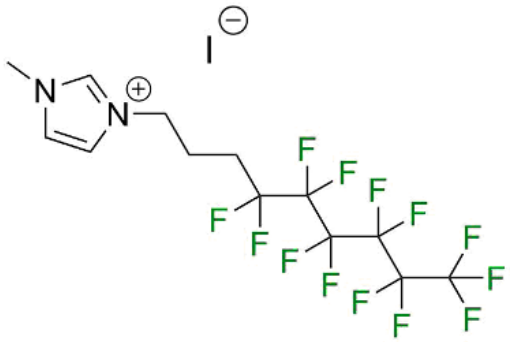

LinF-MImI

Figure 2.2: Chemical structure of the linear perfluoroalkyl-methyl imidazolium iodide salt (LinF-MeIMI).

Moreover, it has to be mentioned and we should be aware that perluoroalkyl compounds with chains longer than six carbon atoms are raising concerns about their suspected toxicity and are therefore being banned due to their environmental impact and bioaccumulative potential. So, alternatives have to be found and because of that a multibranched fluorinated imidazolium iodide salt (BrF-MeImI, Figure 2.3) has been designed.

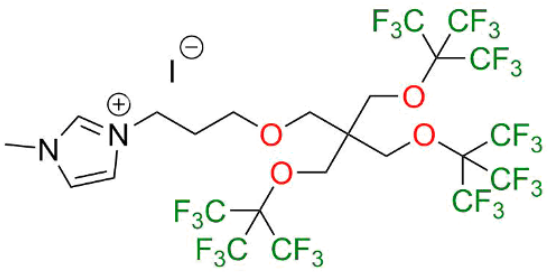

BrF-MImI

Figure 2.3: Chemical structure of the branched perfluoroalkyl-methyl imidazolium iodide salt (BrF-MeIMI).

This innovative structure allows us to increase the number of fluorine atoms in the molecule (27 F atoms per molecule), resulting in a high fluorine density on the surface and a low surface free energy. In addition, the presence of four ether bonds in the core may accelerate molecular degradation in the environment due to the cleavage of such

bonds under physiological conditions, thereby resolving bioaccumulation concerns [89]. The branched perfluorinated molecules used is a derivative of the already known fluorinated molecule Perfecta (empirical formula: $C_{21}H_8F_36O_4$), which is depicted in Figure 2.4 [71].

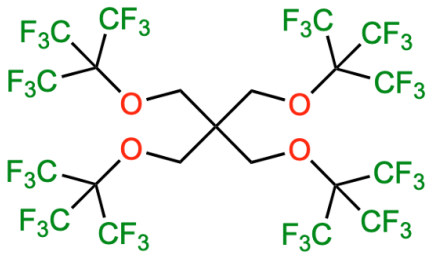

Figure 2.4: Chemical structure of Perfecta.

The main aim of this research activity is try to understand the effect of linear and branched fluorinated chains on crystallization process in hybrid organic-inorganic halide perovskites. To this pourpose, the above mentioned imidazolium salts were applied for the synthesis of two distinct perovskites starting from lead iodide (Figure 2.5).

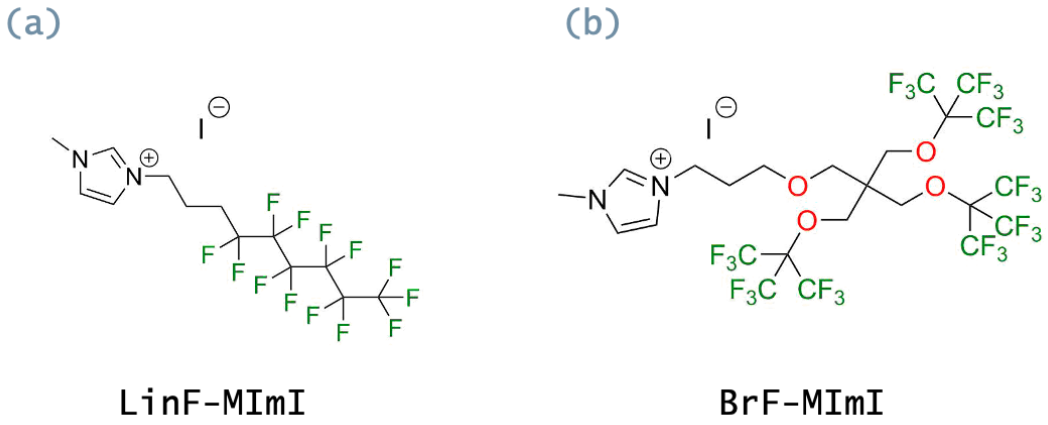

Figure 2.5: Chemical structure of the (a) linear perfluoroalkyl imidazolium cation (LinF-MeIM) and (b) branched perfluoroalkyl imidazolium cation (BrF-MeIm).

Both the imidazolium salts reacted with lead iodide, which is currently the most widely used reagent in the perovskite field because it produces more stable materials. This can allow to better evaluate the efficacy of fluorinated ligands. The main disadvantage of lead is its toxicity, but if positive results are obtained, the fluorinated imidazoles can be induced to react with other non-toxic metals, like Sn.

A multibranched fluorinated ammonium salt (BrF-NH_3^+, Figure 2.6) has been also applied as cation for the synthesis of perovskites, with the aim to understand the effect of different ammonium salts (primary ammonium versus imidazolium) on the final structure. Perfluorinated ammonium salts have been also reported as passivating agents [42]. Also this molecule is a Perfecta derivative and it was obtained as an intermediate during the synthesis of the branched fluorinated imidazolium cation, as described in the chapter 4. The purpose of this synthesis was to establish whether or not the variety of cation can have an effect on the final crystal structure of the perovskite.

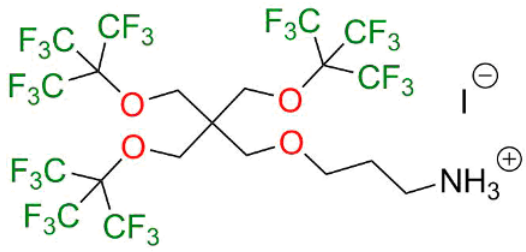

BrF-NH_3^+

Figure 2.6: Chemical structure of the multibranched fluorinated ammonium salt (BrF-NH_3^+).

As mentioned previously, the first part of this work concentrates on the various synthesis techniques that were employed to create the final perovskites. In a subsequent phase, all the salts and the perovskites made with fluorinated imidazolium cations were characterized. In addition, single crystals of the perovskite with linear perfluoroalkyl imidazolium cation (PbI_2):(LinF-MImI) were collected and analyzed using X-ray diffraction (XRD) at a synchrotron (Elettra Sincrotrone Trieste). These data have enabled the discovery of important informations regarding the relationship between the structures and properties of perovskites.

3 | Results and discussion

3.1. Molecule design

As was previously stated, the stability of perovskite materials under various degradation stresses is still the limiting factor for their commercialization. Several strategies have been proposed to surmount these obstacles, including low-dimensional perovskites, surface treatment, and additives in precursors. Due to their unique properties, such as low volatility, high ionic conductivity, and electrochemical stability, ionic liquids (ILs) have emerged as a promising class of additives for enhancing device performance. In particular, imidazolium-based ionic liquids have been applied as additive in perovkite precursor solutions in order to bind undercoordinated halide anions. The imidazolium unit can also be functionalized with various alkyl or fluorocarbon chains, which produce a significant hydrophobic effect on the material [51, 86]. In fact, fluorination of organic cations is an intriguing strategy to increase idrophobicity while tuning self-assembly and optoelectronic properties of low-dimensional perovskites. In fact, the presence of highly fluorinated saturated molecular fragments in the resulting low-dimensional perovskite can confer additional water-repellent properties and superior stability compared to the hydrocarbon-based cations previously employed [42]. From the best of our knowledge, the reaction between fluorinated imidazolium salts and PbI_2 has never been studied in detail. The purpose of this research is therefore to investigate if the presence of fluorinated imidazolium cations can affect crystallization process in perovskites and reduce the presence of defects. Figure 3.1 shows the three compounds chosen for the synthesis of perovskites: two imidazolium salts and a multibranched fluorinated ammonium salt. It was decided to synthesize a multibranched fluorinated imidazolium cation as an eco-friendly alternative to perluoroalkyl compounds with carbon chains longer than six atoms, whose environmental impact and bioaccumulative potential are causing concerns. This structure allows us to increase the number of fluorine atoms in the molecule and, in addition, the presence of four ether bonds in the core may expedite molecular degradation in the environment as a result of bond cleavage, thereby alleviating bioaccumulation concerns [89]. Furthermore, the multibranched fluorinated amine was also synthesized in order to investigate

the effect of different ammonium salt (imidazolium vs primary ammonium) on the final crystal structure of the perovskite.

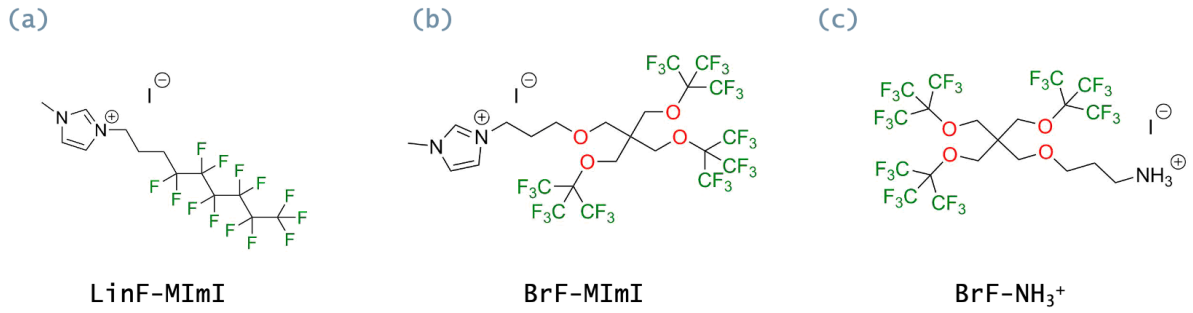

Figure 3.1: Chemical structure respectively of: (a) linear perfluoroalkyl methylimidazolium iodide (LinF-MImI), (b) multibranched fluorinated methylimidazolium iodide (BrF-MImI) and (c) multibranched fluorinated ammonium salt (BrF-NH_3^+).

Due to the dimensions of these organic molecules, a low-dimensional perovskite structure can be predicted from the beginning. In fact, the Goldschmidt tolerance factor (t) can be used to evaluate the structural probability and crystallographic stability of the perovskite.

$$\mathrm{t} = \frac{R_A + R_X}{\sqrt{2}(R_B + R_X)} \tag{3.1}$$

where R_A, R_B, and R_X are the ion radii corresponding to A (organic cation), B (Pb cation), and X (I anion) ions, respectively [12].
It is known that when the t value is greater than 1, it indicates that the A-site cations are too large to have an octahedral framework (3D) and 2D layered structures, one dimensional (1D) chain structures or even zero dimensional (0D) isolated clusters can be formed [13].

3.1.1. (PbI_2):(LinF-MImI) and (PbI_2):(BrF-MetImI)

In order to synthesize perovskite with two distinct imidazolium fluorinated cations, various reaction steps were performed. Following a well-established procedure described in the chapter 4, the two different salts depicted in Figure 3.2 were first obtained by nucleophilic addition of the corrispective linear and branched iodo-polyfluorinated compounds to 1-methyl imidazole in toluene. These salts were used as starting reagents to obtain two different perovskites respectively with a linear fluorinated imidazolium cation and with branched fluorinated imidazolium cation which have been both characterised by NMR, FTIR, TGA, POM, DSC and SAXS analyses.

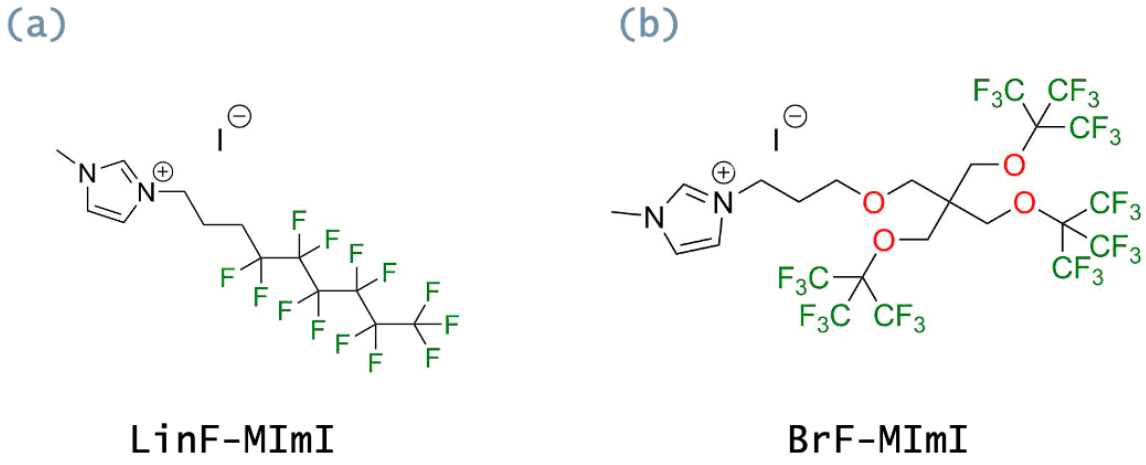

Figure 3.2: Chemical structure of (a) linear perfluoroalkyl imidazolium salt (LinF-MetImI) and (b) branched perfluoroalkyl imidazolium salt (BrF-MetImI).

Perovskite syntheses were first of all carried out following the procedure described by Seth et al. using the imidazolium iodide and PbI_2 with molar ratio (PbI_2):(LinF-MImI) [2:1] in the presence of an excess of Hydroiodic acid 57% w/w solution stabilized with 1.5% hypophosphorous acid [90]. The reaction was kept at 110°C for 24 hours under stirring and nitrogen atmosphere. Some precipitate was obtained and it was filtered at Buckner, to obtain a yellow powder. Afterwards, in order to optimize the perovskite synthesis and verify the influence of the molar ratio between the initial reagents on the chemical structure of the product, different reactions with the same reagents, but different conditions were performed (reported in Table 3.1).

Table 3.1: Different experiment conditions for the perovskite's powders (EX = large excess; DR = few droplets).

	Eq. PbI_2	Eq. LinF-MImI	Eq. HI	Eq. H_3PO_2	T	Time
(PbI_2):(LinF−MImI)[1:2][I]	1	2	EX	/	100°C	24h
(PbI_2):(LinF−MImI)[1:2][II]	1	2	EX	DR	120°C	24h
(PbI_2):(LinF−MImI)[1:2]	1	2	EX	DR	120°C	1-2h
(PbI_2):(LinF−MImI)[1:4]	1	4	EX	DR	120°C	1-2h
(PbI_2):(LinF−MImI)[1:1]	1	1	EX	DR	120°C	1-2h

It has to be mentioned that in the first reaction was evident the presence of a dark byproduct due to the iodide oxidation, so the addition of a solution of H_3PO_2 (50 wt.% in H_2O) in the following reactions was necessary in order to prevent this oxidation. Immediately after the addition of H_3PO_2 the solution became transparent and the black byproduct was not present anymore. In contrast to the reaction reported by Seth et al. the temperature during stirring was increased to 120 °C to enhance solubility. The reaction mixture was cooled down with a rate of 10°C/h. The day after, the final products were filtrated in Buckner with ethanol obtaining in all the cases a yellow powder, as shown in Figure 3.3.

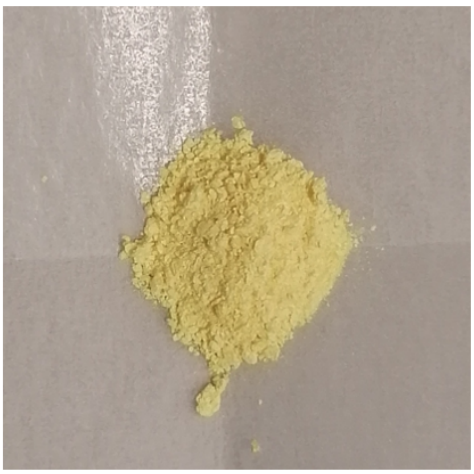

Figure 3.3: Picture of the perovskite powder (PbI_2):(LinF-MImI) after the work-up.

All of these samples underwent an attempt at crystallisation, as the experimental work's primary objective was to investigate their crystalline structure. The compounds were synthesized again with different molar ratios between the initial reagents, and the reaction conditions were altered with the aim of obtaining crystals. In the following table (Table 3.2) all the different conditions used are reported.

Table 3.2: Different experiment conditions for the perovskite crystals (EX = large excess; DR = few droplets).

	Eq. PbI_2	Eq. $C_9F_{13}MImI^-$	Eq. HI	Eq. H_3PO_2	T	Time
(PbI_2):(LinF−MImI)[2:1]	1	2	EX	DR	130°C	24h
(PbI_2):(LinF−MImI)[4:1]	1	4	EX	DR	130°C	24h
(PbI_2):(LinF−MImI)[1:1]	1	1	EX	DR	130°C	24h

In these cases, the fundamental difference has been the cooling rate. The reactions were first heated to 130°C to obtain a clear solution enhancing the solubility, then they were left to cool down slowly until the solution became opaque around 100°C. The reaction mixture remained at this temperature overnight and in the next days the temperature was decreased with a controlled cooling rate of 2°C/h. When the solutions reached the room temperature, some thin crystals precipitated at the bottom of the flask. The platelets were collected, dried under vacuum in a sintered glass funnel with the aim of removing the acid mother liquor and subsequently they were washed with methanol. For all the three reactions performed with different molar ratios, as it is reported in Figure 3.4, shiny yellow crystals were obtained.

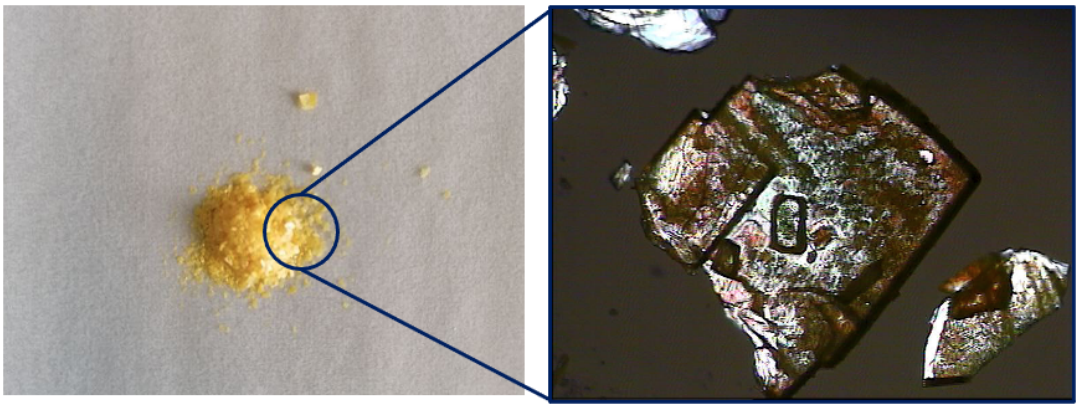

Figure 3.4: Photo and POM image of the crystals obtained.

Following the same conditions of the syntheses previously made, the branched imidazolium salt was firstly dissolved in methanol (since it was insoluble in the acid) and then added in a tube flask together with the lead iodide in an excess of hydroiodic acid (HI, 150eq), always with the addition of hypophosphorous acid solution (50 wt.% in H_2O) to prevent the iodide oxidation (Table 4.18). Immediately a solid was formed floating in the centre of the flask. The solid in the solution was stirred overnight at a temperature of 120°C. The following day, the solid was filtered with nitrogen flux and Buckner. Under these

conditions, the resulting substance was amorphous and viscous. To crystallize the solid, I dissolved it in acetonitrile in a vial, heated the solution to 60°C, and then gently cooled it to 25°C before storing it overnight in the refrigerator. I obtained sharp needles of the ultimate product in this manner (Figure 3.5). The solvent was then allowed to evaporate, after which the needles were gathered and washed with methanol.

Figure 3.5: Picture of the (PbI_2):(BrF-MImI) needles after the crystallisation in acetonitrile.

3.1.2. (PbI_2):(BrF-NH_2)

As indicated previously, an attempt to obtain a new hybrid organic-inorganic metal halide perovskite with a different fluorinated cation was also made. In the chapter 4, all the reaction steps required to produce the multibranched fluorinated amine depicted in Figure 3.6 are described in detail.

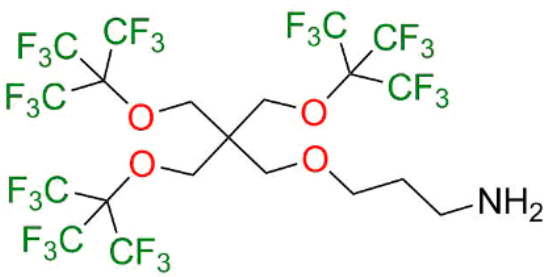

Figure 3.6: Chemical structure of the multibranched fluorinated amine (BrF-NH_2).

The plan was to use the same reaction procedure as with the imidazolium salts, with the exception that the amine would react directly in the hydroiodic acid to form the branched fluorinated ammonium salt, which would then react with the lead iodide in situ. As with previous reactions, the reagents were placed in a tube flask with an excess of hydroiodic acid and a hypophosphorous acid solution (50 wt.% in H_2O). The solution stirred at 120°C for 48 hours. Since the amine was insoluble in HI, it must be mentioned that it has been dissolved in methanol. Finally, the yellow powder depicted in Figure 3.7 was obtained by filtration with Buchner under nitrogen flow.

Figure 3.7: Picture of the final product (PbI_2):($BrF\text{-}NH_2$) after the work-up.

3.2. Structural characterization

3.2.1. (PbI_2):(LinF-MImI)

X-ray diffraction (XRD) analysis

Small needle shaped single crystals were obtained for the perovskites containing the LinF-MIm cation and were analyzed by synchrotron X-ray diffraction. The synchrotron is a type of circular particle accelerator that works by accelerating charged particles (electrons) through sequences of bending magnets until they reach almost the speed of light.

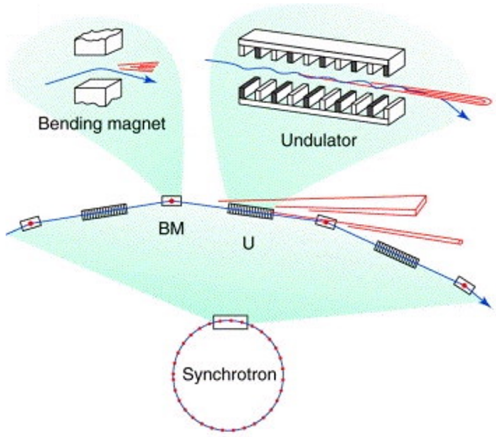

Figure 3.8: Schematic illustration of radiation producing magnetic devices in one synchrotron sector. A synchrotron storage ring with 40 sectors is shown at the bottom, an excerpt containing three straight sections is shown in the middle, and details from a bending magnet and an undulator are shown at the top. BM, dipole bending magnet; U, undulator array. As electrons (blue) are accelerated through a magnet at high energy they emit X-rays (red) instantaneously into a narrow cone of $\sim 0.004°$ [91].

These fast-moving electrons produce electromagnetic radiations (ranging in the X-ray spectrum), called synchrotron light. This very intense light can be used to study minute matter such as atoms and molecules and allows us to collect a complete data set from a single crystal [91, 92].

X-ray diffraction analysis revealed the same chemical structure for all the analyzed crystals (Table 3.2) regardless the stoichiometry (PbI_2):(LinF-MImI) used for the synthesis. In particular all the sample show a chemical formula, with a (PbI_2):(LinF-MImI)[1:2] stoichiometry. X-ray structure show only the presence of discrete $(Pb_3I_{12})^{6-}$ anions surrounded by six $(LinF\text{-}MIm)^{+}$ cations.

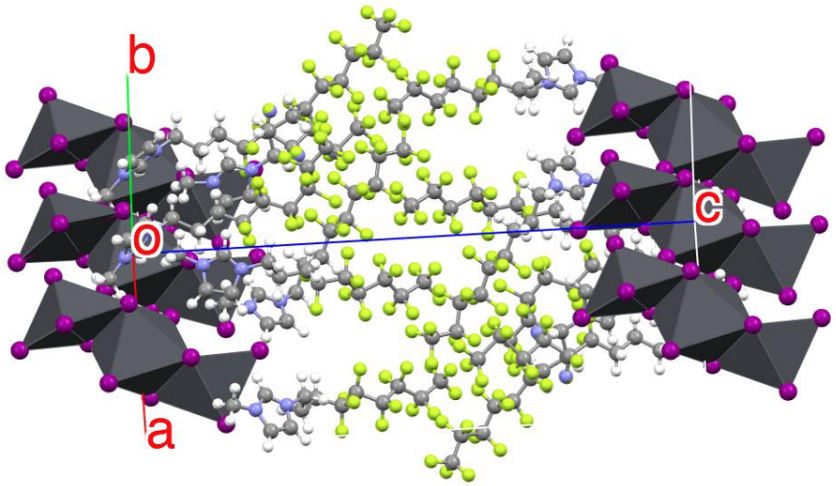

Figure 3.9: Crystal structure of the $(Pb_3I_{12})^{6-}$ $(LinF\text{-}MIm)^{+}{}_6$ low-dimentional perovskite. Colour code: gray = C, white = H, blue = N, yellowish green = F, purple = I.

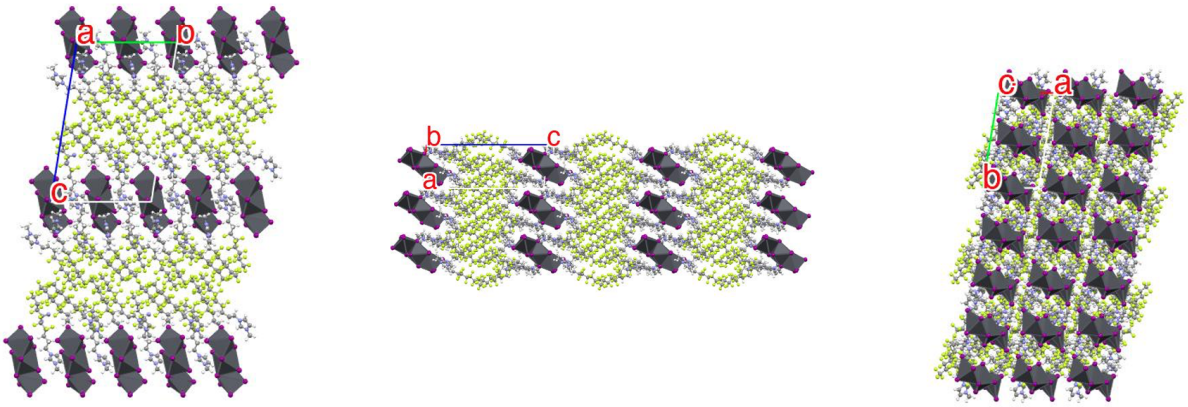

Figure 3.10: Crystal structure of the $(Pb_3I_{12})^{6-}$ $(LinF\text{-}MIm)^{+}{}_6$ low dimentional perovskite: view along a, b and c axes. Colour code: gray = C, white = H, blue = N, yellowish green = F, purple = I.

Each Pb^{2+} cation within the trinuclear cluster is hexacoordinated by six iodine atoms and assumes a distorted octahedral geometry. The six iodine anions surrounding the central Pb^{2+} cation form a face-sharing connection between the PbI_6 octahedra within the trinuclear cluster. The Pb-I bond lengths range from 3.083 to 3.304, with the terminal Pb-I bonds (3.083 to 3.149) being shorter than the middle ones (3.175-2.304). The Pb $\cdots$ Pb distance is 4.079 Å. The trinuclear cluster anions $Pb_3I_{12}{}^{-6}$ are connected through hydrogen bonds with methylene and methyl groups of the cation (Figure 3.11).

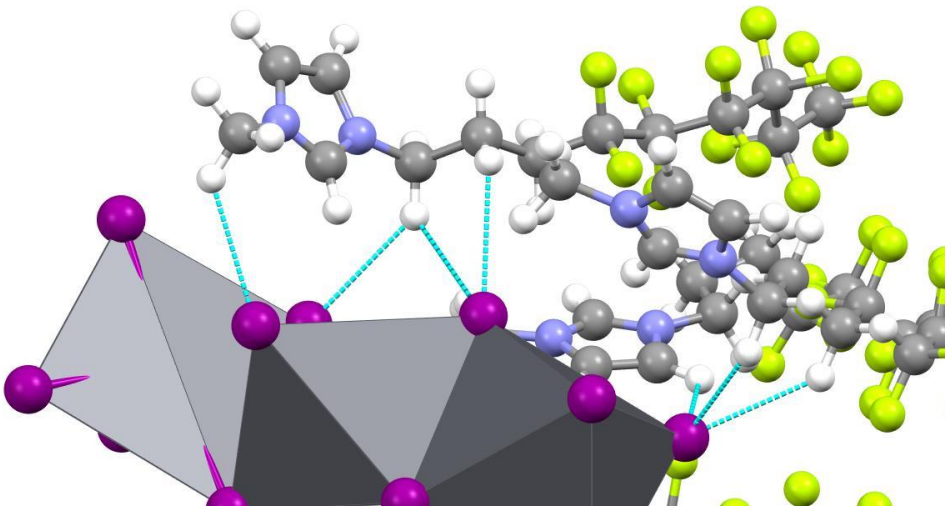

Figure 3.11: Visual representation of the hydrogen bonds between the inorganic clusters and the methylene and methyl groups of the imidazolium cation. Colour code: gray = C, white = H, blue = N, yellowish green = F, purple = I.

Florous-florous interactions give rise to a partial interdigitation and segregation of fluorinated chains (Figure 3.12). This interaction pattern enables the nanoscale separation of fluorinated chains and inorganic clusters into a lamellar structure (visible in Figure 3.10). Further details about crystallographic structure are present in Table A.1.

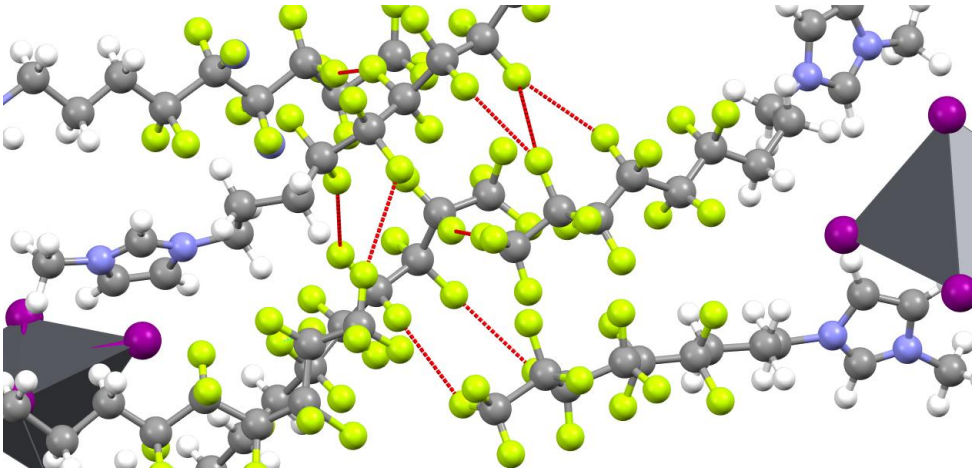

Figure 3.12: Visual representation of F $\cdots$ F interactions between the fluorinated chains of the linear imidazolium cations. Colour code: gray = C, white = H, blue = N, yellowish green = F, purple = I.

Powder X-Ray Diffraction (PXRD) spectra were also collected. Specifically the spectrum of the perfluoroalkyl-methyl imidazolium lead iodide perovskite was compared to diffractograms of initial regents: lead (II) iodide and imidazolium iodide salt. As depicted in

Figure 3.13 for (PbI_2):(LinF-MImI), the absence of peaks typical of lead iodide and the starting LinF-MImI, and the appearence of new peaks indicated a successful synthesis devoid of remaining imidazolium or lead iodide impurities.

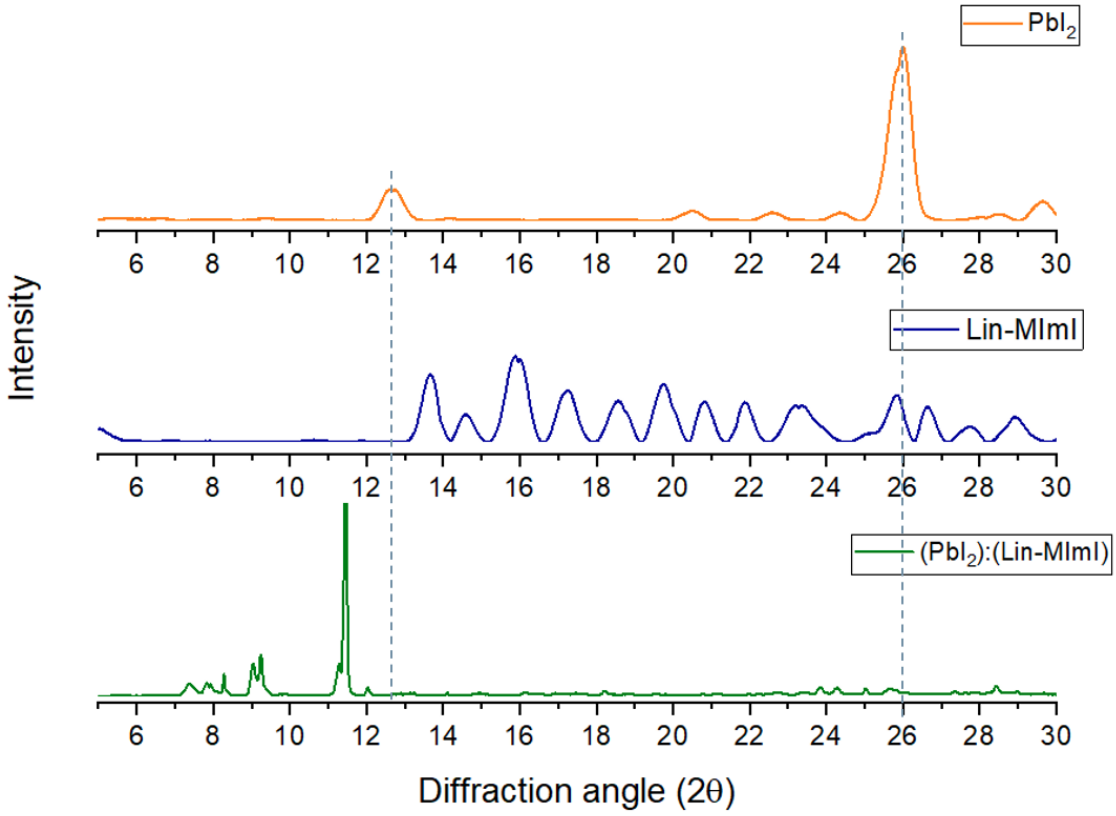

Figure 3.13: Powder XRD spectra comparison among lead (II) iodide, LinF-MImI and the (PbI_2):(LinF-MImI) perovskite.

To confirm that the structure of the single crystal obtained is identical to that of the bulk material, the PXRD spectrum of the (PbI_2):(LinF-MImI) sample has been compared to the simulated spectrum calculated by the cristallographic software Mercury.

As shown in Figure 3.14, the spectrum is compatible with that of the bulk material since the peaks obtained from the single crystal studied are in the same values of 2θ. After the reaction with lead iodide, it can be observed the formation of a series of peaks between 7° and 12°. Using Bragg's law, each peak has been correlated with the interatomic distance d, which is the spacing between the various diffracting planes in the crystal (Table 3.3).

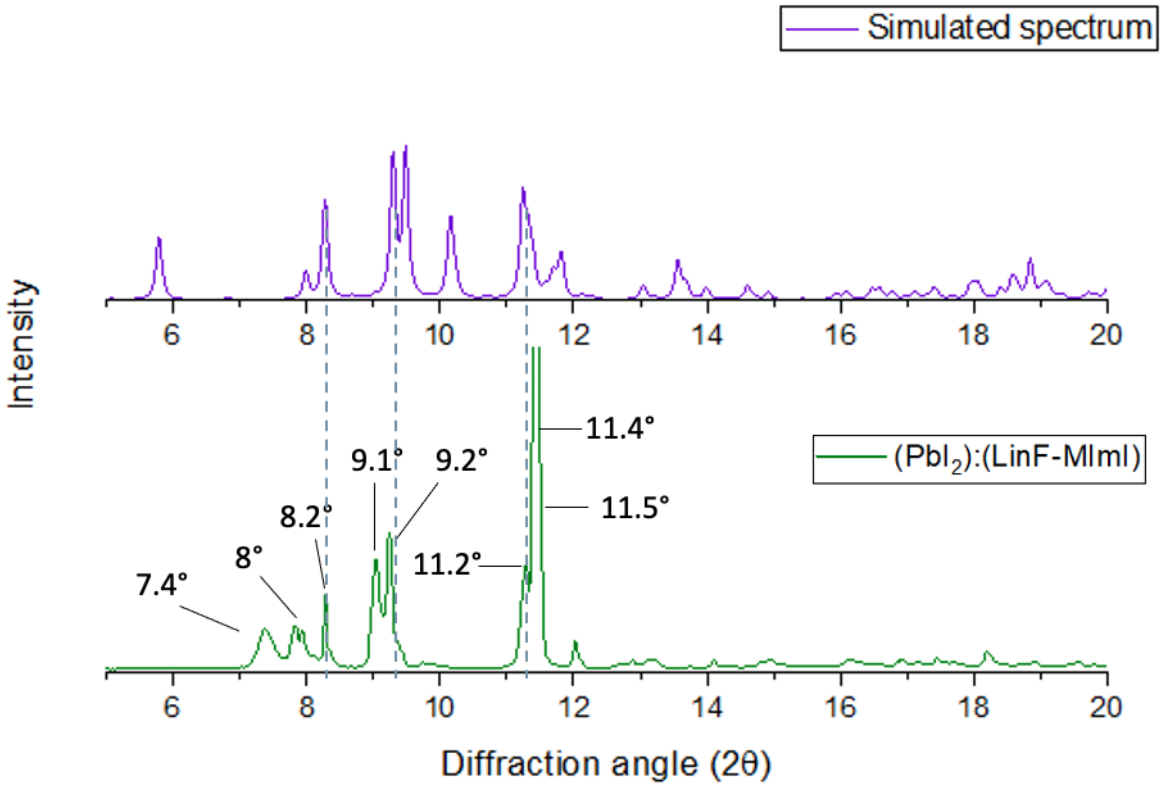

Figure 3.14: Comparison between the experimental PXRD spectrum of the (PbI_2):(LinF-MImI) sample and the simulated bulk PXRD spectrum.

Table 3.3: Characteristic diffaction peaks of the (PbI_2):(LinF-MImI) perovskite with the relative crystallographic planes.

Diffraction angles (2θ)	**Miller indeces (h,k,l)**	**d spacing [Å]**
7.4°	(0,1,-2)	12
8°	(1,0,0)	11
8.2°	(1,0,-1)	10.7
9.1°	(0,2,0)	9.7
9.2°	(1,0,-2)	9.5
11.2°	(1,-2,0)	7.8
11.4°	(1,0,-3)	7.78
11.5°	(1,-2,1)	7.77

Three distinct regions were analyzed:

- **Between 7° and 9°** three peaks are visible. The first at 7.4° corresponds to the plane with Miller indeces (0,1,-2) while the other two correspond to the (1,0,0) and (1,0,-1) planes at 8° and 8.2°, respectively.

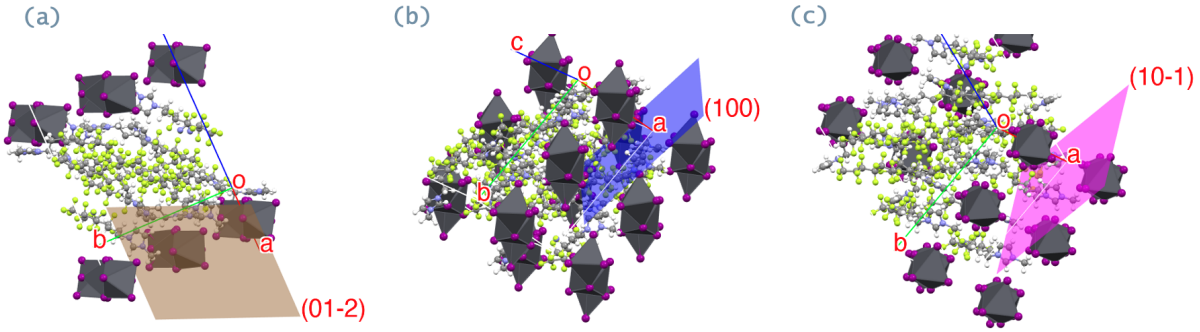

Figure 3.15: Visual representation of the (0,1,-2), (1,0,0) and (1,0,-1) planes associated through the cristallographic software Mercury to the peaks at 7.4°, 8° and 8.2°.

- **Around 9°** two distinct peaks are formed, the first at 9.1° and related to the (0,2,0) plane at half the b-axis length, and the second at 9.2° and related to the (1,0,-2) plane.

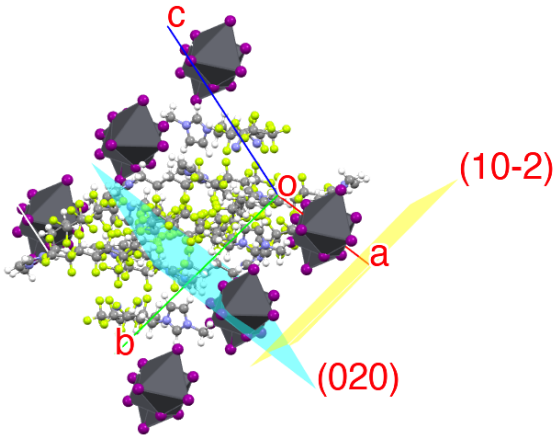

Figure 3.16: Visual representation of the (0,2,0) and (1,0,-2) planes associated through the cristallographic software Mercury to the peaks at 9.1° and 9.2°.

- **A peak between 11.4° and 11.5°** that is the most prominent in the crystal sample. In this region of 2θ, different planes can be found. Presumably, the diffraction peaks associated with these planes are superimposed. Notably, the (1,0,-3) and (1,-2,1) planes contain iodine elements from the perovskite's inorganic octahedra.

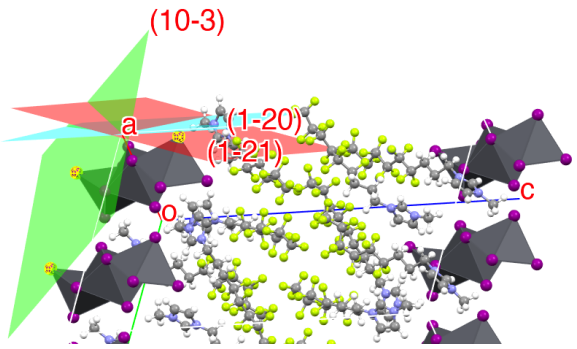

Figure 3.17: Visual representation of the (1,0,-3) and (1,-2,1) planes associated through the cristallographic software Mercury to the peaks around 11.5°.

In conclusion, as a result of the large size of the octahedra anions a series of peaks are formed between 7° and 12°, which correspond to greater d-spacing values between the planes compared to the imidazolium salt LinF-MImI. These peaks can be attributed to the spatial distribution of perfluoroalkyl chains and their orientation in the crystalline structure.

Fourier transformed Infrared spectroscopy (FTIR)

The Fourier transformed infrared spectra of imidazolium salts were examined to determine how the interaction with lead (II) iodide modifies their vibrational modes. The interactions of these cations can therefore be evaluated as successful. First, the distinctive signals of the imidazolium salts utilized in this study must be identified. Consequently, it is evident which wavenumbers can generate a specific signal for identifying imidazolium cations and their interactions with lead halide octahedra. As shown in Figure 3.18, methyl-imidazolium iodide salt with linear fluorinated chain (LinF-MImI) FTIR main signals can be analyzed in three key regions:

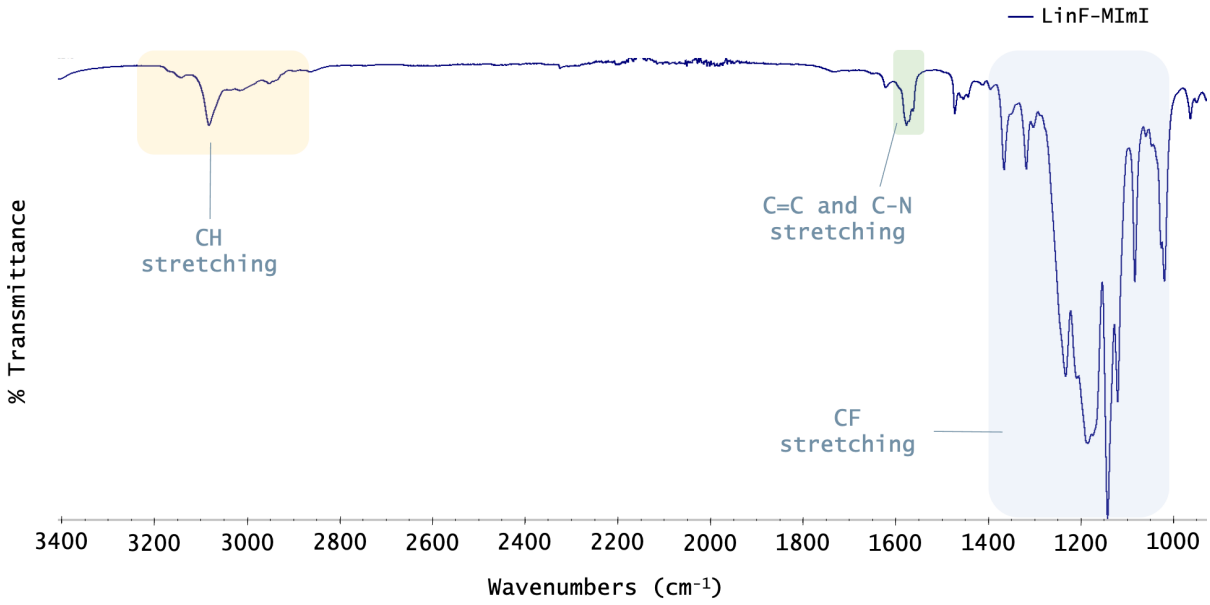

Figure 3.18: LinF-MImI FTIR spectrum with main bands.

1. **At wavenumbers higher than 2800 cm^{-1}**, signals are caused from C-H stretching modes of imidazolium ring and alkyl chains (Figure 3.19) [93, 94]. Features above 3000 cm^{-1} were from the CH vibrational modes of the imidazolium ring (antisymmetric/symmetric stretch of HC(3)=C(4)H and C(2)H stretch vibrational modes). Especially the peak at 3142 can be associated to H-C(3)=C(4)-H stretching modes (Figure 3.19). These signals can be modified with change of anions with respect to I^- [95]. While in the region between 2800-3000 cm^{-1} there are signals created by CH symmetric or asymmetric stretching of alkyl spacers with fluorinated part, as shown in Figure 3.19. These signals, which change with different alkyl chains, can be used to asses that the reaction occurred. It has to be mentioned that the CH_3 group in position (6) creates a signal between 3100 and 2900 cm^{-1} (peak at 2952 in Figure 3.19) which is prone to modification upon interaction with lead.

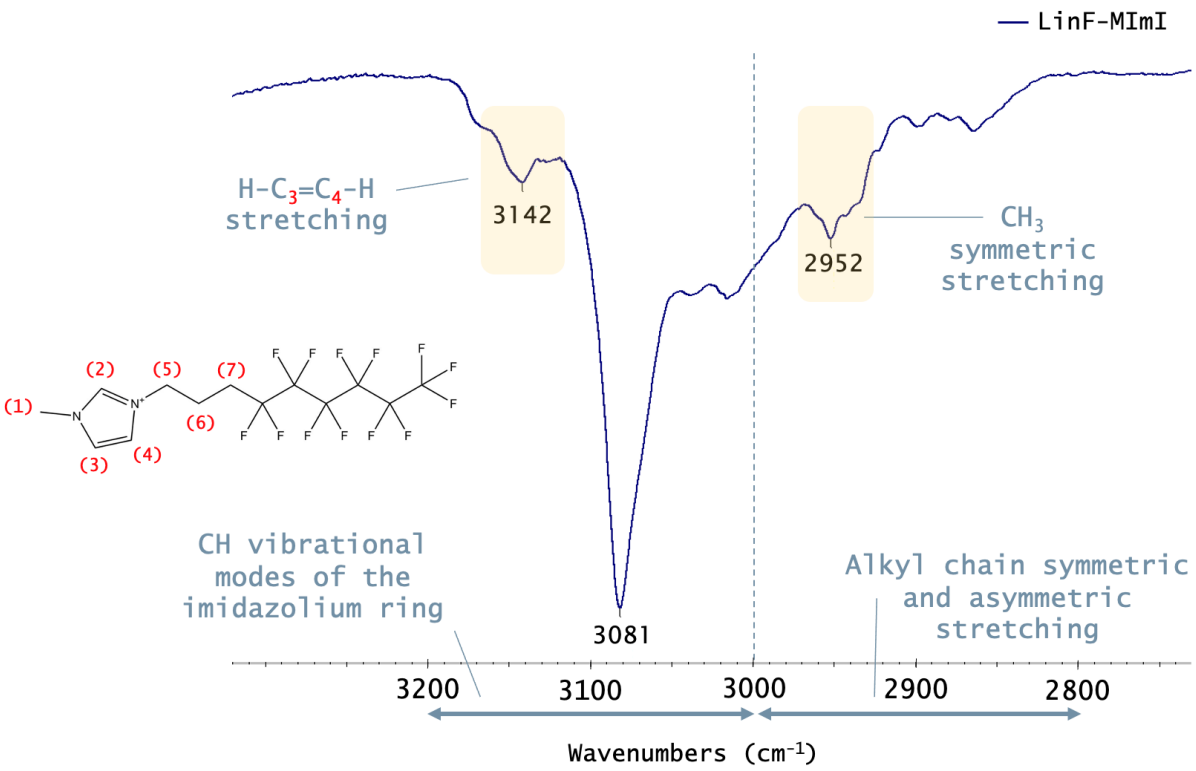

Figure 3.19: LinF-MImI CH stretching signals.

2. **Between 1550cm^{-1} and 1600cm^{-1}**, a significant peak related to imidazolium ring is present, as shown in Figure 3.20 [93]. It can be correlated to ring in-plane (ip) symmetric and asymmetric (sym/asym) stretching, CH3(N) and CH2(N) CN stretching modes [96] which are affected by ionic interaction among the fluorinated methyl imidazolium cation and inorganic sublattice as reported by Jerman et al. [95].

3. **From 1000 cm^{-1} to 1400 cm^{-1}**. In this region the FTIR spectrum shows peaks of alkyl chain rocking (1400-1300 cm^{-1}) and twist (1100-1000 cm^{-1}), but these peaks are not useful to analyze imidazolium reaction. In this region are the CF stretching signals create very strong bands dependent in terms of peaks and wavenumber on fluorine atoms (Figure 3.20). This region is particularly interesting since usually CF_2 and CF_3 stretching signals create strong bands in this region between 1400-1000 $^{-1}$. These signals are dependent on fluorinated carbon in the imidazolium cation, and they overlap other signals that can be made by CF_2 chains deformation and vibration and CF_3 rocking and wagging [97, 98].

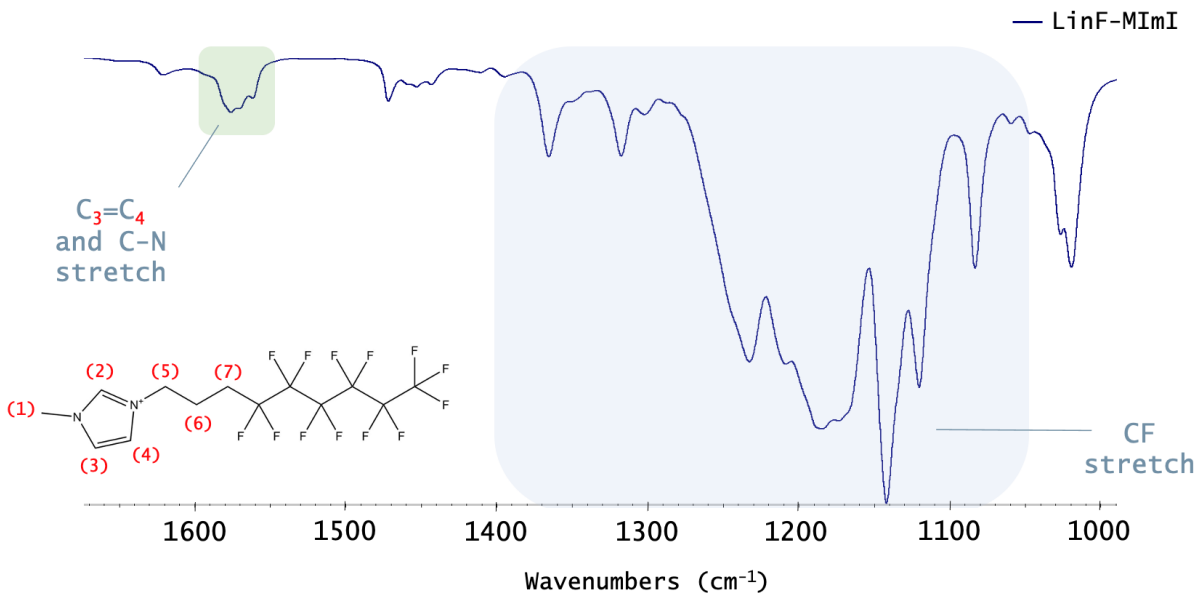

Figure 3.20: C=C, C-N and CF stretching FTIR signals of the LinF-MImI.

A comparison between the spectra of the imidazolium salt (LinF-MImI) and the (PbI_2):(LinF-MImI) perovskite samples was performed in order to demonstrate how the arrangement of the imidazolium salt with lead iodide can be verified by FTIR spectral analysis. The interaction between the imidazolium salt and lead iodide can be carried out due to:

1. **Change of signals in 2800-3200 cm^{-1} region related to CH stretching band**: these changes are induced by ionic interaction. In the perovskite, C-H vibrations can be modified due to the establishment of H-bond interactions between the C-H groups on the imidazolium cation and the lead iodide [99, 100]. These interactions modify the stretching modes of CH_3 and HC(3)=C(4)H shifting them at lower wavenumbers, as shown in Figure 3.21. This effect, together with modification of other C-H stretching signals (the peak at 3081 separates in two different peaks at sliglthy higher wavenumbers), gives a first clue for the occurrence of the chemical reaction (Table 3.4).

2. **Change of imidazolium ring stretching in 1500-1600 cm^{-1} region**. A single peak for imidazolium iodide salts is present in this region and it is related to the skeleton vibration peak of the aromatic ring (1576 cm^1). It is found that this peak is split into two peaks at 1571 and 1558 cm^1, which indicates that the electron cloud density of the imidazole ring has been changed (Figure 3.22) [61, 95]. In addition, both peaks are at lower wavenumbers with respect to initial imidazolium peak.

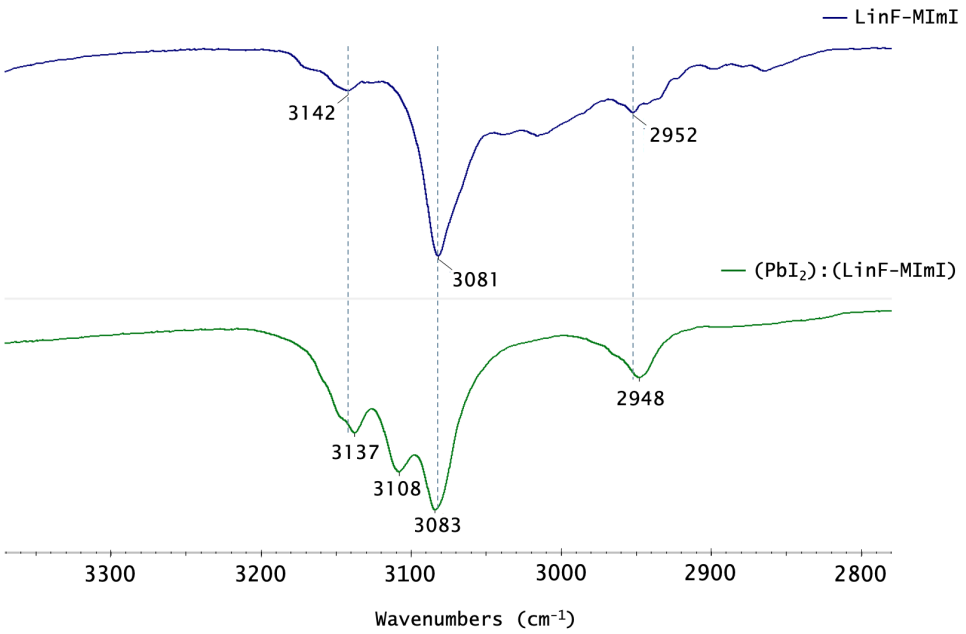

Figure 3.21: FTIR spectra comparison between LinF-MImI and (PbI_2):(LinF-MImI) in CH stretching region.

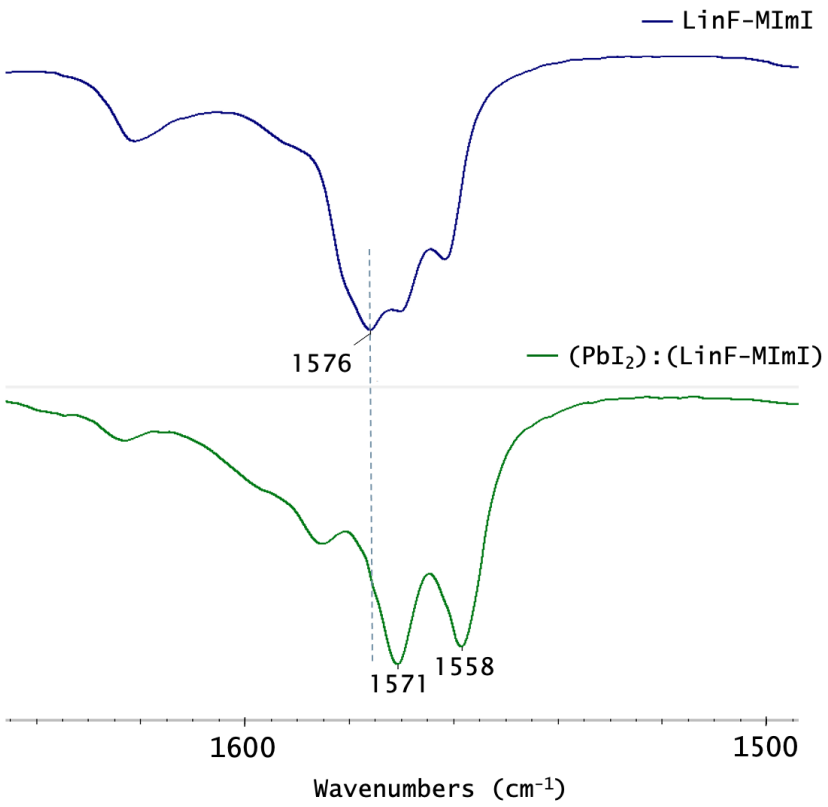

Figure 3.22: Change of imidazole ring C=C stretching peak as effect of different charge distribution induced by lead iodide.

3. **CF stretching signals**, which can be considerated as another clue of the presence of the fluorinated imidazolium cation after the reaction. Indeed, the fluorinated part creates the same signals both for the starting imidazolium salt and the final product. It has to be noticed that in this region there are no significant changes because the interactions involving the fluorinated chains do not change. It is probable that the fluorinated chains interact with each other by fluorous-fluorous interactions which remain unchanged after the interaction with lead.

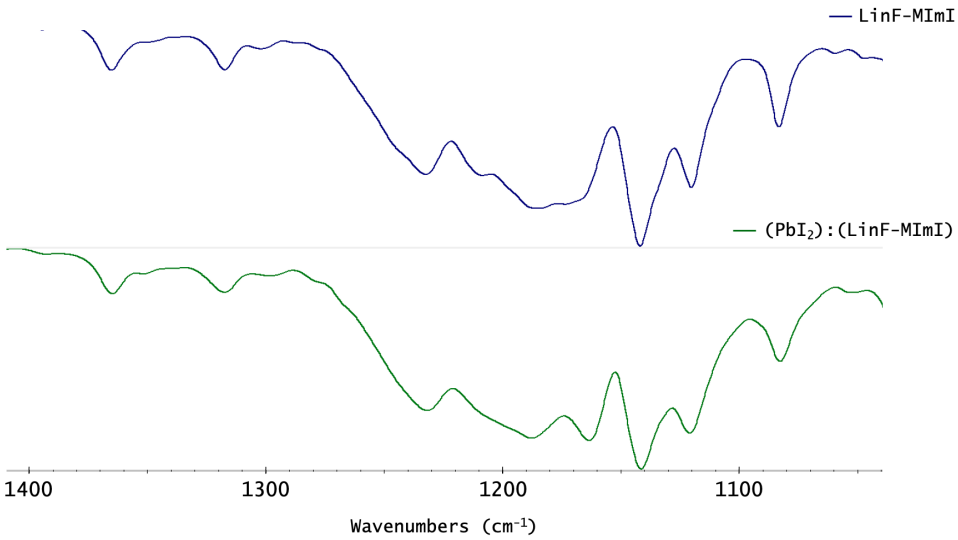

Figure 3.23: CF_2 and CF_3 stretching signal both for the LinF-MImI and the (PbI_2):(LinF-MImI) samples.

Table 3.4: Characteristic peaks of the LinF-MImI imidazolium salt and the (PbI_2):(LinF-MImI) perovskite.

	C(4)=C(5)H str	**CH_3 symmetric str**	**C=C str**	**CF_2 str**
LinF-MImI	3142	2952	1576	1236, 1184
(PbI_2):(LinF-MImI)	3137	2948	1571, 1558	1232, 1189

As conclusion, the IR spectroscopy could provide a preliminary evaluation of the interactions between the imidazolium cation and lead iodide by analyzing the three fingerprinting regions detected in the FTIR spectrum.

Nuclear Magnetic Resonance and Mass Spectroscopy

In order to make a comparison and see if it is possible to notice some differences in the NMR spectra after the interaction of the imidazolium salt with lead iodide, first of all few mg of the LinF-MImI compound were dissolved in aceton-d6. In Figure 3.18 is reported the NMR spectrum of the linear perfluoroalkyl imidazolium salt. The characteristic peaks are expected to be in the same three main regions:

1. Single H linked to carbon atoms characteristic of the imidazolium ring: a first singlet is present at 9.66 ppm. Then two singlets are present at 7.97 and 7.80 ppm. All these signals are integrated 1.
2. Singlet related to the methyl group of the imidazolium integrating 3 at 4.10 ppm and a triplet which integrates 2 related to the methylene group near the imidazolium ring at 4.68 ppm.
3. A multiplet between 2.32 and 2.54 ppm related to the other two methylene groups, integrating 4.

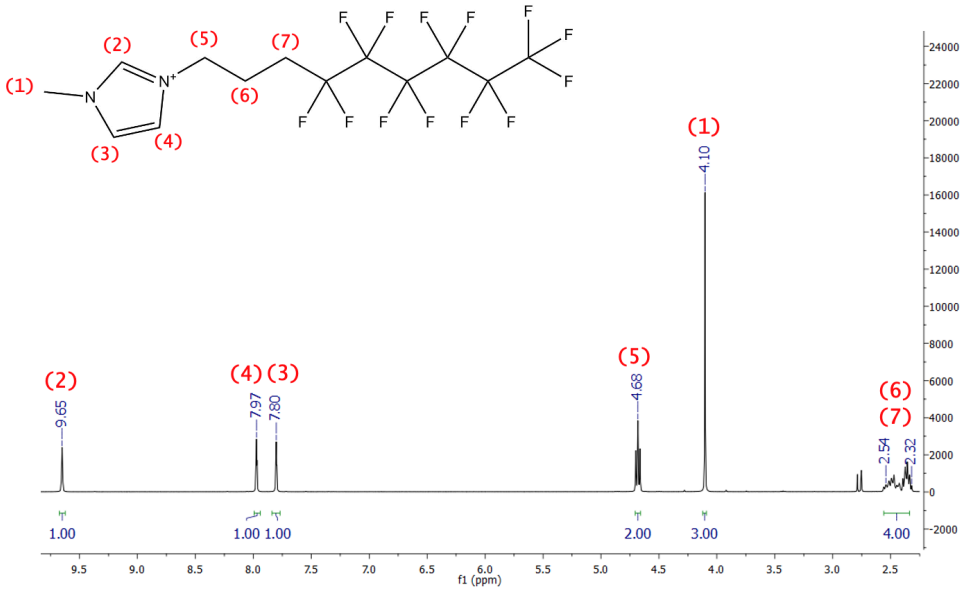

Figure 3.24: ^{1}H NMR spectrum of the (LinF-MImI) compound in aceton-d6. δ/ppm : $2.32 - 2.54(4H, m, CH_2)$, 4.10 (3H,s,-CH_3), 4.68 (2H,t,CH_2), 7.80 (1H,s,NCH), 7.97 (1H,s,NCH), 9.66 (1H,s,NCHN).

Then, few milligrams of the (PbI_2):(LinF-MImI) compound were dissolved in deuterated aceton and characterized by ^{1}H NMR and ^{19}F NMR. In Figure 3.25 it is possible to see all the distinctive ^{1}H NMR signals of the imidazolium cation in the perovskite.

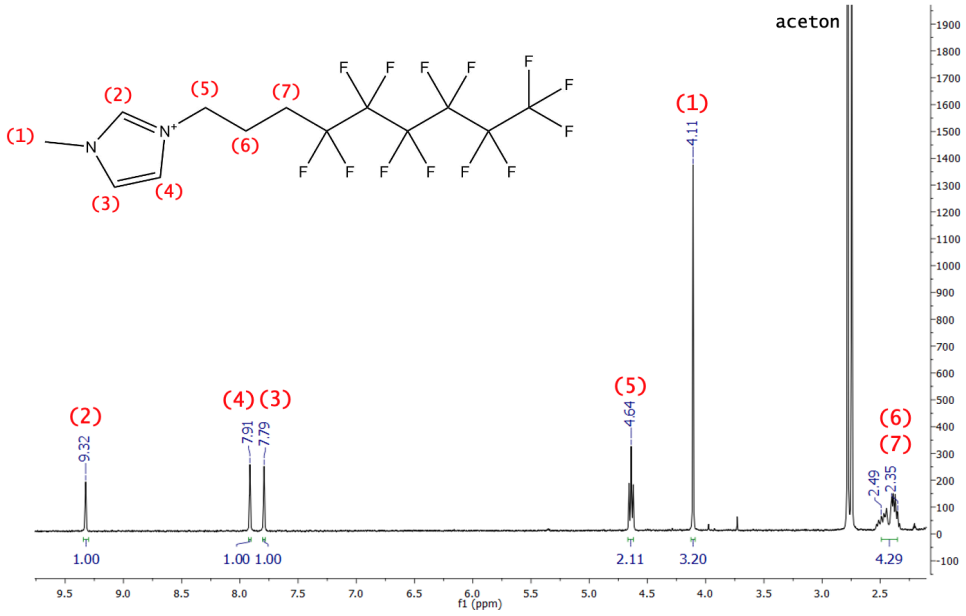

Figure 3.25: ^{1}H NMR spectrum of the (PbI_2):(LinF−MImI) compound in aceton-d6. δ/ppm : $2.35 - 2.49(4H, m, CH_2)$, 4.11 (3H,s,-CH_3), 4.64 (2H,t,CH_2), 7.79 (1H,s,NCH), 7.91 (1H,s,NCH), 9.32 (1H,s,NCHN).

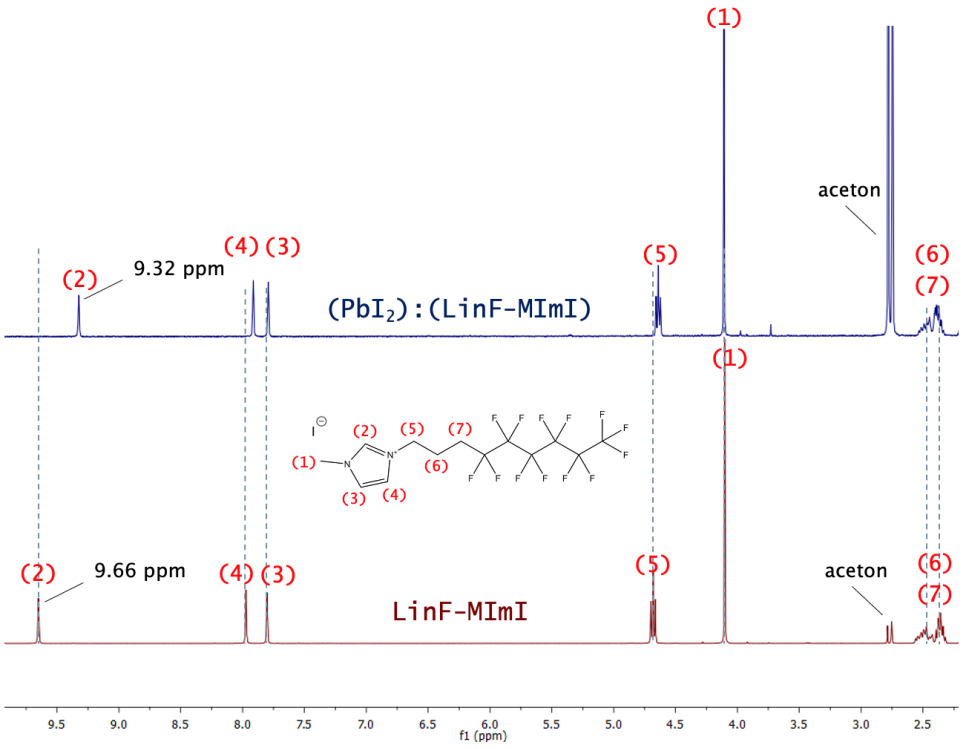

Figure 3.26: Superposition of the ^{1}H NMR spectra respectively of the (LinF-MImI) salt (bottom) and (PbI_2):(LinF-MImI) perovskite (top). A right shift to lower frequencies is shown for the single H linked to the C atom in the imidazolium ring in position 2.

The peaks are more or less in the same position both for the perovskite and the salt. Notably there are slight shifts to the right of the peaks related to the single H linked to the C atom in the imidazole ring in position 3 and 4. The single H linked to the carbon atom in position 2 in the imidazolium ring shifts more than the others to the right. This effect could be due to the fact that after the interaction with lead iodide the electron cloud density changes and is higher than before, therefore the proton is more shielded causing a right shift of the peak.

As shown in Figure 3.36, the sample was further characterized using mass spectrometry by dissolving 1 mg of the product in 1 mL of acetonitrile. Specifically, both the positive and the negative ion modes were collected. Looking at the positive ion mode spectrum there is only one peak and so it is possible to assert that the cation is present in its entirety in the final product and that the reaction with lead iodide did not produce any impurities. While in the negative ion mode some of the peaks have been assigned: the I- at 127, the (LinF-MImI)I- (theor: 696.89) at 697.1 and the (LinF-MImI)2I- (theor: 1266.87) at 1266.5. Notably the peak at m/z = 588 is related to the PbI_3^- anion which could be probably formed upon decomposition of the lead iodide clusters during the analysis. Peaks related to lead oxidation were not evident and so it was collectively concluded that the isolated crystals were of high purity.

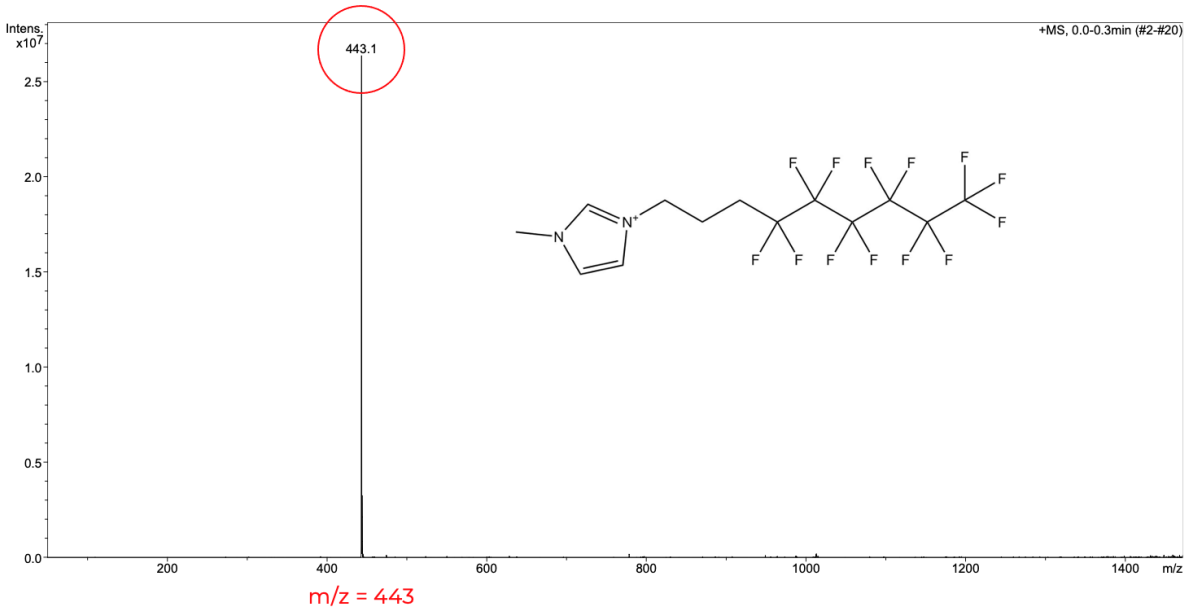

Figure 3.27: Mass spectrum of the (PbI_2):(LinF-MImI) compound in acetonitrile. Positive ion mode showing peak related to the presence of the perfluorinated linear cation (m/z=433).

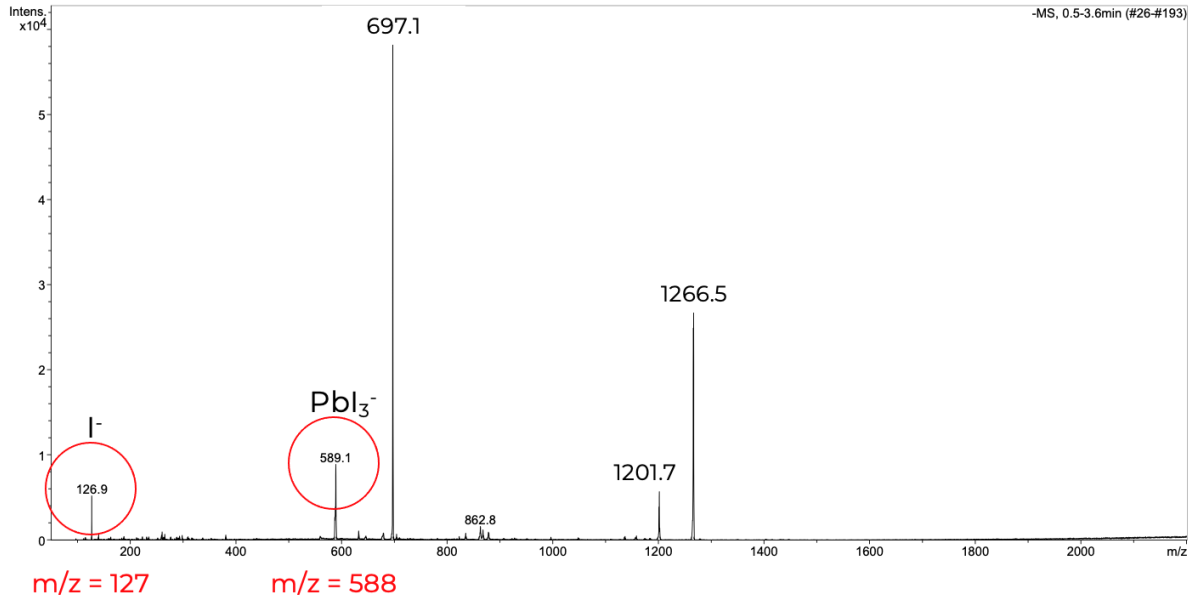

Figure 3.28: Mass spectrum of the (PbI_2):(LinF-MImI) compound in acetonitrile. Negative ion mode with peaks associated with iodine (m/z=127) and PbI_3^- anions produced upon decomposition of lead iodide clusters.

3.2.2. (PbI_2):(BrF-MImI)

First of all it has to be mentioned that when the imidazolium cation with the multi-branched fluorinated chain reacted (BrF-MImI) with lead (II) iodide, no single crystals suitable for XRD analysis were produced. Instead, a microcrystalline powder was synthesized, which has been analyzed by FTIR, NMR and MS to determine if the perovskite was obtained.

Fourier Transformed Infrared Spectroscopy (FTIR)

To have a first confirm that the reaction has been succesful, following the previous analysis made with the (PbI_2):(LinF-MImI) perovskite, the three fingerprinting regions of the perfluorinated imidazolium cation were investigated to determine how the interactions with lead iodide modify the vibrational modes. Again, a change of signals in 2800-3200 cm^{-1} region related to CH stretching modes is noticed and can be attributed to the non-covalent interactions forming between the BrF-MImI sample and the lead (II) iodide.

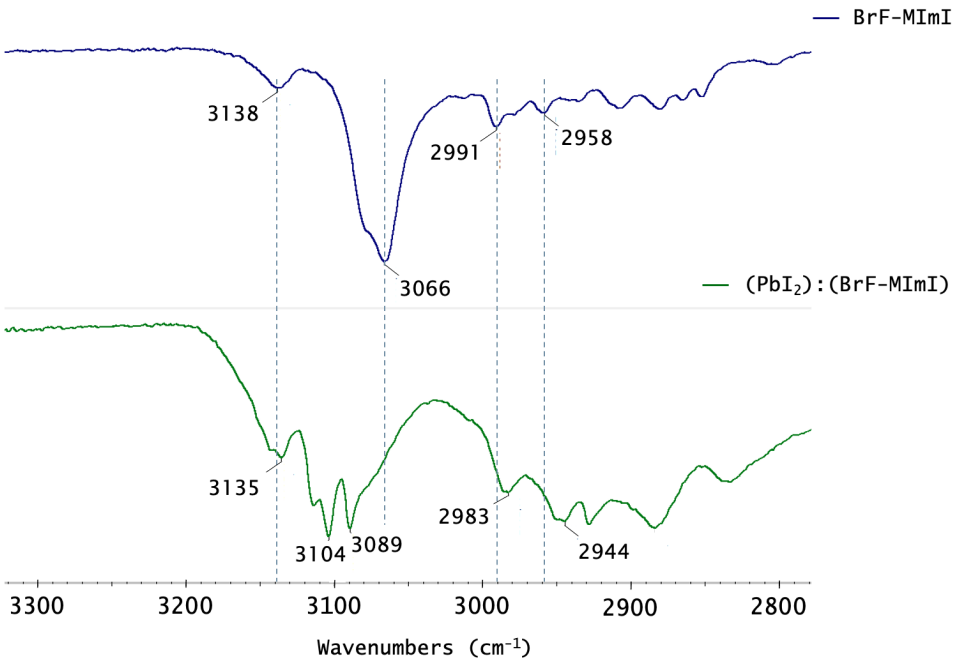

Figure 3.29: FTIR spectra comparison between BrF-MImI and (PbI_2):(BrF-MImI) in the CH stretching region.

In the same way, the change of imidazolium ring stretching in 1500-1600 cm^{-1} region was evident. A double peak is produced by interaction with lead iodide at 1570 and 1564 cm^{-1}, indicating that the electron cloud density of the imidazole ring has changed. Finally, the region related to CF stretching signals of the (PbI_2):(BrF-MImI) perovskite was equal

with the same peaks in comparison to the starting BrF-MImI salt highlighting the fact that the fluorinated part interacts with itself again through fluorous-fluorous interactions that are unaffected by the reaction with lead iodide.

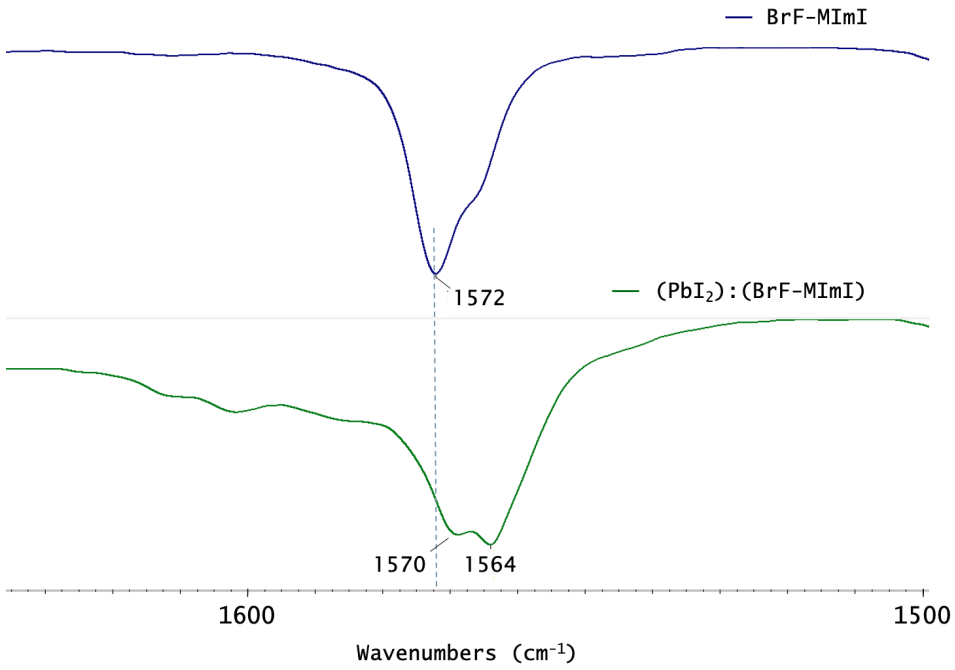

Figure 3.30: Change of imidazolium C=C stretching peak as effect of different charge distribution induced by lead iodide.

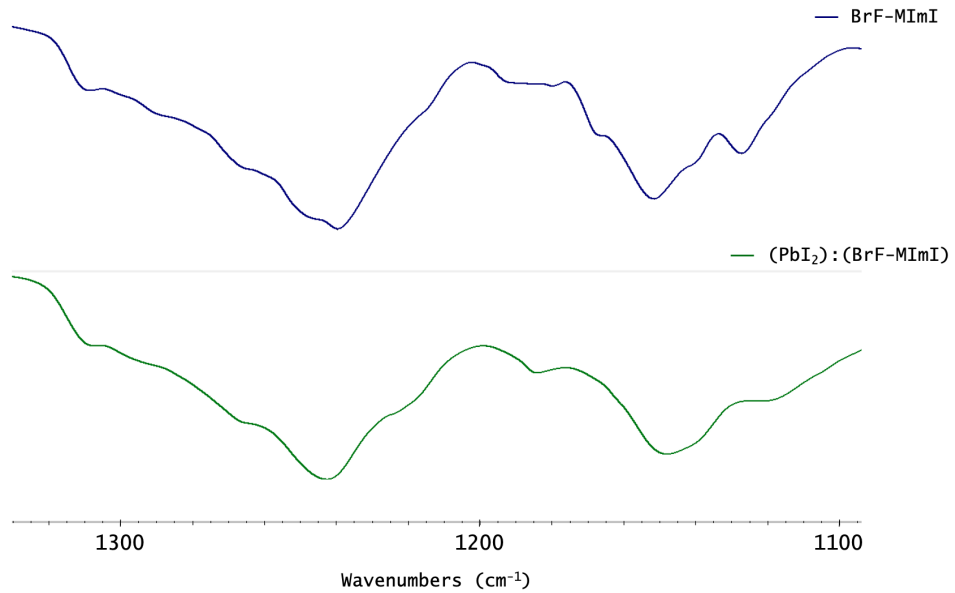

Figure 3.31: CF_2 and CF_3 stretching signal both for the BrF-MImI and the (PbI_2):(BrF-MImI) samples.

The FTIR analysis allows us to determine that a reaction between the starting reagents occurred even though the crystal structure of the final product is still unclear. In addition, the three fingerprinting regions change in the same manner as with the linear imidazolium salt following the reaction, indicating that these changes are reproducible and can be used to evaluate in general interactions between various fluorinated imidazolium salts and lead iodide. In light of the obtained results, comparing the thermal behavior of the (PbI_2):(BrF-MImI) with the well-known (PbI_2):(LinF-MImI) perovskite became of primary interest to better understand the effect of the multibranched fluorinated cation on the chemical structure of the final product.

Nuclear Magnetic Resonance and Mass Spectroscopy

As in the previous case, in order to make a comparison and see if it is possible to notice some differences in the NMR spectra after the interaction of the imidazolium salt with lead (II) iodide, few mg of the BrF-MImI compound were dissolved in aceton-d6.

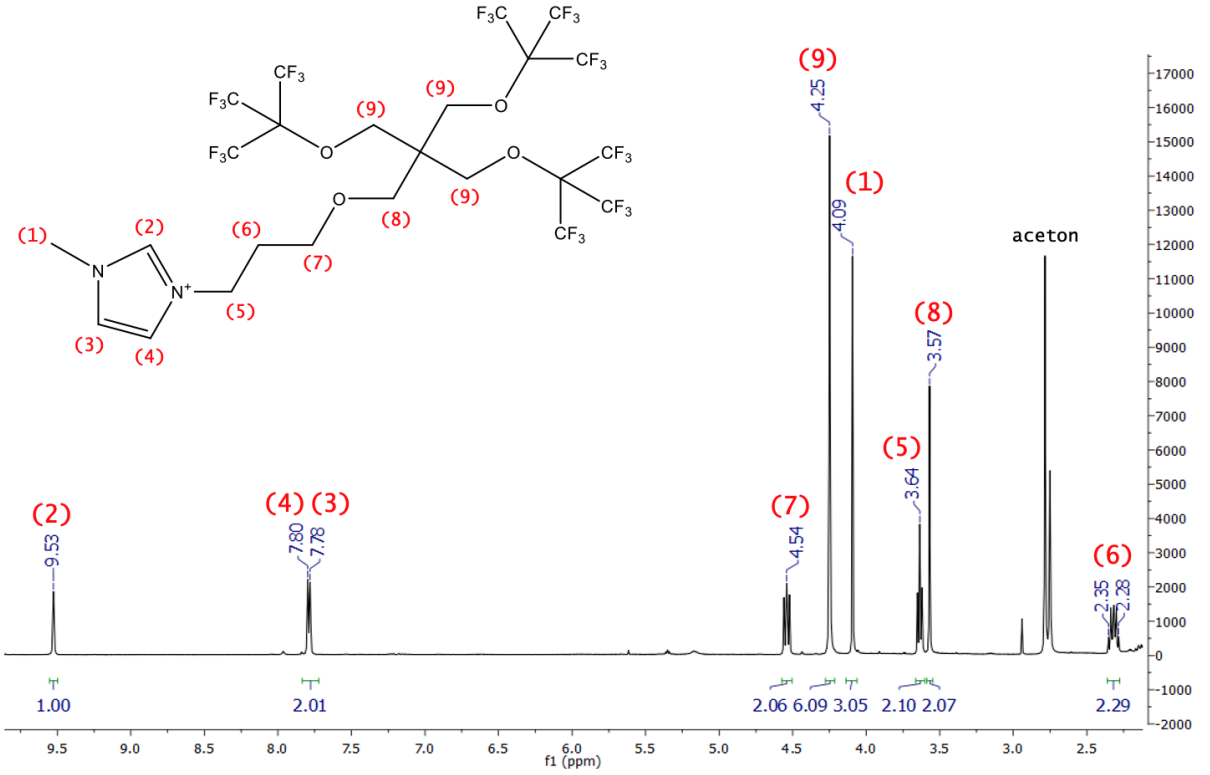

Figure 3.32: ^{1}H NMR spectrum of the BrF-MImI compound in aceton−d6. δ/ppm : 2.28−2.35($2H, m, CH_2$), 3.57 (2H,s,CH_2), 3.64 (2H,t,CH_2), 4.09 (3H,s,-CH_3), 4.25 (6H,s,CH_3), 4.54 (2H,t,CH_2), 7.78 (1H,s,NCH), 7.80 (1H,s,NCH), 9.53 (1H,s,NCHN).

Then, to rule out the presence of impurities, a few milligrams of the final product were dissolved in deuterated aceton and characterized by ^{1}H NMR and ^{19}F NMR. From the ^{1}H NMR is possible to see all the distinctive signals of the branched cation (Figure 3.33) while from the ^{19}F NMR only one peak is present, related to the branched fluorinated part of the cation (Figure 3.34).

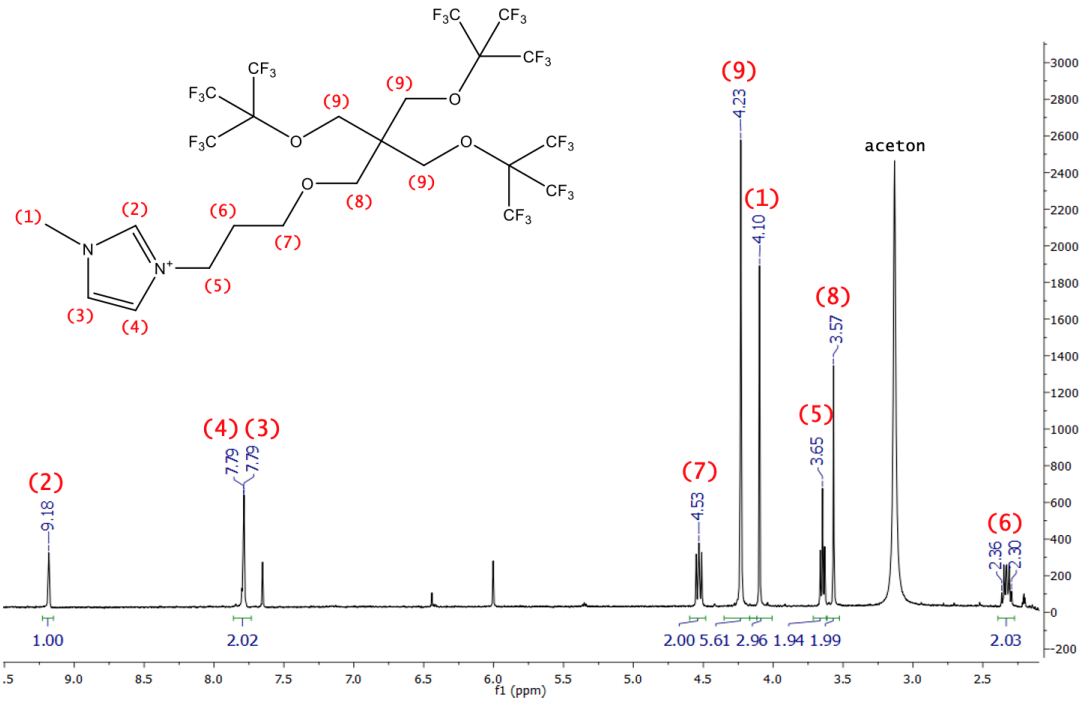

Figure 3.33: ^{1}H NMR spectrum of the (PbI_2):(BrF-MImI) compound in aceton−d6. δ/ppm : $2.30 - 2.36(2H, m, CH_2)$, 3.57 (2H,s,CH_2), 3.65 (2H,t,CH_2), 4.10 (3H,s,-CH_3), 4.23 (6H,s,CH_3), 4.53 (2H,t,CH_2), 7.79 (1H,s,NCH), 7.79 (1H,s,NCH), 9.18 (1H,s,NCHN).

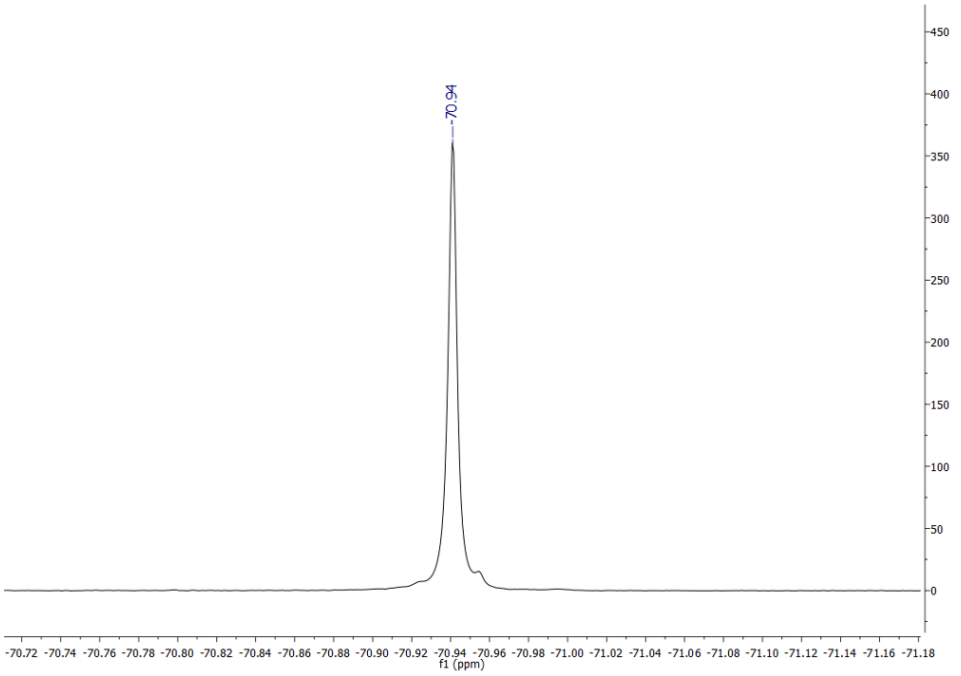

Figure 3.34: ^{19}F NMR spectrum of the (PbI_2):(BrF-MImI) compound in aceton−d6. δ/ppm : $70.94(27F, s)$.

The signal related to the single H bonded to the carbon atom in position 2 of the imidazolium ring exhibits a shift to the right in this case as well. This is additional evidence that the reaction with lead iodide was successful.

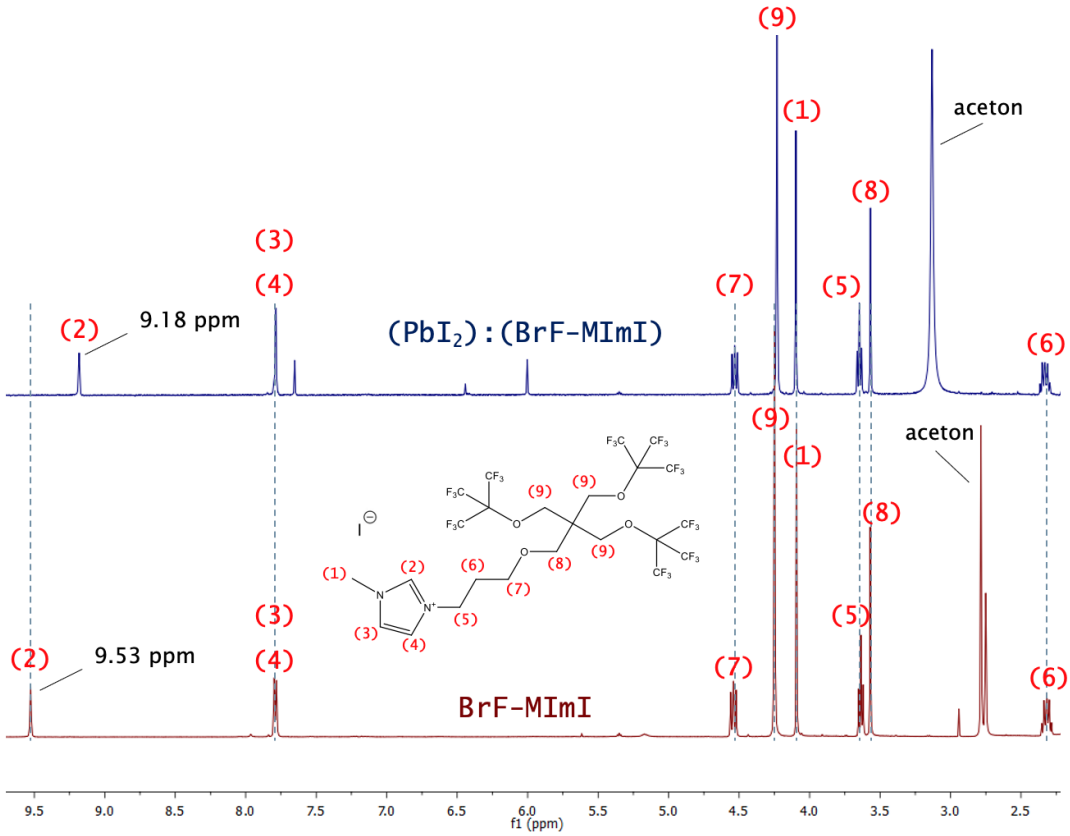

Figure 3.35: Superposition of the ^{1}H NMR spectra respectively of the (BrF-MImI) salt (bottom) and (PbI_2):(BrF-MImI) perovskite (top). A right shift to lower frequencies is shown for the single H linked to the C atom in the imidazolium ring in position 2.

As shown in Figure 3.36 and Figure 3.37, the sample was further characterized using mass spectrometry by dissolving 1 mg of the product in 1 mL of aceton. Also in this case it is feasible to state that the branched cation is present in its entirety in the final product and that there are no impurities resulting from the reaction with lead iodide. We can hypothesize the formation of inorganic octahedra after the reaction due to the presence of the PbI_3^- anion peak, which was also present in the other case, and which is likely formed after the disaggregation of the octahedra during the analysis.

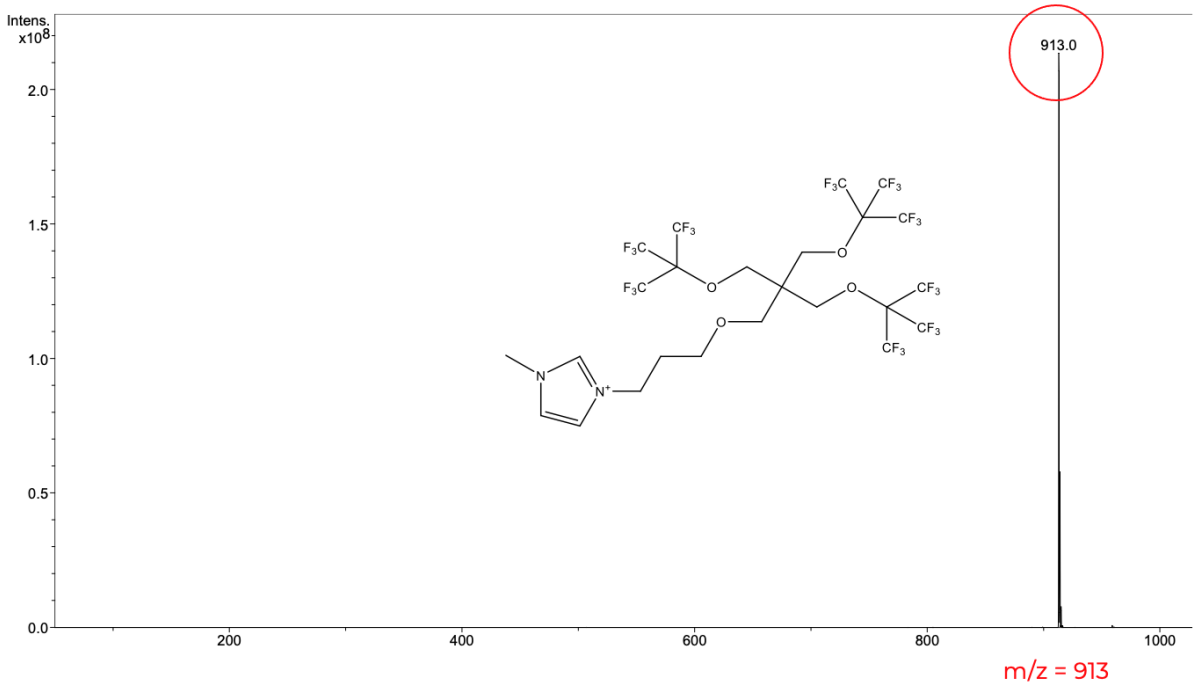

Figure 3.36: Mass spectrum of the (PbI_2):(BrF-MImI) compound in aceton. Positive ion mode showing peak related to the presence of the perfluorinated cation (m/z=913.3).

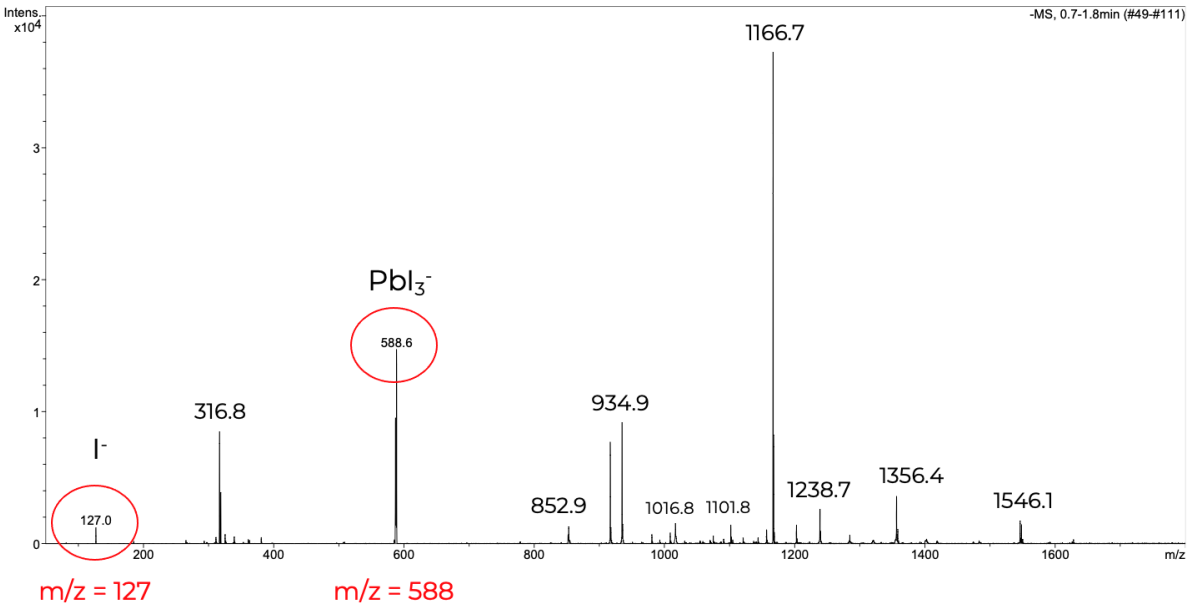

Figure 3.37: Mass spectrum of the (PbI_2):(BrF-MImI) compound in aceton. Negative ion mode with peaks associated with iodine (m/z=127) and PbI_3^- anions produced upon decomposition of inorganic octahedra.

X-ray diffraction (XRD) analysis

As previously mentioned, in this case the X-ray analysis at the synchrotron has not been done yet, due to the low quality of the obtained crystals, the single crystal structure could not be completely resolved. However, Powder X-Ray Diffraction (PXRD) spectra were collected as it is possible to see in Figure 3.38.

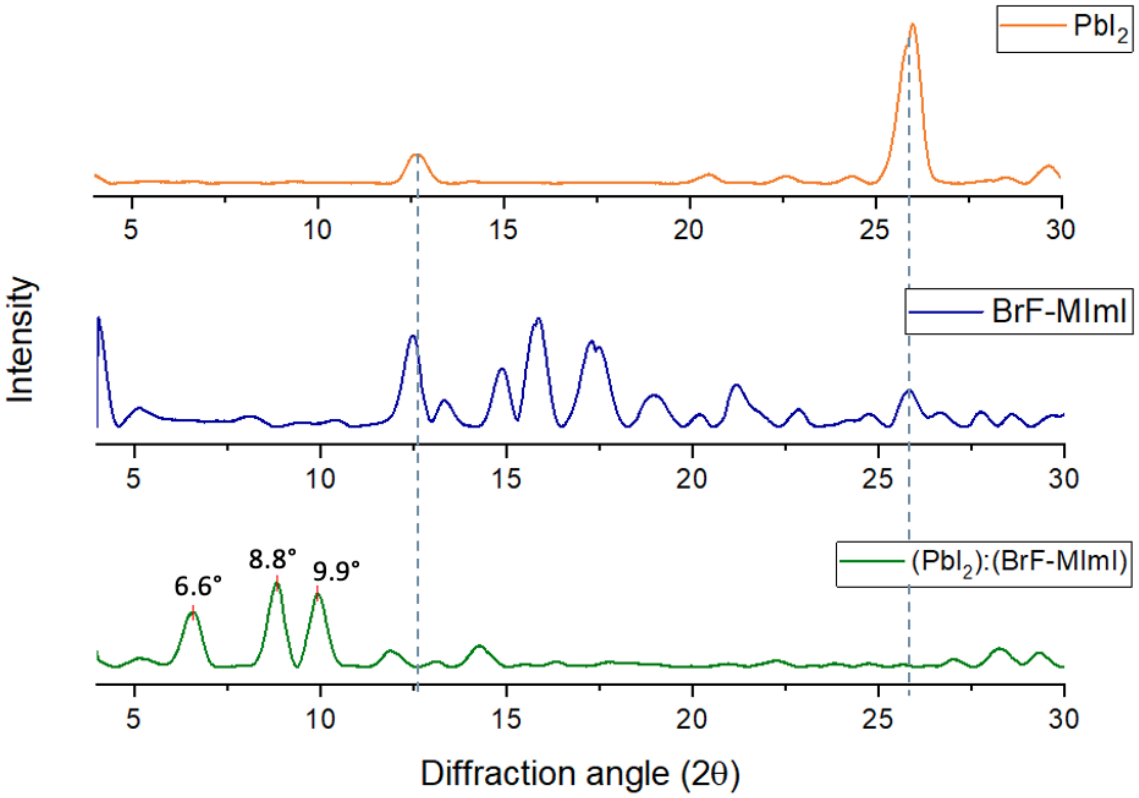

Figure 3.38: Powder XRD spectra comparison among lead (II) iodide, $C_{20}H_{14}F_{27}MetImI^{-}$ and the $(C_{20}H_{14}F_{27}MetImI^{-})$:$(PbI_2)$[2:1] perovskite.

First of all, it must be noted that this compound does not exhibit superimposable peaks with reagent signals. These results suggest that the (PbI_2):(BrF-MImI) perovskite should have a distinct lead iodide lattice and it can be considered as a further clue indicating that the reaction was successful. As reported in Figure 3.39, a comparison between the PXRD spectra of the two perovskites obtained has been done.

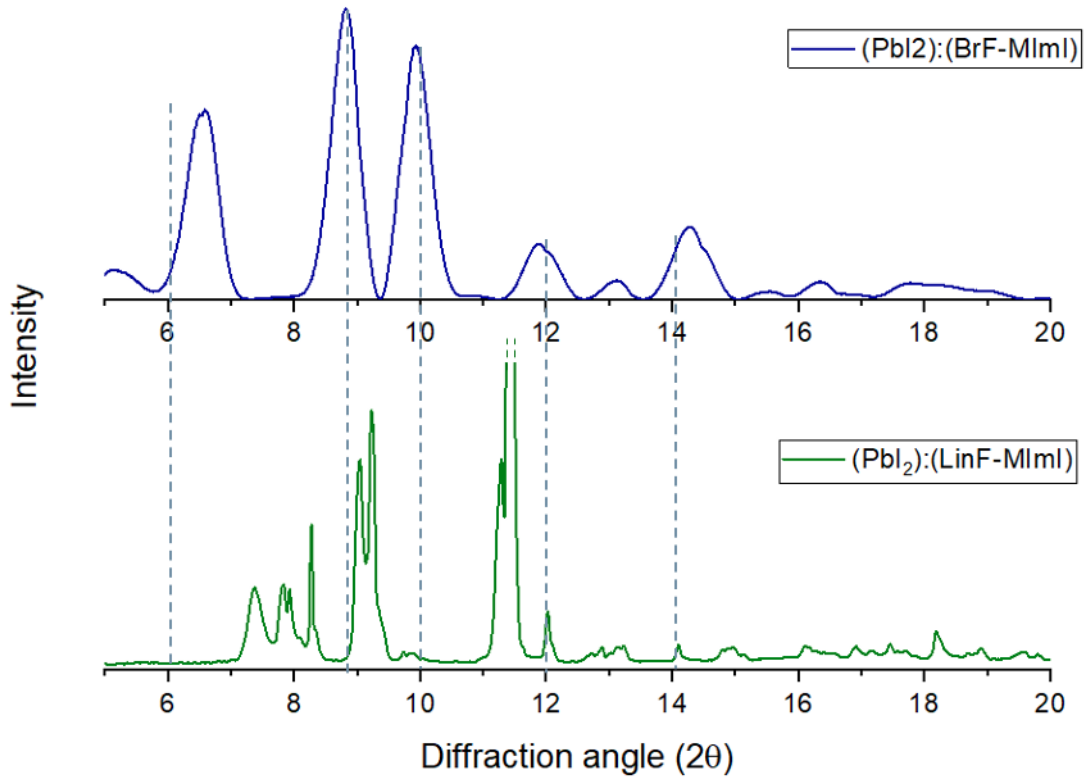

Figure 3.39: Comparison between the PXRD spectra obtained for the (PbI_2):(LinF−MImI) and the (PbI_2):(BrF-MImI) samples.

Without knowing the crystalline structure of the (PbI_2):(BrF-MImI) sample, the peaks can not be associated with a particular crystallographic plane and furthermore there is not a similar pattern with respect to the (PbI_2):(LinF−MImI) perovskite that can assure the formation of the $Pb_3I_{12}{}^{-6}$ trinuclear inorganic cluster also in this case. However, it is possible to notice that with respect to the BrF-MImI spectrum the peaks of the (PbI_2):(BrF-MImI) are relocated to lower angles. Given the fact that higher distances among planes need lower angles for scattering we can deduce that the interplanar spacing of the crystals in the perovskite layers is greater than in the imidazolium salt due to the formation of inorganic octahedra. The peaks obtained are located at different values of 2θ with respect the (PbI_2):(LinF-MImI) perovskite because with the addition of a multibranched pefluorinated cation (shown in Figure 3.40) leads to a different segregation of the fluorinated portion induced by a different self-assembly effect and steric hindrance of the fluorinated part.

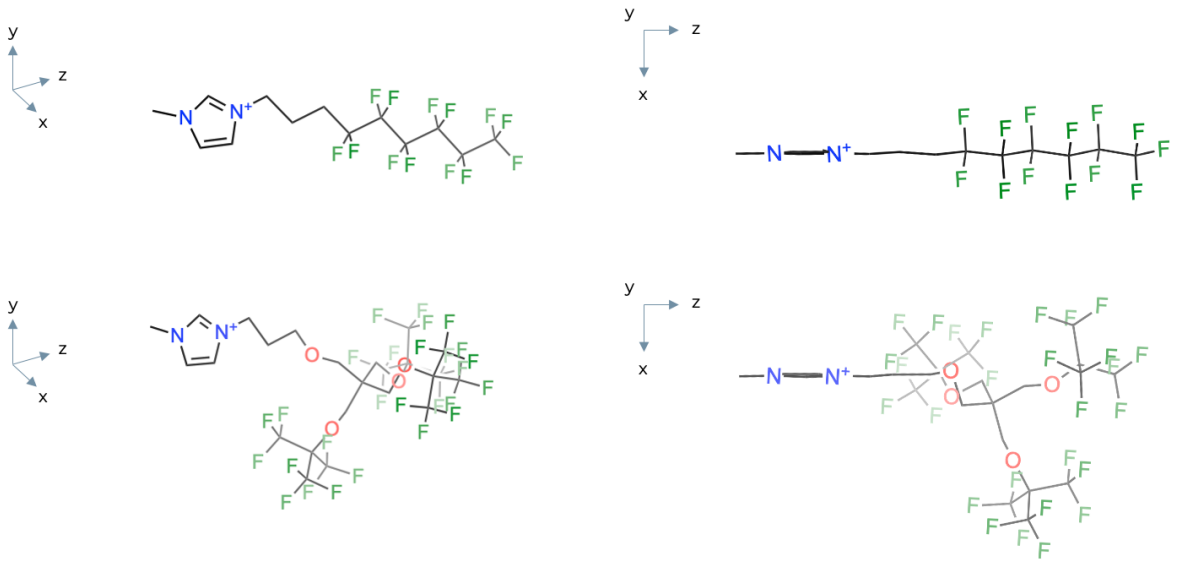

Figure 3.40: Comparison between the 3D images of the multibranched fluorinated and the linear perfluoroalkyl fluorinated imidazolium cations, modelled with the professional software ChemDraw®.

As a conclusion, just by looking the PXRD spectra it is not possible to hypothesize the formation of the quasi-0D perovskite also in this case and the structural characterization of this compound has to be completed, but in both cases ((PbI_2):(BrF-MImI) and (PbI_2):(LinF−MImI)) we can notice a general trend which is the formation of intense peaks in the region between 6° and 12° after the reaction of the imidazolium salt with lead iodide. Together with the data previously obtained from the FTIR, NMR and MS, this permits us to deduce that the perovskite is formed and the reaction was successful also in this case.

3.2.3. (PbI_2):$(BrF\text{-}NH_2)$

X-ray diffraction (XRD) analysis

Also for this compound the Powder X-Ray Diffraction (PXRD) spectra were collected. As shown in Figure 3.41 the peaks of the multibranched fluorinated ammonium salt and of the lead (II) iodide used as regents are both present with different intensities in the final product spectrum. From this analysis the powder obtained seems to be a mixture of both compounds that did not react.

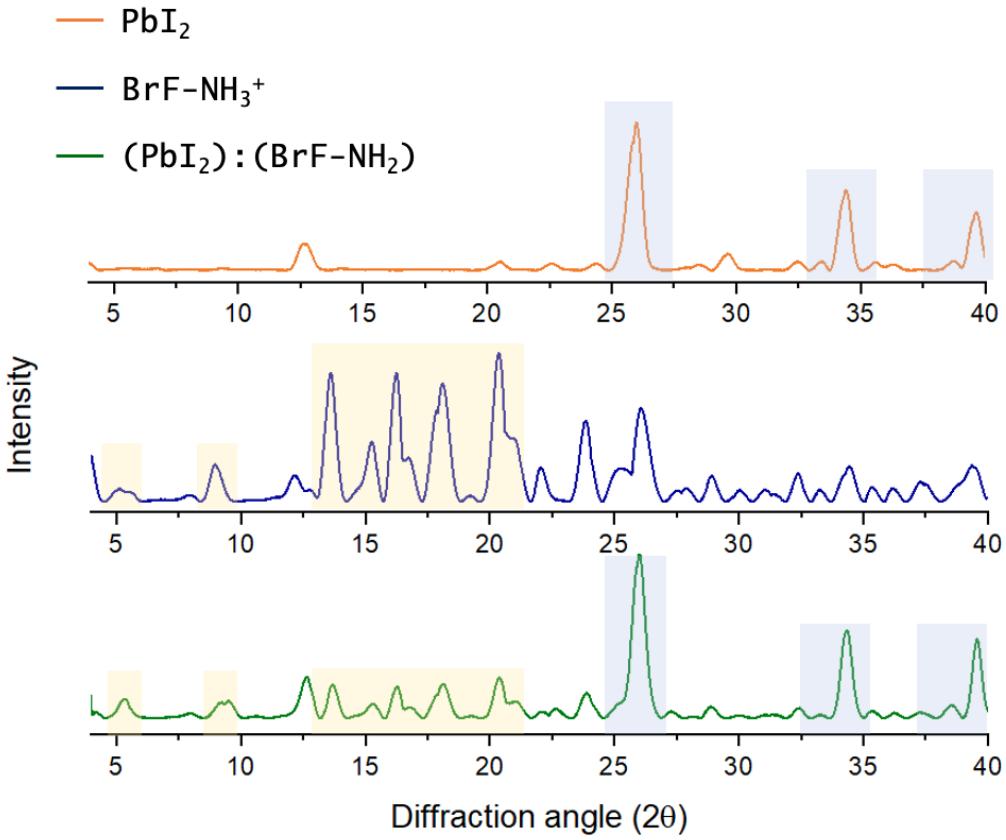

Figure 3.41: Powder XRD spectra comparison among the lead (II) iodide, the ammonium salt Perfecta derivative and the (PbI_2):$(BrF\text{-}NH_2)$ perovskite.

One hypothesis for the failed reaction is that the ammonium group is less exposed to the formation of an interaction with the inorganic lattice. It should also be noted that the insoluble nature of the ammonium salt in hydroiodic acid did not facilitate the reaction. In the future, another solvent, such as the γ-valerolactone reported in the literature [101] as a solvent used for spin coating of perovskites, may be attempted to dissolve the branched amine with the lead (II) iodide directly and favour the reaction.

3.3. Thermogravimetric analysis (TGA)

Temperature-dependent stability of perovskites has been investigated through TGA under nitrogen atmosphere to understand their degradation temperature. Before examining the experimental results, the TGA of lead (II) iodide has been examinated as initial step to understand how residual PbI_2 decomposition affects weight loss in thermogravimetric analysis. With the aim of analyzing the perovskites so that they are well-performing without losing their properties due to thermal degradation, it is reasonable to consider as T_{deg} (onset of degradation) a temperature which corresponds to a mass loss of 5% for the sample. As depicted in Figure 3.42, from TGA analysis performed, the T_{deg} of PbI_2 was found approximately at 488°C, which is coherent with literature data [102].

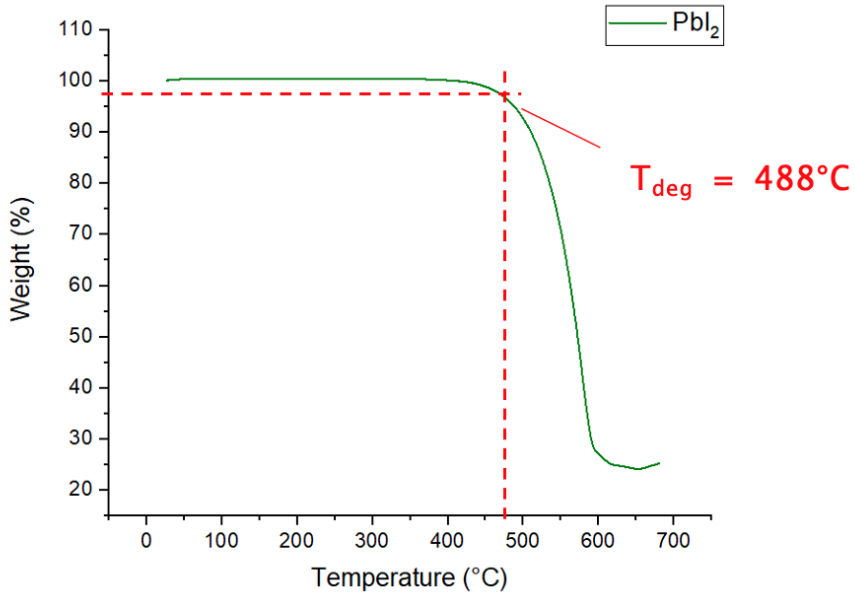

Figure 3.42: Onset of degradation (T_{deg}) of lead (II) iodide.

3.3.1. (PbI_2):(LinF-MImI)

In order to analyse the thermal degradation behavior of the (PbI_2):(LinF-MImI) perovskite, a TGA analysis of the linear imidazolium salt (LinF-MImI) was performed first. As it is possible to see in Figure 3.43 the LinF-MImI sample shows a degradation onset at 246°C. Regarding the (PbI_2):(LinF-MImI) perovskite synthesized in this work, TGA plot shows two steps of degradation, as reported in Figure 3.43 that can be associated with the two degradation steps typical of organo-metal halide perovskites. The first one is at 266°C which is related to the organic imidazolium cation followed by PbI_2 sublimation at temperatures higher than 400°C. Notably, due to the reaction with lead iodide and the formation

of inorganic clusters the onset of degradation related to the imidazolium cation shifts to higher temperatures. This result is compatible to what is reported in literature. Indeed, as reported in literature by Yu, Shan-Shan, et al. [69] for alkyl-methyl-imidazolium lead bromide perovskites, the general processes of thermal degradation occurs in two steps: organic cations degradation followed by PbI_2 sublimation at higher temperatures with total mass loss.

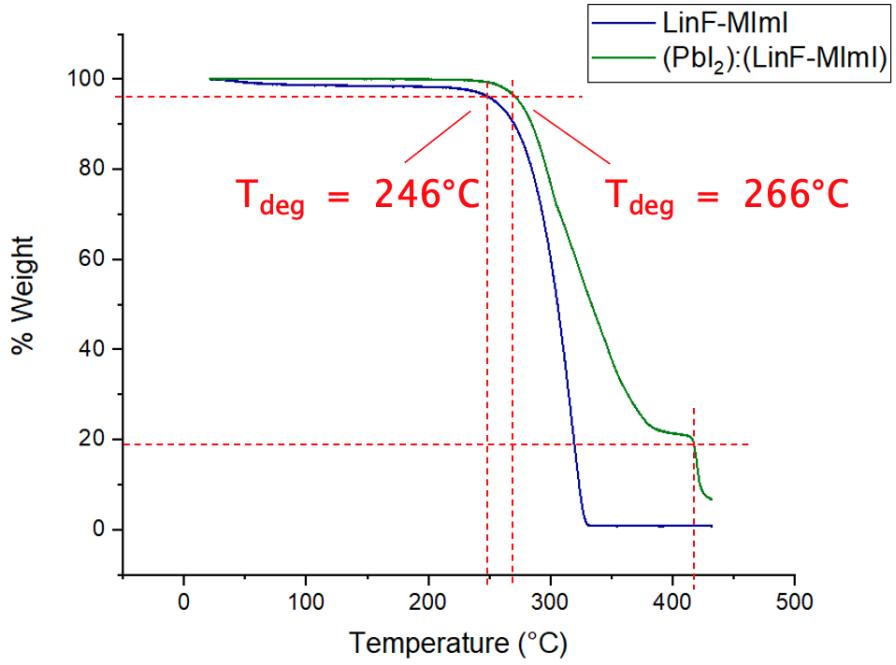

Figure 3.43: Degradation onset of the imidazolium salt (LinF-MImI) at 246°C and of the (PbI_2):(LinF-MImI) perovskite at 266°C.

In light of these results, it has to be noticed that an important feature of this perovskite is its high stability to open air at room temperature.

3.3.2. (PbI_2):(BrF-MetImI)

In the same way, the thermal stability of the (PbI_2):(BrF-MetImI) perovskite was evaluated and compared to the TGA plot of the branched imidazolium salt (BrF-MetImI). As it is possible to see in Figure 3.44, the BrF-MetImI sample shows a degradation onset at 228°C. The (PbI_2):(BrF-MetImI) perovskite TGA plot shows two-step weight loss in the range of 25°C-500°C respectively at 270°C and around 440°C (Figure 3.44) that can be again associated with the organic cation degradation followed by the PbI_2 sublimation. As in the previous instance, the presence of lead causes the shift of the T_{deg} value to higher temperatures with respect to the initial imidazolium salt (Table 3.5).

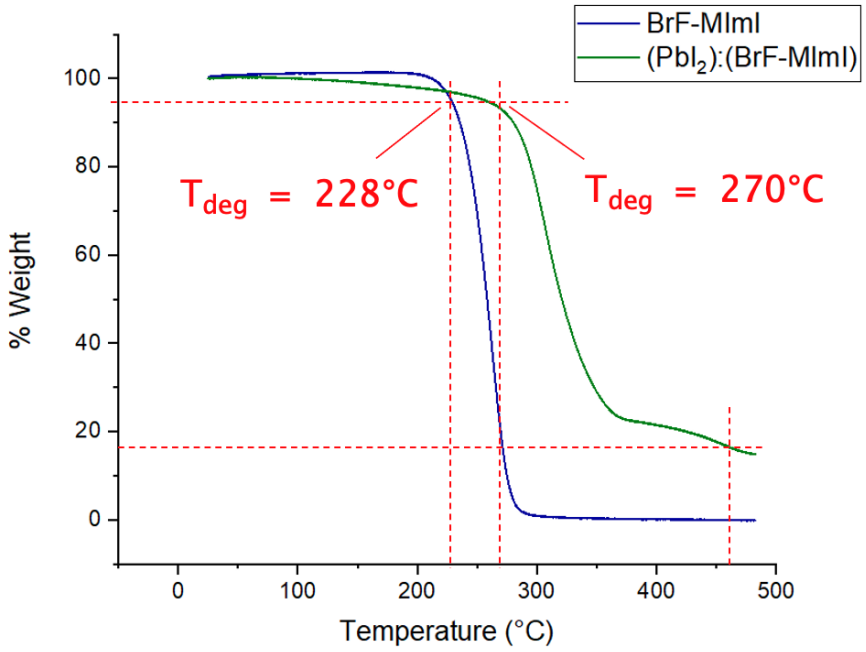

Figure 3.44: Degradation onset of the branched imidazolium salt (BrF-MetImI) at 228°C and of the (PbI_2):(BrF-MetImI) perovskite at 270°C.

Table 3.5: Onset degradation temperatures for the LinF-MImI, BrF-MetImI salts and the (PbI_2):(LinF-MImI), (PbI_2):(BrF-MetImI) perovskites.

	Onset of degradation [°C]
LinF-MImI	246
BrF-MetImI	228
(PbI_2):(LinF-MImI)	266
(PbI_2):(BrF-MetImI)	270

3.4. Differential Scanning Calorimetry (DSC)

Differential Scanning Calorimetry together with Polarized-light Optical Microscope (POM) images have been studied to evaluate phase transitions in perovskites. As a result of the distinct space reorganization of lead halide lattice, these phase transitions were reported as discontinuities (exothermic or endothermic peaks) in DSC thermograms. It is known that the initial perfluoroalkyl imidazolium salt is LC with a smectic phase due to fluorine-fluorine interactions, which are responsible for the segregation of the fluorinated chains [88]. As mentioned previously, the examined X-Ray structure of the (PbI_2):(LinF-MImI) perovskite reveals the presence of a lamellar structure in the solid state (Figure 3.10), and if this lamellar structure were to be maintained in the molten state, this would probably imply a liquid-crystalline behavior also in the perovskite.
Starting from these informations and the obtained TGA results, being aware of the onset of degradation of all the examined materials, the thermal characterization of the samples was initiated with the hot-stage POM, which allows us to observe the phase changes and determine if there is an LC phase. In addition, a comparison was made between the DSC thermograms of the initial imidazolium salt and the related perovskite in order to confirm the POM observations and better evaluate the effect of the fluorinated cations. Notably, all complexes obtained exhibited thermotropic LC (liquid crystalline) properties. Temperatures of transition are listed in Table 3.6 and Table 3.7. All of these compounds displayed enantiotropic mesomorphism, with smectic A phases (SmA) exhibiting distinctive optical textures detectable at POM.

3.4.1. (PbI_2):(LinF-MImI)

First of all, the LinF-MImI ionic liquid was analyzed at the POM and, as it is possible to notice in Figure 3.45, during heating it undergoes a Cr-to-LC transition around 86°C with a clearing point (LC-to-Iso) at 202°C. The Cr-to-LC transition is observed thanks to the birefringence typical of liquid crystal that rotate polarized light. Therefore, with two polarized inclined by 90° light can be detected passing through liquid crystal resulting in characteristic optical texture of the smectic A phase. Notably, during cooling the Iso-to-LC transition is reproducible at the same temperature while reaching room temperature no LC-to-Cr was observed below what should be the crystallization point. The samples actually becomes solid, but it maintains the organization of the smectic A phase.

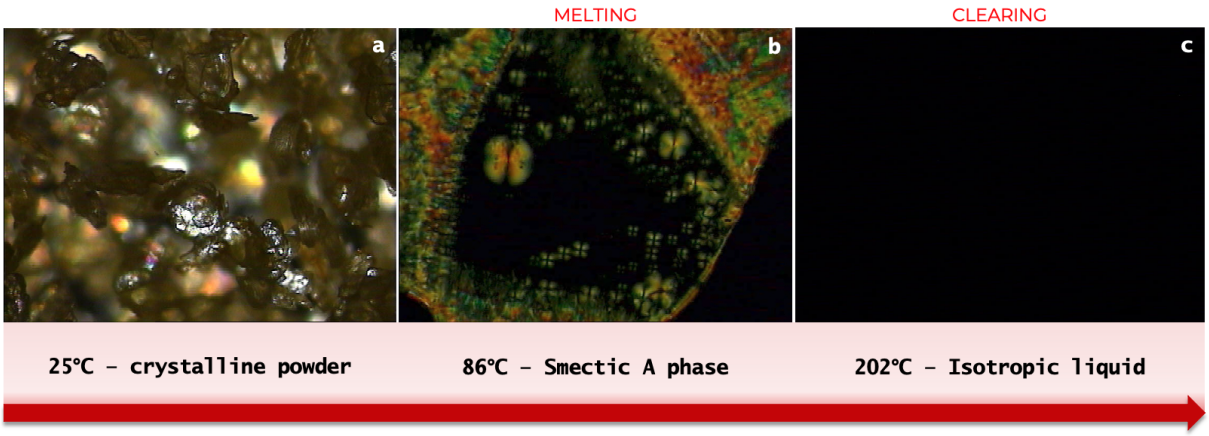

Figure 3.45: POM images of the LinF-MImI salt with T ranging from 25°C to 210°C, heating (a, b, c) with an heating rate of 10°C/min.

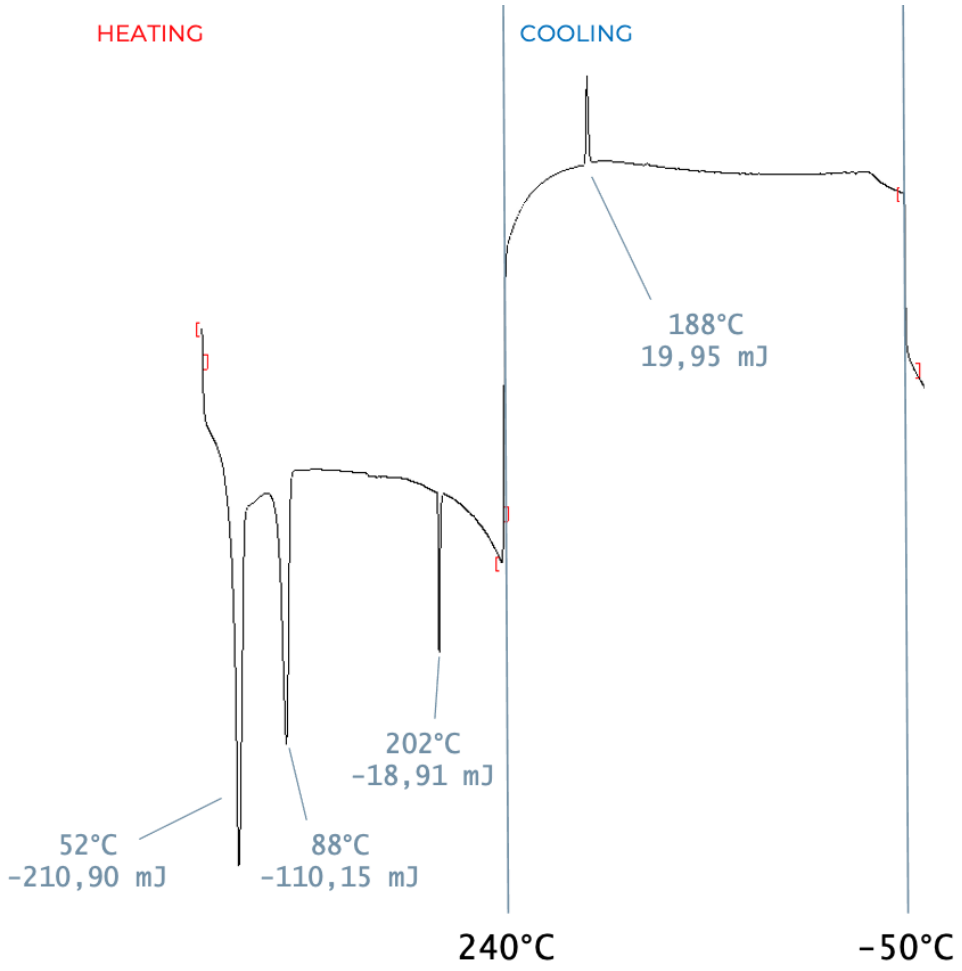

Figure 3.46: DSC results of the LinF-MImI ioniuc liquid with an heating rate of 10°C/min.

These results were confirmed with the DSC analysis where the LinF-MImI sample exhibits

three endothermic peaks, while during cooling only a single peak was detected (Figure 3.46). This single peak (at 188°C) is related to the Iso-to-LC transition. During heating the formation of the smectic phase A (SmA), made from the packing of perfluoroalkyl chains [56], is confirmed by the the endothermic peaks at 88°C while the peak at 202°C refers to the LC-to-Iso transition. The endothermic peak at 52°C probably is related to a solid-solid phase transition since it is visible only in the first heating of the sample and it is not reproducible as the others.

In the same way the (PbI_2):(LinF-MImI) perovskite has been analyzed with a hot stage POM in a range between 25°C and 250°C to study effect at high temperature avoiding the degradation of the sample (Figure 3.48). As visible from POM images in Figure 3.47, this perovskite undergoes to an initial melting transition (around 134°C in Figure 3.47b) to pass to a liquid crystalline smectic phase A. This phase remains stable until it melts as isotropic liquid around 240°C (Figure 3.47c). Then liquid crystalline behavior has been proven also during cooling phase. The isotropic liquid passed to SmA phase at 238°C, visible in Figure 3.47d. Interestingly, cooling the sample from the isotropic state to room temperature, the texture typical of the SmA phase remained unmodifed suggesting that the perovskite tends to form a glassy mesophase.

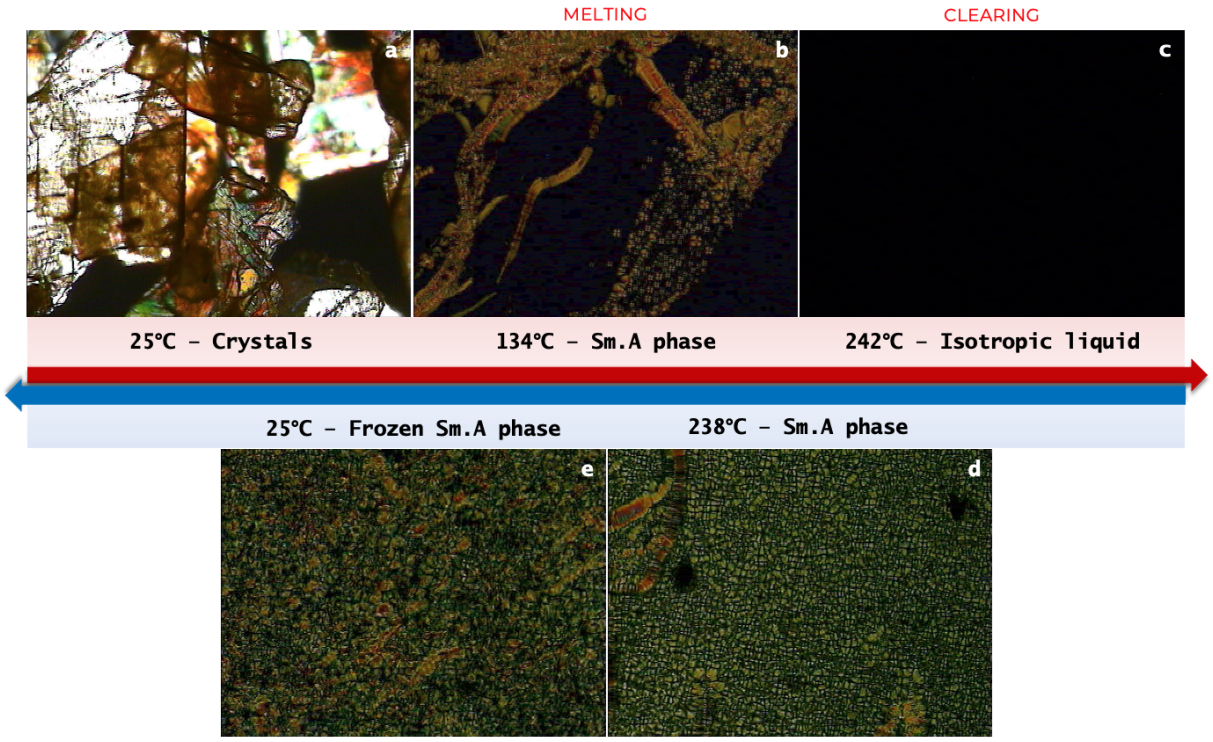

Figure 3.47: POM images of the (PbI_2):(LinF-MImI) perovskite with T ranging from 25°C to 250°C, heating (a, b, c) and cooling (d, e) with an heating rate of 10°C/min.

Afterwards, the behavior of this material was further investigated with a DSC analysis. The result obtained again confirmed what was previously noticed with the POM (Figure 3.48). The sample shows enantiotropic LC phase transitions and mesomorphism characterized, during heating, by a Cr-to-LC transition around 134°C and a clearing point at $\simeq$ 242°C. Values for the transitions exhibited by the imidazolium salt are translated to higher temperatures for the perovskite (Table 3.6). On cooling the sample to -50°C and an exothermic peak which could be associated to the crystallization of the sample was found at 6°C

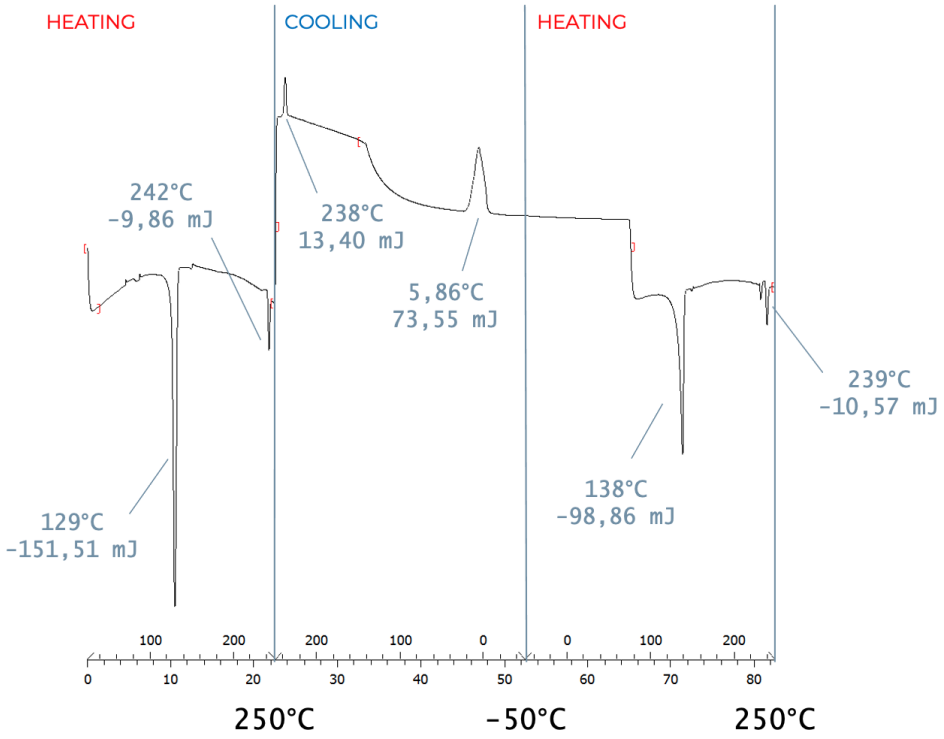

Figure 3.48: DSC results of the $(Pb_3I_{12})^{-6}(C_9F_{13}MIm)^6$ perovskite with an heating rate of 10°C/min.

Table 3.6: Phase transition temperatures and mesophase temperature ranges measured by heating and cooling the samples. Crystal phase (Cr), smectic A phase (SmA) and isotropic phase (Iso).

	Cr−SmA	**SmA−Iso**	**ΔT**
LinF-MImI	88°C	202°C	114°C
(PbI_2):(LinF-MImI)	134°C	240°C	106°C

Thus, the results obtained confirm that this perovskite could exploit fluorophobic effect given by the imidazolium cation. They organize themselves to create a lamellar structure that is mainteined also in the molten state forming a smectic-A liquid crystalline phase in which the fluorinated portion of the cations tend to segregate as depicted in Figure 3.49. So, The formation of F···F interactions of the fluorinated tails plays a key role in the assembly and stabilization of the observed SmA phases [56].

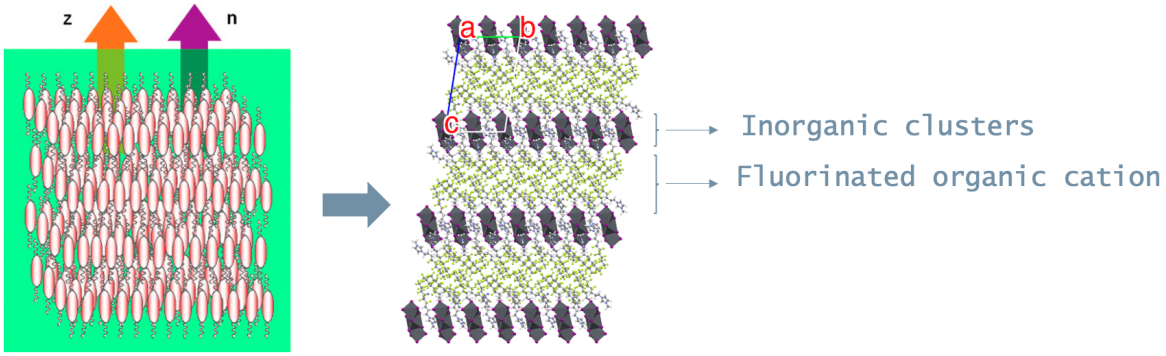

Figure 3.49: Schematic representation of a smectic-A liquid crystalline phase [103], being n the direction of the molecules and z the layer normal. In the smectic-A phase, molecules are almost perfectly parallel to each other, and the layer normal. Within a smectic layer, they have no positional or bond-orientational order. Picture made with the crystallographic software Mercury.

For the first time, thermotropic liquid crystalline behavior in low-dimensional perovskite was observed. So this is a relevant result because it provides a new insight about low-dimensional perovskites properties and possibilities. Despite the high clearing points, DSC analyses confirmed the stability of the perovskite (Figure 3.48). Repeated heating and cooling cycles demonstrated that the LC properties were fully reversible at least for three cycles and typical POM features were perfectly reproducible even after several excursions into the isotropic phases.

3.4.2. (PbI_2):(BrF-MetImI)

Also in this case the liquid crystal properties were characterized using a combination of Differential Scanning Calorimetry (DSC) and Polarized-light Optical Microscope (POM). As the linear imidazolium salt LinF-MetImI previously characterized, the BrF-MetImI sample turned out to be an ionic liquid with a melting point below 100°C. Specifically, as it is possible to notice in Figure 3.50, also the BrF-MetImI salt exhibits liquid crystalline behaviour.

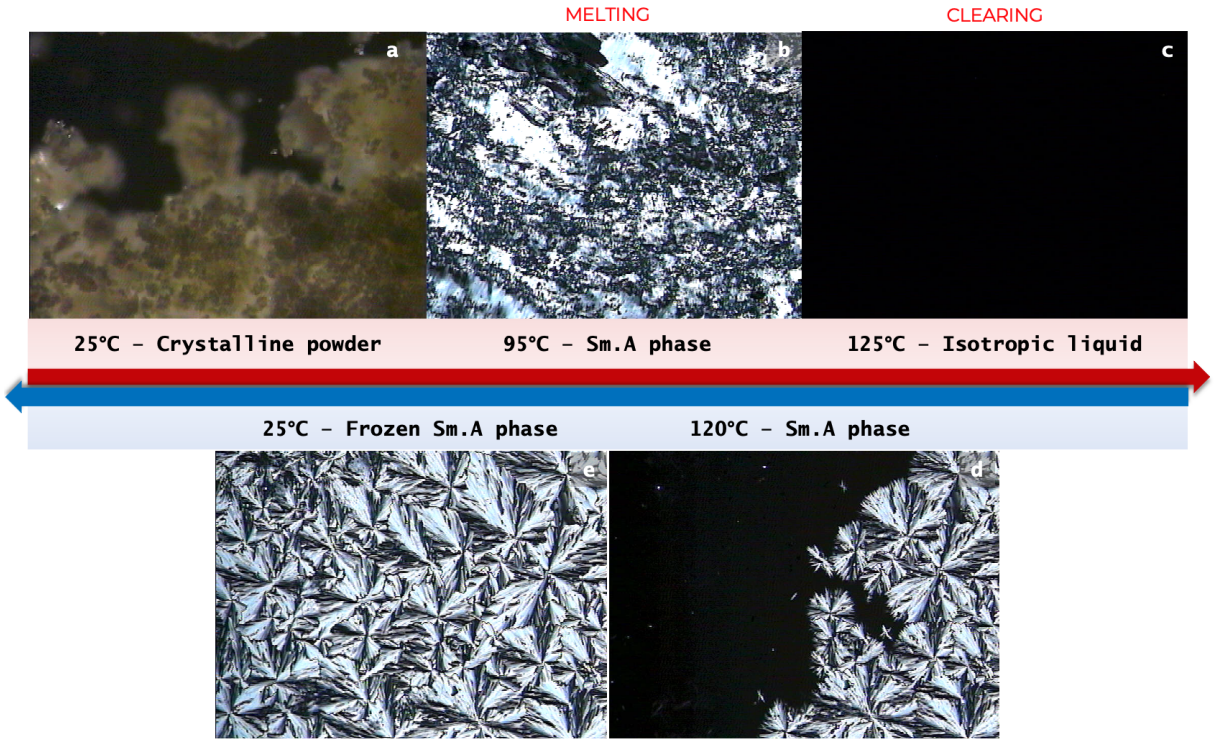

Figure 3.50: POM images of the BrF-MetImI salt with T ranging from 25°C to 150°C, heating (a, b, c) and cooling (d, e) with an heating rate of 10°C/min.

Increasing the temperature, the sample exhibits a Cr-to-LC transition LC around 95°C and a clearing point at $\simeq$ 125°C. The optical texture observed in the liquid crystalline mesophase is characteristic of a Sm.A phase which is probably formed as a consequence of the packing of the multibranched fluorinated portions that result in an ordered structure, as the LinF-MetImI sample. Cooling down the temperature to 25°C the sample returns to the liquid crystalline phase and it did not crystallize forming at room temperature a glassy mesophase that maintains the structural organization given by the LC phase. In good agreement with what has been observed, the DSC thermogram shown in Figure 3.51 exhibit two endothermic peaks related to the Cr-to-LC and LC-to-Iso transitions during heating and only one exothermic peak at 116°C detected during cooling.

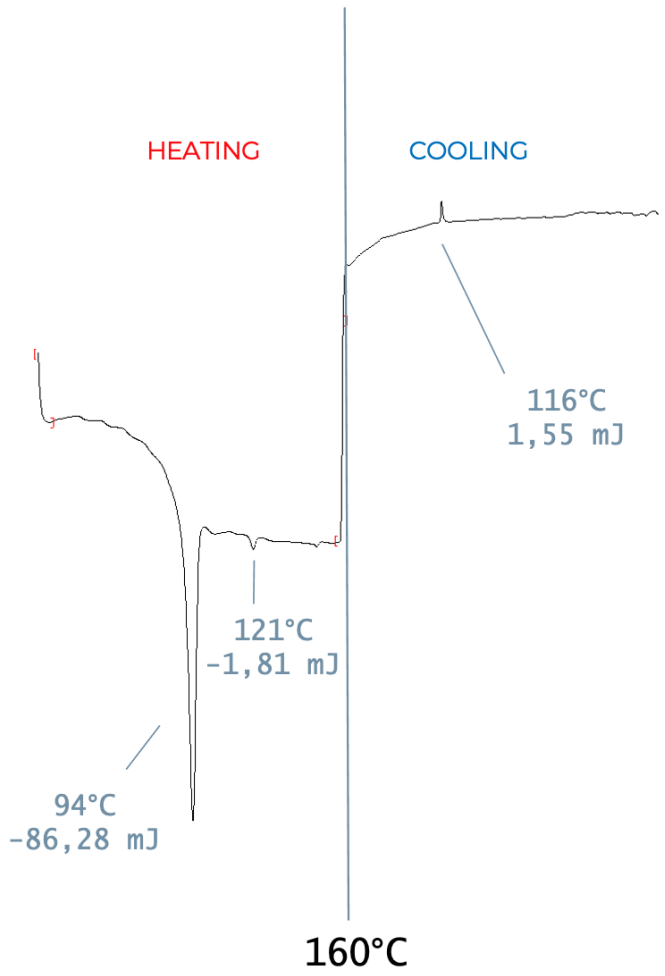

Figure 3.51: DSC results of the BrF-MetImI salt with an heating rate of 10°C/min.

Interestingly the perovskite exhibits the same enantiotropic mesomorphism with a Cr-to-LC transition around 65°C, a clearing point at 215°C and, as in the BrF-MetImI sample, upon cooling the sample from its isotropic state to room temperature, the typical texture of the SmA phase remained unchanged in a frozen state visible in Figure 3.52e. Moreover, no crystallisation occurred even after storing the sample in the refrigerator (-20°C) for several days. Also in this instance, repetitive heating and cooling cycles with POM proved that the liquid crystalline properties are completely reversible. Notably, the perovskite has a lower Cr-to-LC transition temperature than the branched imidazolium salt. Since melting temperatures depend on the interactions between molecules and the solid-state organization, one hypothesis could be that the steric and geometrical requirements in the perovskite lead to weaker interactions, resulting in lower melting points.

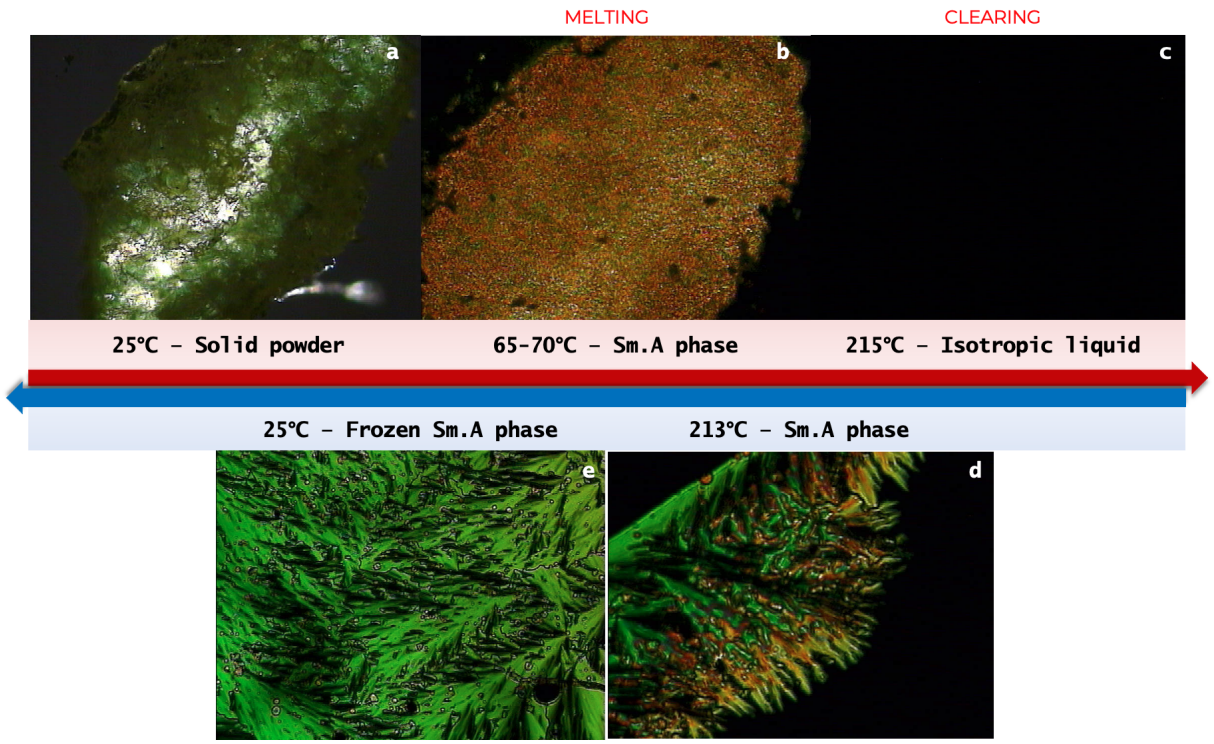

Figure 3.52: POM images of the (PbI_2):(BrF-MetImI) perovskite with T ranging from 25°C to 250°C, heating (a, b, c) and cooling (d, e) with an heating rate of 10°C/min.

Table 3.7: Phase transition temperatures and mesophase temperature ranges measured by heating and cooling the samples. Crystal phase (Cr), smectic A phase (SmA) and isotropic phase (Iso).

	Cr−SmA	**SmA−Iso**	**ΔT**
BrF-MetImI	95°C	121°C	26°C
(PbI_2):(BrF-MetImI)	65°C	215°C	150°C

In addition, the Cr-to-LC transition is shifted to much lower temperatures compared to the perovskite containing the linear perfluoalkyl imidazolium cation, making this material more desirable optoelectronic devices. Indeed, room temperature liquid crystalline (RT-LC) materials displaying high ionic conductivity are attractive candidates for applications in several electrochemical devices. According to one hypothesis, the greater volume occupied by branched cations may reduce interdigitation between fluorinated portions leading to a lower C-to-LC transition temperature. The presence of a smectic phase also indicates a lamellar structure, similar to that of the linear cation.

3.5. Small Angle X-Ray Scattering (SAXS)

The Small Angle X-Ray Scattering (SAXS) technique provides researchers with distinct opportunities to investigate the structural characterization of nanoscale systems. In contrast to wide-angle X-ray diffraction (WAXD), which focuses primarily on the atomic structure of crystals, small-angle X-ray diffraction (SAXD) allows for the investigation of material structures at relatively large-scale distances, or small angles [104]. SAXS involves the diffraction of large lattice spacing, of the order of tens, hundreds, or even thousands of interatomic distances, as well as the scattering by perturbed or nonperiodic structures of amorphous and mesomorphic materials [105]. A. E. Bradley et al. already synthesized a series of long-chain 1-alkyl-3-methylimidazolium salts with amphiphilic properties and studied the thermotropic phase behavior of these salts using variable temperature small-angle X-ray scattering. The compounds form lamellar, sheetlike arrays in the crystalline phase and an enantiotropic smectic liquid crystalline phase at elevated temperatures; the layer spacing in the crystal and mesophase has been determined from variable temperature SAXS [106]. To date, there have been no comparable analyses of perovskites. Starting from the DSC and POM results, the objective was to investigate the thermotropic phase behavior of the imidazolium salts in comparison to the corresponding perovskites in order to demonstrate with reliable results the enantiotropic behavior of the perovskites, which organize themselves in a thermotropic Smectic A liquid crystalline phase.

3.5.1. (PbI_2):(LinF-MetImI)

SAXS data were collected for LinF-MetImI at different temperatures. At room temperature it is possible to notice a series of peaks between 10° and 28° of 2θ in accordance with the PXRD results. In addition, a narrow peak in the low-angle region at 3.07° appears. As shown in Figure 3.53, upon heating, the peaks in the 10°-28° range become broader and less intense, forming two broad peaks around 16° and 22° when the temperature is higher then 88°C corresponding to the Cr-to-LC transition. On the contrary, the peak at 3.07° shifts slightly to the right but remains quite sharp. The disappearance of the crystalline peaks in the wide-angle region increasing the temperature reflects the increased thermal mobility of the alkyl chains and the reduction of positional order. In contrast, the peak at lower angles that remains acute at 150°C indicates that the material exhibits the typical large-scale order of an LC material.

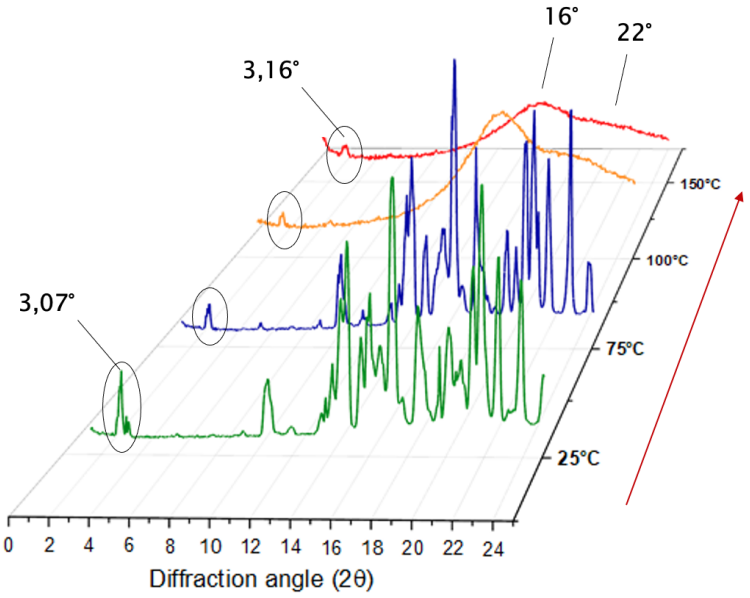

Figure 3.53: SAXS diffraction spectra of LinF-MetImI at different temperatures (25°C, 75°C, 100°C and 150°C). The long-scale order is maintained at high temperatures and the narrow peak at 3° can be associated to the (0,0,1) crystallographic plane.

Afterwards, the (PbI_2):(LinF-MetImI) perovskite was analysed in the same way (Figure 3.54).

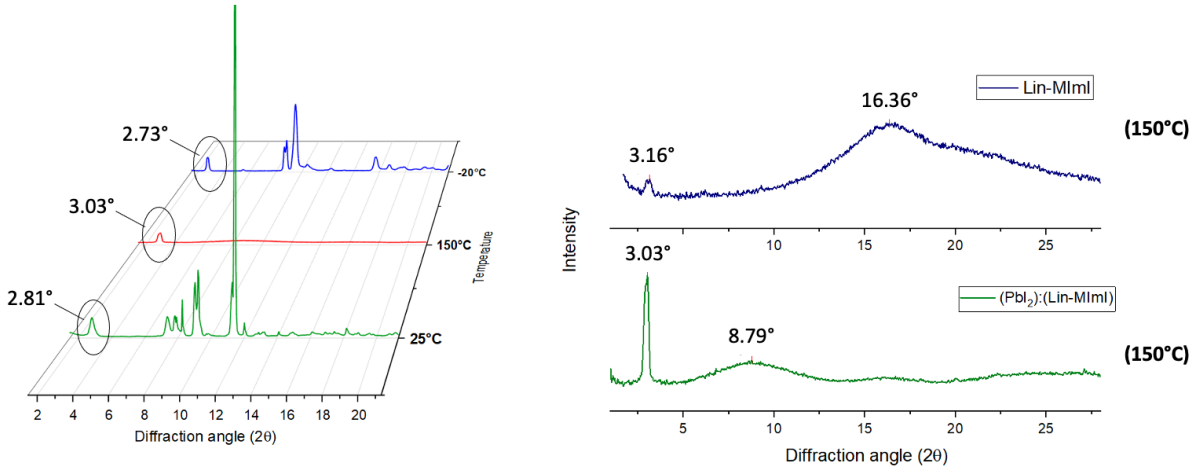

Figure 3.54: SAXS diffraction spectra of (PbI_2):(LinF-MetImI) at different temperatures (25°C, 150°C and -20°C) and comparison between the spectra of the (PbI_2):(LinF-MetImI) and LinF-MetImI samples at 150°C.

According to the PXRD analysis, at room temperature, a series of peaks emerge at lower angles with respect to the LinF-MetImI salt, between 6° and 12°, as a result of the dif-

ferent size of the anion and consequently the greater spacing between the crystal planes. Moreover, a peak was detected at 2.81°. This peak is superimposable with the spectrum generated by the crystallographic software Mercury and corresponds to the (001) layer repeat unit depicted in Figure 3.55. Exploiting the Bragg's law, this peak at 2.81° corresponds to a d-spacing value of almost d = 31 Å. Since the crystal layer spacing is l < d < 2l, where $l = 16.6$ is the fully extended length of the cation calculated by the software Mercury, this highlights that the perfluoroalkyl chains of the cations are interdigitated as already seen in the crystal structure (Figure 3.56).

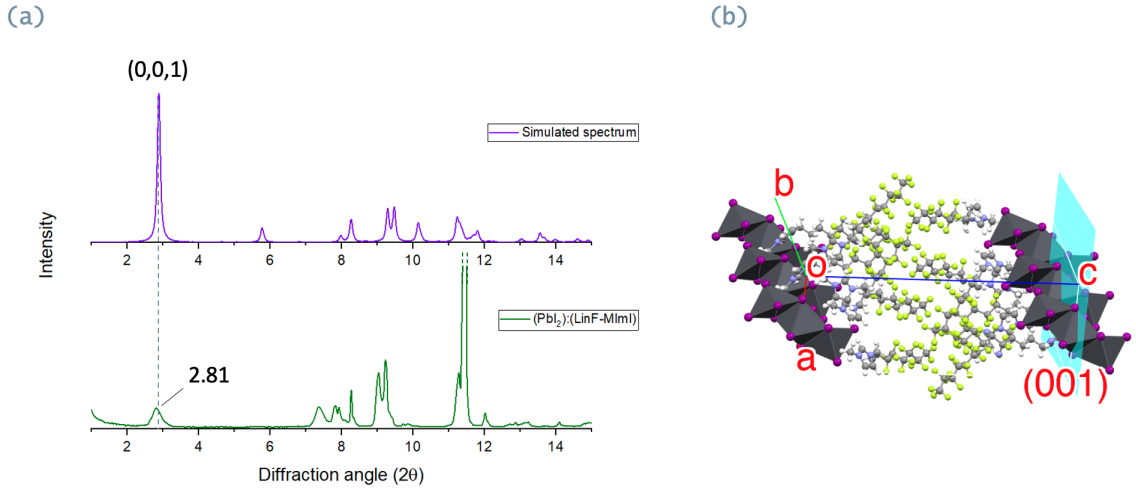

Figure 3.55: (a) Comparison between the (PbI_2):(LinF-MetImI) SAXS specturm and the simulated single crystal spectrum. (b) Visual representation of the (0,0,1) plane.

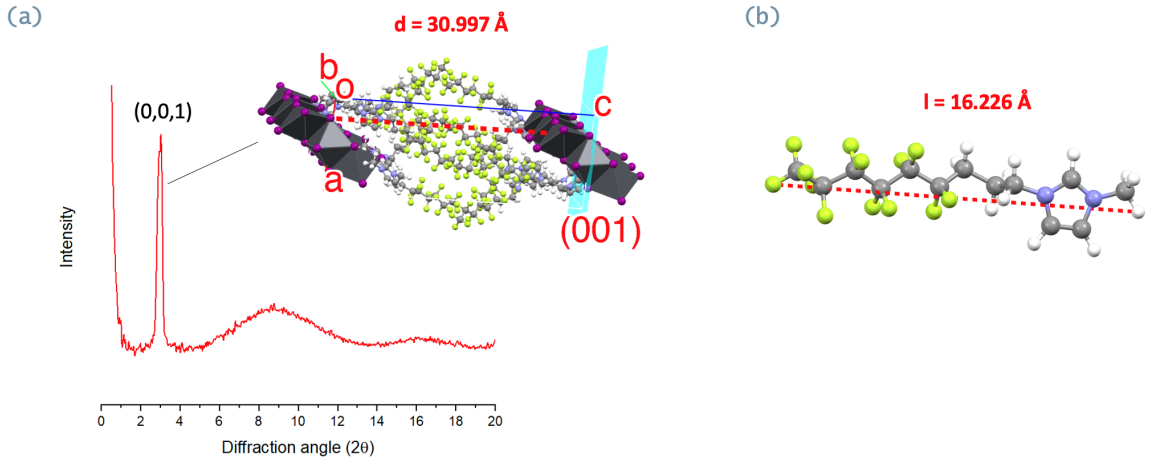

Figure 3.56: (a) Visual representation of the (0,0,1) plane and length of the c axis, d, measured with the crystallographic software Mercury. (b) Visual representation of the perfluoralkyl imidazolium cation with length, l, measured with the crystallographic software Mercury.

As the temperature increases above the Cr-to-LC transition (corresponding to 134°C), the peaks in the wide-angle region became less intense and broader as a result of the increasing movement of the perfluoroalkyl chains (Figure 3.54), whereas the peak in the low-angle region remains visible and distinct and slightly shifts to the right (3.03°). Notably, this peak at 2.81° is slightly broader and shifts to higher angles when the material is melted, both in the case of the imidazolium salt and in the perovskite. This is probably a consequence of the movement of the perfluoroalkyl chains that show a better interdigitation in the LC mesophase at 150°C.
Cooling down the perovskite to room temperature crystallization occurred. As shown in Figure 3.57, the new peaks are arranged differently than the initial peaks at 25°C suggesting a different crystalline phase. It appears that the structure of the material is reorganized differently after melting. This is further demonstrated by the fact that the peak at 2.81°, which corresponds to the (0,0,1) axis, also shifts to the left at 2.73° after melting due to the distinct spatial distribution of the fluorinated chains after the LC-phase transition.

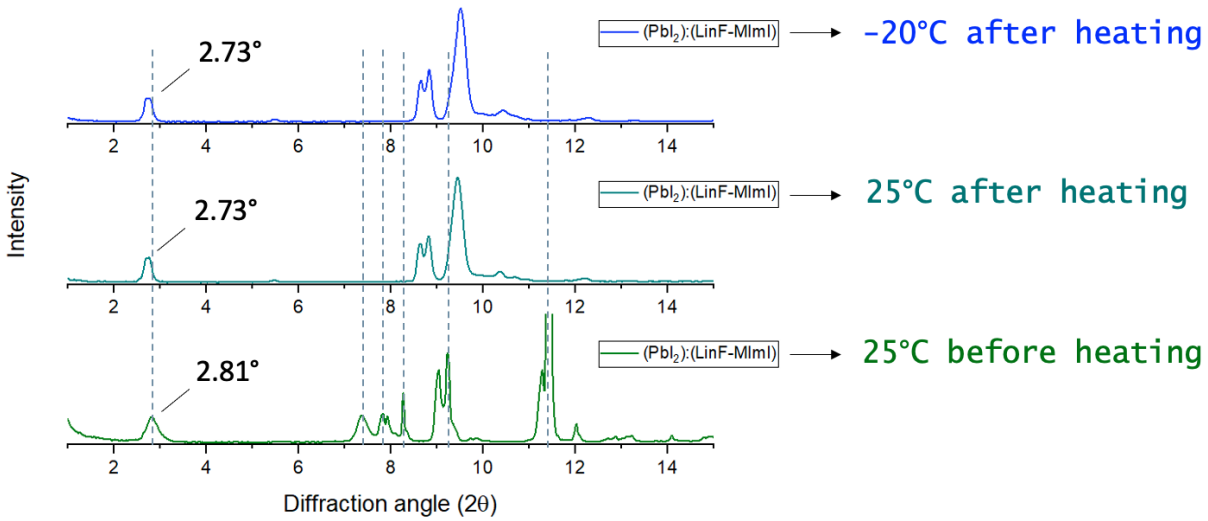

Figure 3.57: (PbI_2):(LinF-MetImI) SAXS spectra comparison at 25°C befroe heating, 25°C after cooling and -20°C. The peak found at 2.81° shifts to the left after the melting and the wide-angle peaks are differently disposed.

As conclusion, in accordance with the result obtained from POM and DSC analyses, we can deduce that, as the starting imidazolium salt, the perovskite shows a smectic phase thermotropic behaviour. Interestingly, the broad peaks shown by the perovskite are the same with respect to the starting imidazolium salt, but shifted to lower angles. This could be associated to the different dimensions of the anions in the starting imidazolium salt (LinFMImI) and the final perovskite resulting in higher distances between the lamellar

planes in the LC phase. The narrow peak at low angles is more or less in the same position and, by analogy with the crystalline structure, it can be associated with the fluorinated chains that do not change after the reaction with lead iodide. These fluorinated chains of the imidazolium cation are moving more and more increasing the temperature and with the thermal input the material organize itself in a different way. Then, cooling down the structure crystallize and the broad peak became sharp and narrow.

3.5.2. (PbI_2):(BrF-MetImI)

The same analyses with the same experimental conditions were performed also in the branched case. As shown in Figure 3.58 the BrF-MetImI salt at room temperature shows narrow peaks in the 10°-25° region in accordance with the PXRD results. Increasing the temperature over the Cr-to-LC transition (corresponding to 95°C) the peaks became broader and less intense.

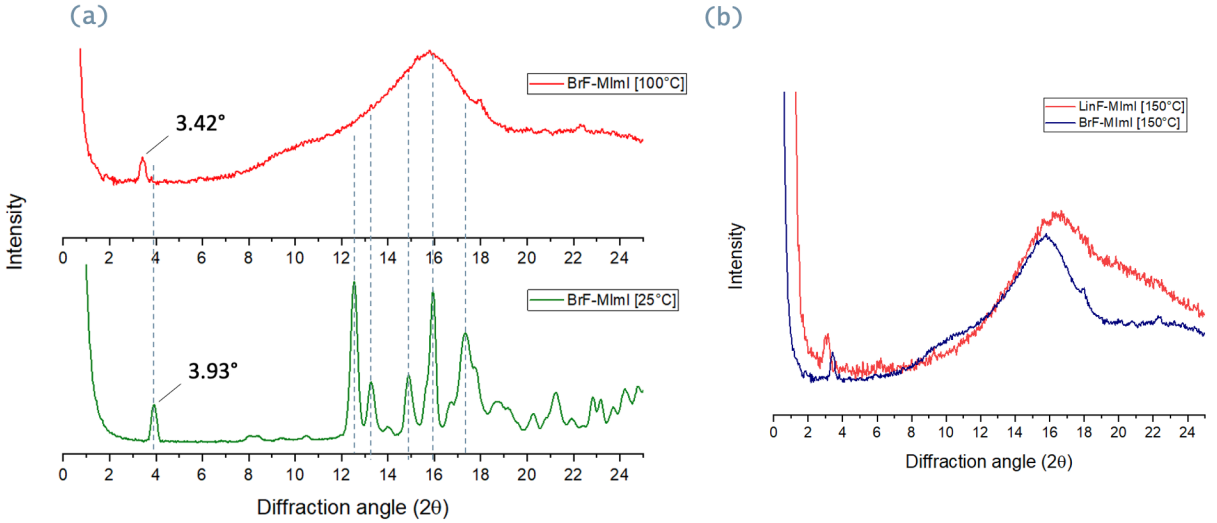

Figure 3.58: (a) SAXS diffraction spectra of the BrF-MetImI sample at 25°C and 150°C. (b) Comparison between the SAXS spectra at 150°C of the BrF-MetImI and the LinF-MImI compounds.

The same behaviour was detected also for the (PbI_2):(BrF-MetImI) perovskite. In this case, as shown in Figure 3.59, narrow peaks were present in the 6°-10° region which disappear becoming a unique broad peak with low intensity increasing the temperature over the Cr-to-LC transition at 65°C. Furthermore, both in the branched imidazolium salt and in the perovskite, it is possible to notice a narrow peak in the low-angle region of 2θ which remains sharp and intense even for temperature higher than the Cr-to-LC transition indicating a large-scale order in the materials also in the molten state, typical of a LC phase. By analogy with the other cases previously analysed, we can assume that the fluorinated chains will interact similarly. In fact, the most intense peak in the low-angle region suggest a crystalline structure with a long axis repeat unit probably given by the self-assembly of the fluorinated portion of the imidazolium cation. This long-range order in the molten state demonstrates that also the (PbI_2):(BrF-MetImI) perovskite undergoes a Cr-to-LC phase transition, as predicted by the POM analysis. Consequently, a lamellar structure typical of the smectic phase can be hypothesized also in this case. The steric

hindrance of the fluorinated determines the distance between the lamellar structures which is different with respect to the linear case as the narrow peak in the low-angle region shifts at higher values of 2*theta* compared to the LinF-MetImI case (Figure 3.59b).

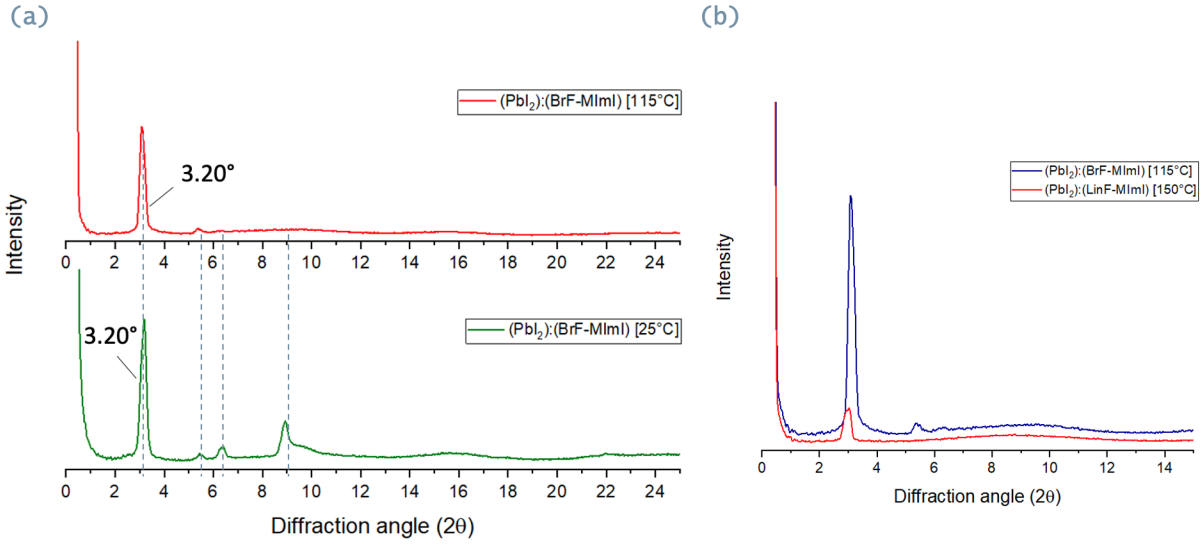

Figure 3.59: (a) SAXS diffraction spectra of the (PbI_2):(BrF-MetImI) sample at 25°C and 115°C. (b) Comparison between the SAXS spectra of the (PbI_2):(BrF-MetImI) at 115°C and the (PbI_2):(LinF-MetImI) at 150°C.

To better comprehend how this structure is packed, however, a synchrotron evaluation of the single crystal is required. After conducting this analysis, we can conclude that the (PbI_2):(BrF-MetImI) perovksite exhibits a similar pattern to the linear case. Based on this result and other previously obtained data, we can hypothesize a mesophase with a lamellar structure in which the fluorinated cations are packed differently owing to their distinct spatial organization. Notably, the liquid crystalline organization is more stable than the linear case, and the same pattern is maintained in a glassy mesophase even at -20°C, as shown in Figure 3.60. This is consistent with what was observed previously with POM. Since the material forms a glassy mesophase and the molecules are still organized as in the LC phase, but are not moving, the narrow peak at lower angles is more intense.

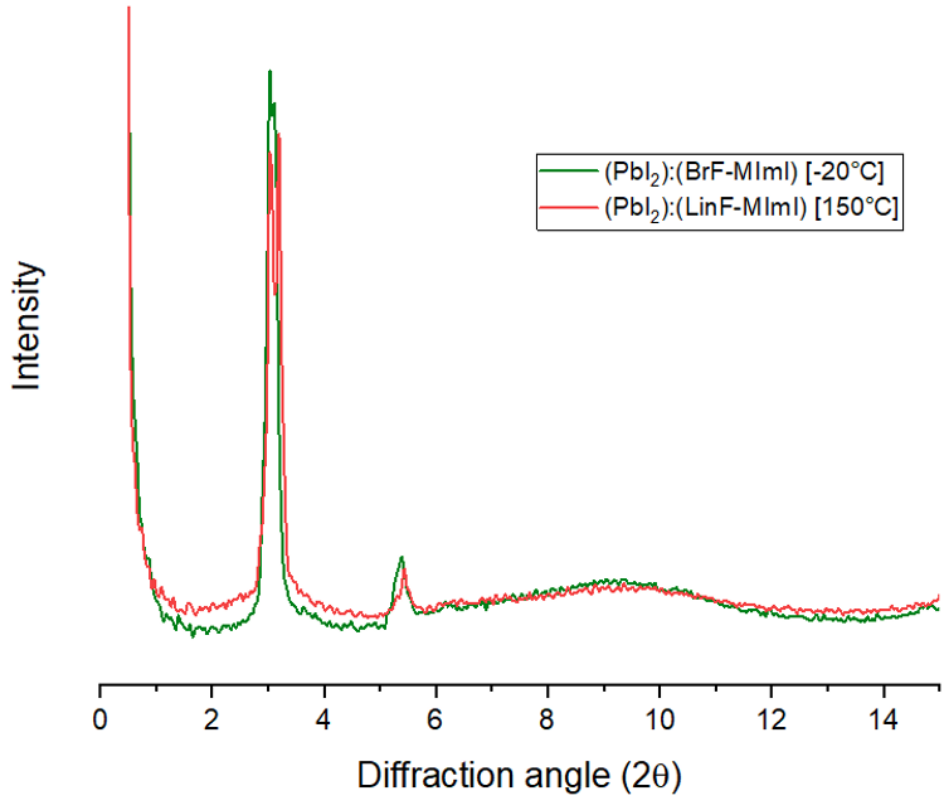

Figure 3.60: Comparison between the SAXS diffraction spectra of the (PbI_2):(BrF-MetImI) sample at 150°C and -20°C.

4 | Materials and methods

4.1. Syntheses description

4.1.1. Multibranched fluorinated amine: BrF-NH_2

To obtain the multibranched fluorinated amine (BrF-NH_2) a series of well-known and optimized reactions were done. Initially, the primary objective was to obtain the alcohol perfluorinated derivative via the various procedures outlined in Figure 4.1:

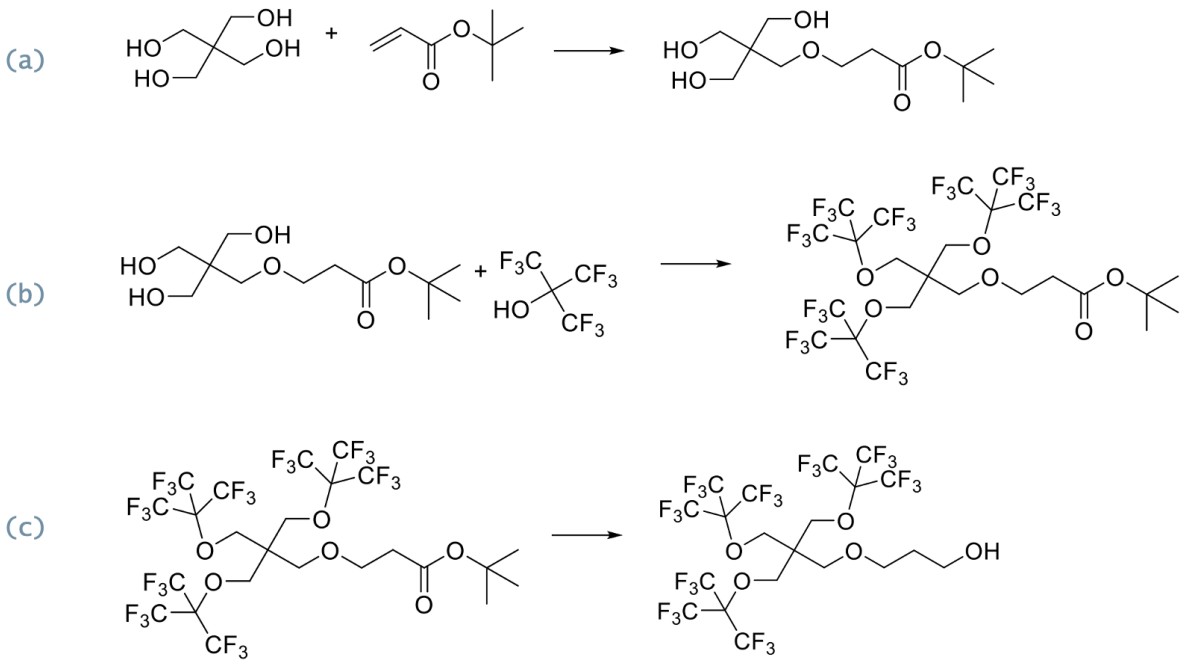

Figure 4.1: Scheme with all the reactions steps, respectively: (a) Michael addition, (b) Mitsunobu reaction, (c) Reduction to alcohol.

a. Michael additions are C-C bond formation reactions in which nucleophilic addition of a carbanion or another nucleophile to an α,β-unsaturated carbonyl compound containing an electron withdrawing group occurs [107]. A solution of NaOH (sodium hydroxide) in water was prepared in a flask. Separately, in a round-bottom flask the

pentaerythritol (2,2-bis(hydroxymethyl)propane-1,3-diol) was dissolved with DMSO (dimethyl sulfoxide) at 80°C. The NaOH solution was subsequently added in one portion to the reaction solution and the tert-butyl acrylate was added slowly to the reaction mixture. The reaction was maintained at 80°C while being stirred.

Table 4.1: Experiment data for Br-TBt (branched tert-butyl terminated molecule).

	Eq.	mmol	MW [g/mol]	W [g]	Density [g/mL]	V [mL]
Pentaerythritol	1	18,99	136,15	2,6	/	/
Tert-butyl acrylate	1,2	22,79	128,17	2,92	0,88	3,32
NaOH	0,2	3,8	39,997	0,15	/	/
DMSO	/	/	/	/	/	5,2

After 1 day, in order to check the formation of the reaction product, a micro-extraction was made with brine solution and ethyl acetate. Then a TLC was made on the ethyl acetate phase. Once the reaction was stopped, at room temperature a solution of HCl 2M was added to obtain an acid pH and favour the extraction of the final product with water and ethyl acetate. Finally, 2,51 g of Br-TBt (Br = branched; TBt = tert-butyl terminated molecule, Figure 4.1a) were obtained with a reaction yield of 50%.

b. The Mitsunobu reaction involving the activation of a hydroxyl group with the combination of triphenylphosphine (PPh_3) and dialkyl azodicarboxylate (DIAD), and its subsequent replacement with a nucleophile, has been widely used in carbohydrates for the introduction of halogen atoms [108]. The procedure adopted is as follows: initially, triphenylphosphine was deposited in a round-bottom flask under a nitrogen atmosphere. The previous step's product (Br-TBt) was then transferred inside with dry THF, and DIAD was added at 0°C to prevent a vigorous exothermic reaction. Few minutes later, when the reaction mixture became a white slurry during stirring at room temperature, the perfluoro-tert-butanol (C_4HF_9O) was added slowly at 0°C. Finally, all the mixture was stirred at 45°C in nitrogen atmosphere.

Table 4.2: Experiment data for BrF-TBt (fluorinated branched tert-butyl terminated molecule).

	Eq.	mmol	MW [g/mol]	W [g]	Density [g/mL]	V [mL]
Br-TBt	1	9,5	264.3	2,51	/	/
C_4HF_9O	6	57	206	11,7	1,7	6,9
PPh_3	6	57	262,3	14,9	/	/
DIAD	6	57	202,2	11,5	1,027	11,2
THF dry	/	/	/	/	/	70

The product was detected after 4 days with a TLC exploiting its apolarity with respect to the initial reagent. To achieve the purification of the product, the mixture was firstly dried with the Rotavapor, followed by an extraction with dichlorometane and water, and then sodium sulphate was added to the organic phase to remove any remaining water. Then the organic phase was filtrated with dichloromethane and dried with the Rotavapor once more. The final phase after the extraction was the crystallisation of the final product: methanol was added until a solid was formed at room temperature to the bottom of the round-bottom flask. Everything was subsequently heated on a plate until the solid completely dissolved, placed the flask in ice, and when a solid product was formed at the bottom of the flask, the mixture was filtered in a Buckner apparatus with methanol. In this way 4,35 g of a white solid (BrF-TBt, Figure 4.1b) were obtained with a reaction yield of 50%.

c. The reduction of the molecule to alcohol was accomplished by transferring the product of the previous step (BrF-TBt) into a bottom-round flask with dry THF and the addition of lithium aluminum hydride ($LiAlH_4$). The mixture was then maintained under stirring for 1 day at room temperature. After that, some drops of HCl were added until the mixture stopped boiling in order to deactivate the $LiAlH_4$, subsequently an extraction with ethyl acetate and water was done. Finally sodium sulphate was added to the organic phase which was then filtered and dried with the Rotavapor (BrF-OH, Table 4.4).

Table 4.3: Experiment data for BrF-OH (fluorinated branched alcohol).

	Eq.	mmol	MW [g/mol]	W [g]	Density [g/mL]	V [mL]
BrF-TBt	1	4,73	918,38	4,35	/	/
$LiAlH_4$	3	14,19	37,95	0,54	/	/
THF dry	/	/	/	/	/	85

Table 4.4: Quantity of product obtained (BrF-OH) and reaction yield.

	W [g]	Reaction yield
BrF-OH	3,7	93%

At this point, once the alcohol has been synthetized, part of it was later used as reagent to obtain the mesyl terminated perfluorinated derivative BrF-Ms (Ms=mesyl terminated molecule). Starting from this molecule, the azide derivative was synthetized and, finally, the amine derivative. The adopted procedure is described in the following lines.
In a round bottom flask the alcohol was transferred and dissolved in anhydrous CH_2Cl_2. Triethylamine (Et_3N) was then added at 0 °C, followed by methanesulfonyl chloride (MsCl). The process was conducted at room temperature, in a nitrogen environment, and under stirring. After 4 days an extraction with dichloromethane and brine was made and the organic phase was dried with sodium sulphate and evaporated with the Rotavapor (BrF-Ms, Table 4.6).

Table 4.5: Experiment data for the BrF-Ms (fluorinated branched mesyl terminated molecule).

	Eq.	mmol	MW [g/mol]	W [g]	Density [g/mL]	V [mL]
BrF-OH	1	2,55	848,29	2,2	/	/
MsCl	3	7,64	114,55	0,9	1,48	0,6
Et_3N	3	7,64	101,19	0,8	0,73	1,1
CH_2Cl_2	/	/	/	/	/	29,58

Table 4.6: Quantity of product obtained (BrF-Ms) and reaction yield.

	W[g]	Reaction yield
BrF-Ms	2,27	96%

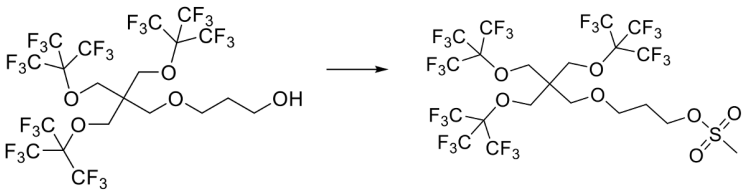

Figure 4.2: Reaction scheme (BrF-Ms).

For the preparation of the azide derivative 2,27 g of mesyl perfluorinated derivative were dissolved in a round-bottom flask with anhydrous DMF, then sodium azide (NaN_3) was added slowly at 0°C. The mixture was kept under stirring at 80°C for 5 days. For the extraction the mixture in the flask was poured into a beaker with ice under stirring and, when the ice was all melted, an extraction with water and hexane was done. The organic part was then dried with sodium sulphate and evaporated. Finally, 1.8 grams of what appears to be a white oil were obtained (BrF-N_3, Table 4.8).

Table 4.7: Experiment data for the BrF-N_3 (branched fluorinated azide derivative).

	Eq.	mmol	MW [g/mol]	W [g]	Density [g/mL]	V [mL]
BrF-Ms	1	2,45	926,38	2,27	/	/
NaN_3	2	4,9	65,01	0,319	/	/
DMF dry	/	/	/	/	/	26

Table 4.8: Quantity of product obtained (BrF-N_3) and reaction yield.

	W [g]	Reaction yield
BrF-N_3	1,8	84%

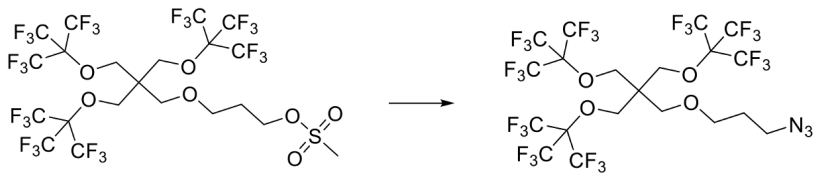

Figure 4.3: Reaction scheme (BrF-N_3).

The last step was the synthesis of the perfluorinated amine derivative. The Staudinger reaction's mechanism was adopted [109, 110]. The triphenylphosphine reacts with the azide to generate a phosphazide, which loses N_2 to form an iminophosphorane. Aqueous work up leads to the amine and a very stable phosphine oxide. Thus, the perfluorinated azide derivative was dissolved in a round-bottom flask with THF, then at 0°C the triphenylphosphine was added. The reaction mixture was left under stirring for 10 minutes and during this time, as a consequence of the formation of the triphenylphosphine adduct which leads to the release of nitrogen, some bubbles were visible. Subsequently, 1,1 mL of Milli-Q water were added and the reaction was left one more under stirring overnight at 45°C. After 1 day, the reaction was checked with a TLC, and, since the triphenylphosphine adduct was still present, 1,5 mL of Milli-Q were added and the reaction was left again under stirring at 70°C with reflux.

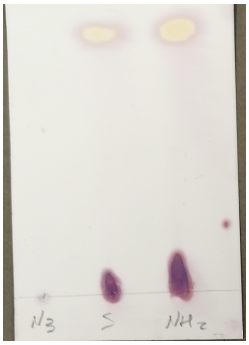

Figure 4.4: TLC after 72h of stirring dipped in Ninhydrin.

After 48h, when a yellowish oil was clearly visible at the bottom, the stirring was stopped and the reaction mixture was poured in a becker with an acid solution of HCl so that the product became soluble in water. An extraction with acid water and dichloromethane was made and to check that the amine derivative was dissolved in water a TLC in ninhydrin was made. After that, a basic solution with NaOH in water was prepared and then the amine derivative was dissolved in the organic phase and separated from the starting reagents and the intermediate triphenylphosphine adduct by performing a sec-

ond extraction with basic water and chloroform. Finally, sodium sulphate was added to the organic phase to remove the residual water, and the product was filtered and dried with the Rotavapor obtaining a white powder (BrF-NH_2).

Table 4.9: Experiment data for the BrF-NH_2.

	Eq.	mmol	MW [g/mol]	W [mg]	Density [g/mL]	V [mL]
BrF-N_3	1	0,49	873,31	430	/	/
PPh_3	1,5	0,74	262,29	194	/	/
THF	/	/	/	/	/	10,7
Milli-Q water	/	/	/	/	/	2,6

Table 4.10: Quantity of product obtained (BrF-NH_2) and reaction yield.

	W [mg]	Reaction yield
BrF-NH_2	226	54%

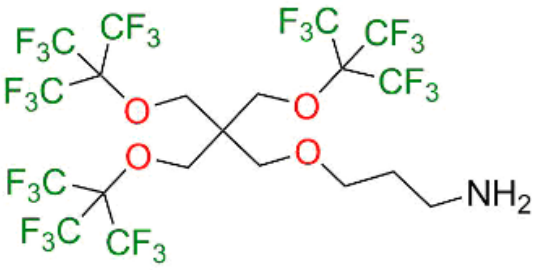

Figure 4.5: Picture of the white solid obtained (BrF-NH_2).

After the synthesis, few mg of the product were dissolved in deuterated methanol that was characterized by ^{1}H NMR and ^{19}F NMR to exclude the presence of impurities. From the ^{1}H NMR is possible to see all the distinctive signals of the molecule (Figure 4.6) while from the ^{19}F NMR only one peak is visible which can be correlated to the perfluorinated amine (Figure 4.7).

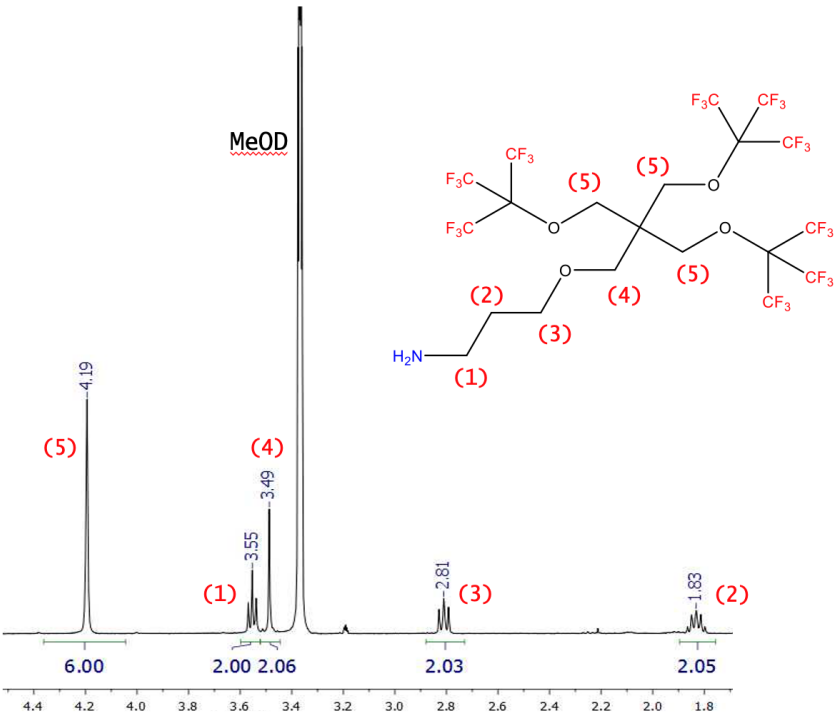

Figure 4.6: ^{1}H NMR of the perluorinated amine molecule (BrF-NH_2) in methanol-d. δ/ppm : 1.83($2H, m, CH_2$), 2.81 (2H,t,CH_2), 3.49 (2H,s,CH_2), 3.55 (2H,t,CH_2), 4.19 (6H,s,CH_2).

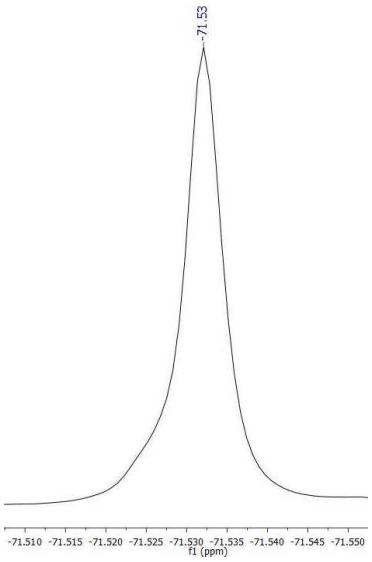

Figure 4.7: ^{19}F NMR of the perluorinated amine molecule (BrF-NH_2) in methanol-d. δ/ppm : 71.53($27F, s$).

4.1.2. Multibranched fluorinated iodinated molecule: BrF-I

In order to synthetize the branched perfluorinated iodinated molecule 300 mg of the alcohol perfluorinated derivative (BrF-OH) obtained with the passages described before (Figure 4.1) were used as starting reagent. The intention was to perform a substitution of the hydroxyl group in a basic environment using the method outlined below (Figure 4.8).

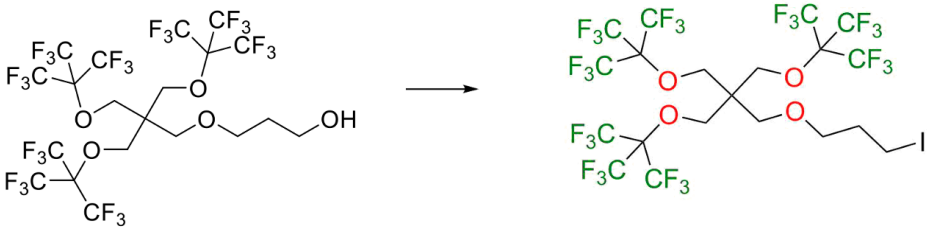

Figure 4.8: Reaction scheme for the BrF-I.

First of all, the iodine (I_2), the imidazole (IM) and the triphenylforphine were added and dissolved in a round-bottom flask with anhydrous dichlorometane under stirring. After that, the alcohol (BrF-OH) was added at 0°C and the reaction mixture was left under stirring at room temperature for 1 day. To remove the starting reagents, sodium thiosulfate (useful for absorbing any remaining iodine) dissolved in water and dichloromethane extraction was done first, followed by another extraction with water and dichloromethane. The organic solution was dehydrated with sodium sulfate, then filtered and dried with Rotovapor. Chromatography column was used to purify from unreacted alcohol detected by TLC. Subsequently the final product was dried at the Rotavapor and placed for one night in fridge. A white solid was obtained (BrF-I, Table 4.12) as shown in Figure 4.9 which at room temperature melted becoming a white oil.

Table 4.11: Experiment data for the BrF-I (multibranched fluorinated iodinated molecule).

	Eq.	mmol	MW [g/mol]	W [mg]	Density [g/mL]	V [mL]
BrF-OH	1	0,35	848,29	300	/	/
PPh_3	1,2	0,42	262,29	110	/	/
IM	1,2	0,42	68,08	28,6	/	/
I_2	1,2	0,42	253,81	106,6	/	/
CH_2Cl_2	/	/	/	/	/	2

Table 4.12: Quantity of product obtained (BrF-I) and reaction yield.

	W [mg]	Reaction yield
BrF-I	209	63%

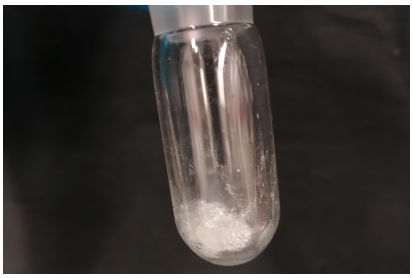

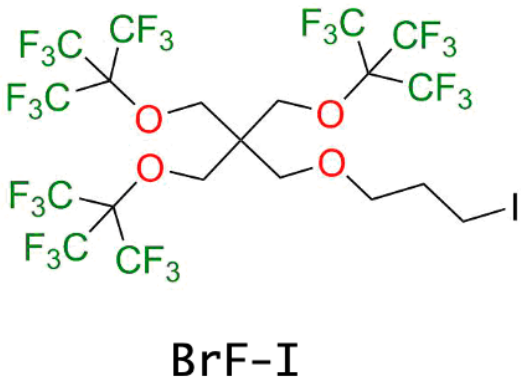

Figure 4.9: Photo of the BrF-I sample after chromatography.

The compound was later characterized by ^{1}H NMR and ^{13}C NMR. As shown in Figure 4.10 and Figure 4.12 the molecule was clean with all its characteristic peaks and without impurities. Looking at the ^{19}F NMR spectra (Figure 4.11) it is possible to see just one peak related to the fluorinated chain of the final product.

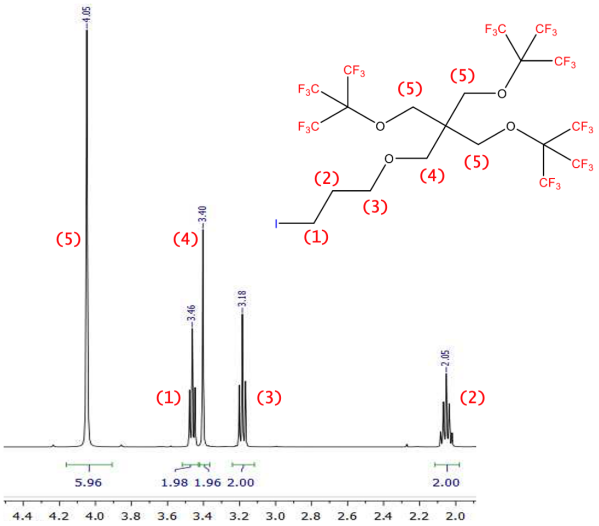

Figure 4.10: ^{1}H NMR spectrum for the branched perfluorinated iodinated molecule (BrF-I) in chloroform-d. δ/ppm : 2.05($2H, m, CH_2$), 3.18 (2H,t,CH_2), 3.40 (2H,s,CH_2), 3.46 (2H,t,CH_2), 4.05 (6H,s,CH_2).

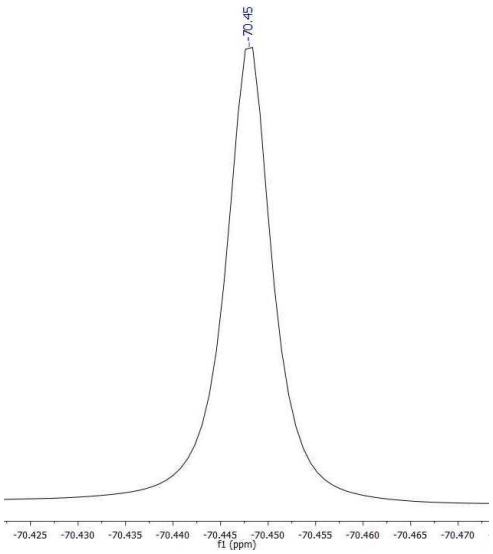

Figure 4.11: ^{19}F NMR spectrum for the branched perfluorinated iodinated molecule (BrF-I) in chloroform-d. δ/ppm : $70.45(27F, s)$.

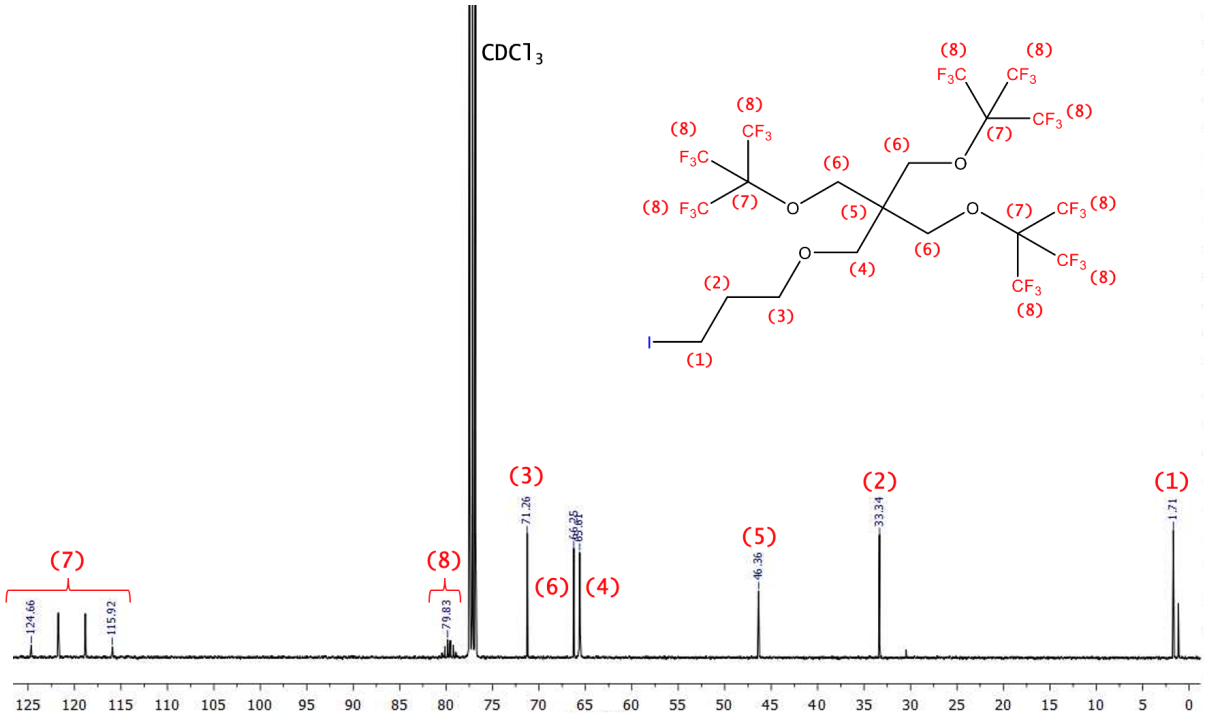

Figure 4.12: ^{13}C spectrum for the branched perfluorinated iodinated molecule (BrF-I) in chloroform-d. δ/ppm: 1.71 (1C,s), 33.34 (1C,s), 46.36 (1C,s), 65.61 (1C,s), 66.25 (1C,s), 71.26 (1C,s), 79.83 (9C,m), from 115.92 to 124.66 (3C,m).

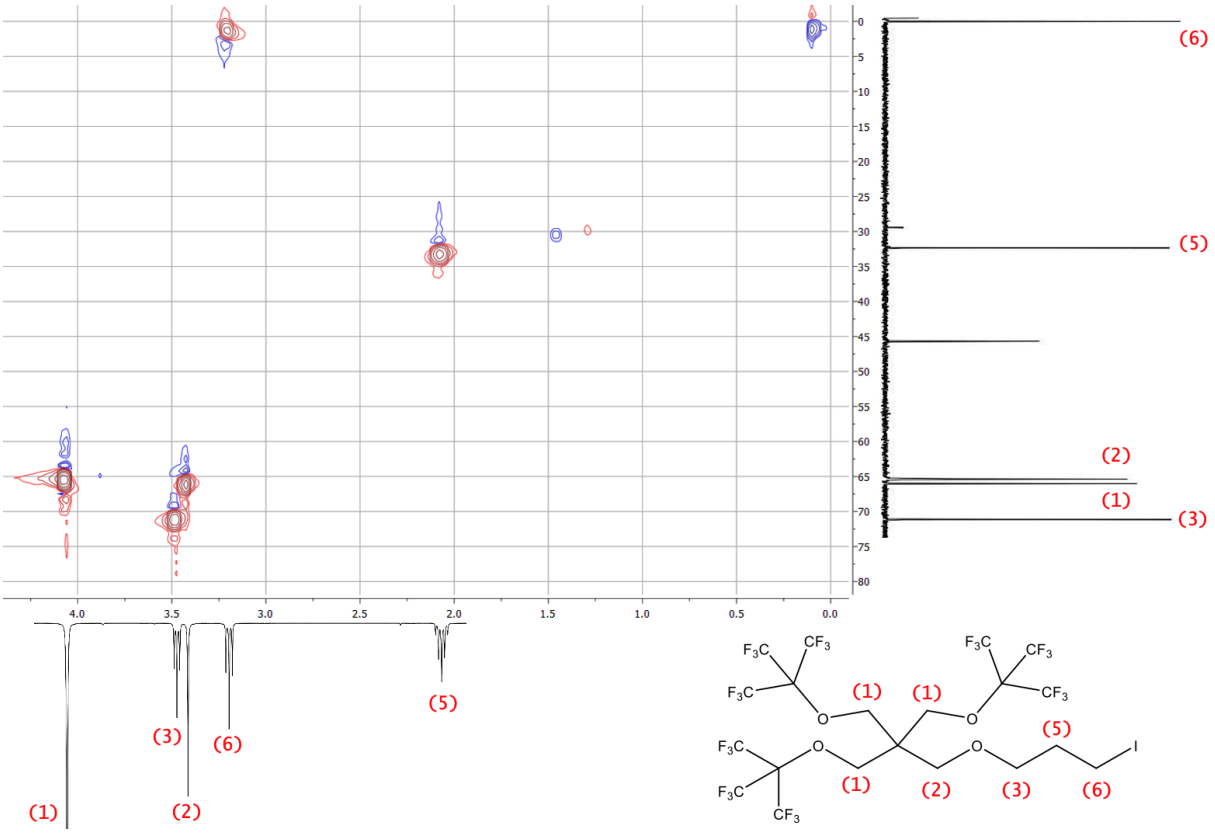

Figure 4.13: 2D NMR comparison between the ^{13}C spectrum and ^{1}H NMR spectrum for the branched perfluorinated iodinated molecule (BrF-I) in chloroform-d.

Finally, a mass spectroscopy was done dissolving 1 mg of the saple in 1 mL of solution with dichloromethane and formic acid (0.1%) to confirm that the compound obtained had the same molecular weight of the iodinated molecule needed for the synthesis of the imidazolium salt, as shown in Figure 4.14.

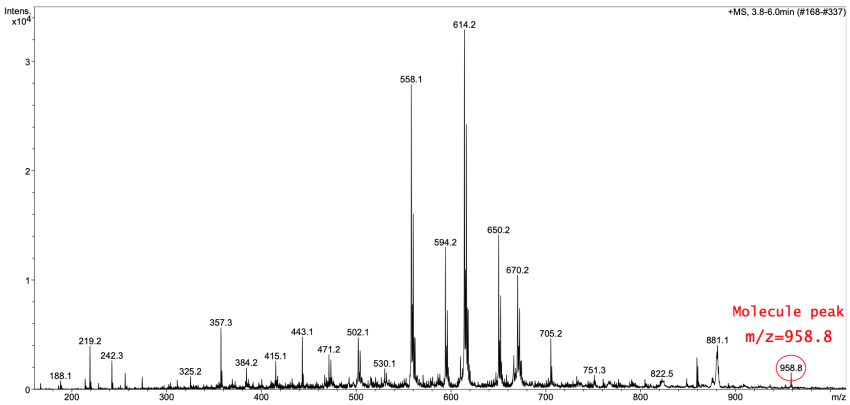

Figure 4.14: Mass spectrum of the branched perfluorinated iodinated molecule (BrF-I) with the molecule peak at m/z=958.8.

4.1.3. Imidazolium salts

- **Perfluoro-alkyl-methyl imidazolium iodide (LinF-MImI)**

  Perfluoro alkyl methylimidazolium iodide was obtained by nucleophilic addition of 1,1,1,2,2,3,3,4,4,5,5,6,6-Tridecafluoro-9-iodo-nonane ($C_9H_6F_{13}I$, from Manchester Organic: purity 95%) to 1-methyl imidazolium. Tridecafluoro-9-iodo-nonane in slight excess was dissolved in toluene and then methyl-imidazolium was added. The solution was stirred for 48 hours at 120°C with reflux. Then, a brown viscous liquid was obtained at the bottom of the round-bottom flask. This phase was dried under vacuum until a yellow powder is obtained, then the compound was characterized by ^{19}H and ^{19}F NMR in chloroform-d. NMR analyses indicated that some residual methyl imidazole remained, with signals in 10-7 ppm region and a singlet related to the methyl group of the methyl imidazole around 4 ppm. Hence, the obtained powder was washed with stirring at 50°C three times with hexane to remove traces of initial reagents. After the removal of the supernatant, the product was dried again under vaccum at the Rotavapor and characterised by ^{1}H in chloroform-d. After the washing it is possible to notice that the characteristic peaks of the starting methyl-imidazole are no more visible and the product is clean.

Table 4.13: Experiment data for LinF-MImI.

	Eq.	mmol	MW [g/mol]	W [mg]	Density [g/mL]	V [mL]
$C_9H_6F_{13}I$	1.2	11.87	488.03	5790	1.83	3.17
M-IM	1	9.89	82.10	811.7	1.03	0.79
Toluene	/	/	/	/	/	35

Table 4.14: Quantity of product obtained (LinF-MImI) and reaction yield.

	W [g]	Reaction yield
LinF-MImI	5,17	91,6%

As shown in Figure 4.15, imidazolium salt signals are expected in three regions:

1. Single H linked to carbon atoms characteristic of the imidazolium ring: a first singlet is present at 10.03 ppm. Then two singlets are present in region between 8 and 7 ppm. All these signals are integrated equal to 1.

2. Singlet related to the methyl group of the imidazolium integrating 3 at 4.07 ppm and a triplet which integrates 2 related to the methylene group near the imidazolium ring at 4.57 ppm.

3. A multiplet between 2 and 3 ppm related to the other two methylene groups, integrating 4.

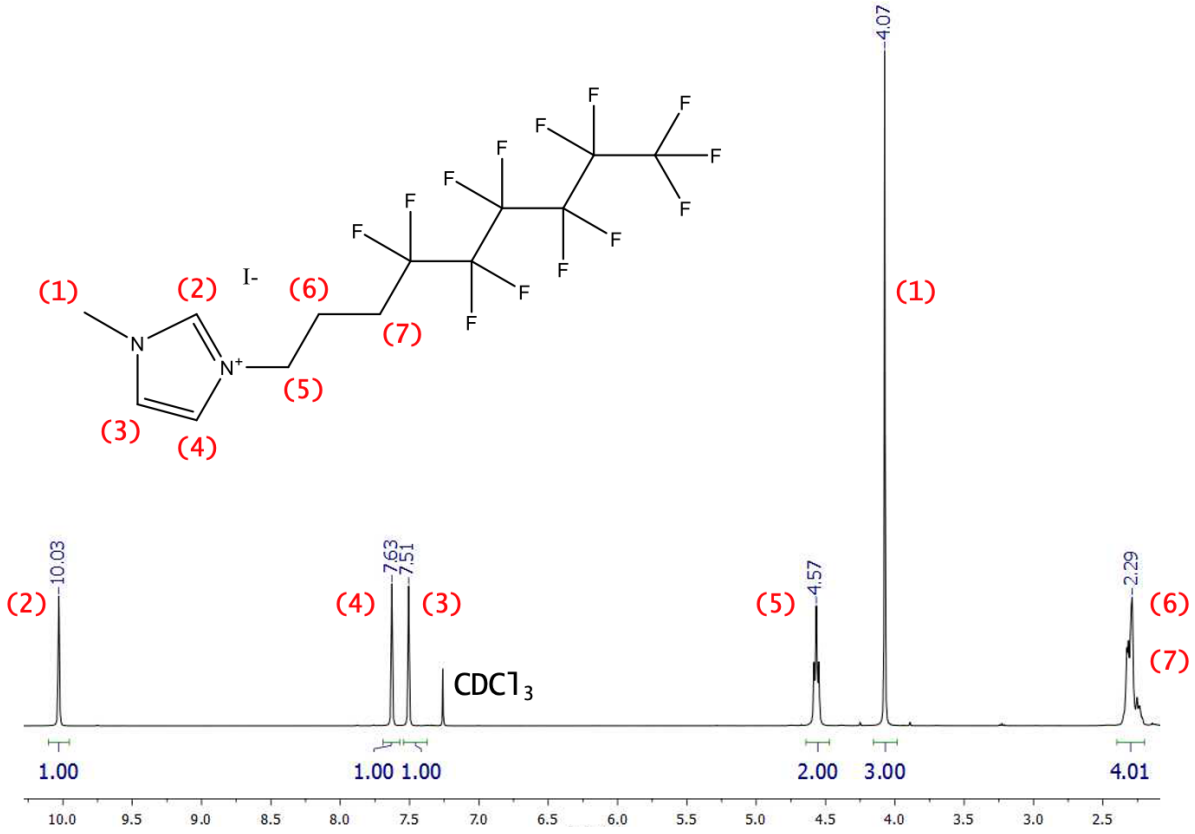

Figure 4.15: Resolved ^{1}H NMR spectrum for LinF-MImI in chloroform-d. δ/ppm : $2.29(m, 4H), 4.07(s, 3H), 4.57(t, 2H), 7.51(s, 1H), 7.63(s, 1H), 10.03(s, 1H)$.

- **Branched perfluoro-methyl imidazolium iodide (BrF-MImI)**

  In the same way the branched perfluoro-methyl imidazolium iodide (BrF-MImI) was obtained by nucleophilic addition of the branched perfluorinated iodinated molecule ($C_{20}H_{14}O_4IF_{27}$, Figure 4.9) to 1-methyl imidazolium (from Sigma Aldrich: MW=82.01 g/mol). Since the quantities of reagents involved in this synthesis are remarkably lower, in order to avoid experimental losses of methyl-imidazole and perform the reaction with a sligthly excess of the perfluorinated iodinated molecule (BrF-I) a solution of Toluene and methyl-imidazolium with the correct concentration of methyl-imidazolium needed for the reaction was prepared. Subsequently, the

perfluorinated branched molecule was added inside and the mixture was stirred for 72 hours at 120°C with reflux. After three days the mixture looks like a yellow oil.

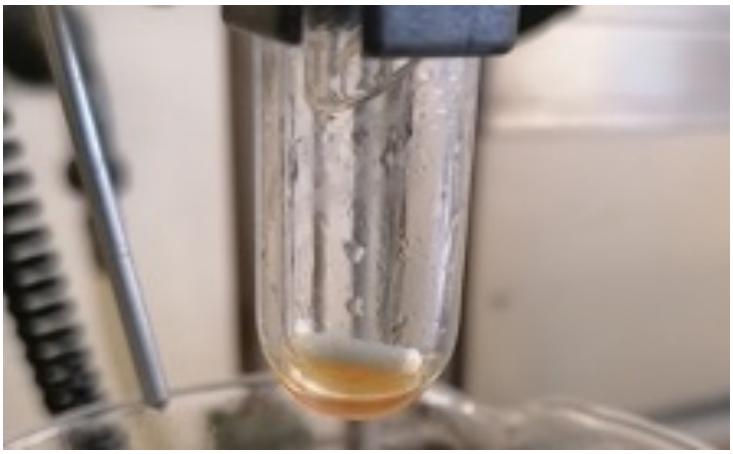

Figure 4.16: Photo of the mixture after 72h of stirring.

The compound was dried at the Rotavapor and washed three times with hexane at 70°C with reflux, each time the surnatant has been collected in order to separate the initial reagents remained from the final product. Once the washing has been done, the compound was dried again at the Rotavapor and finally it looked like a white powder.

Table 4.15: Experiment data for BrF-MImI.

	Eq.	**mmol**	**MW [g/mol]**	**W [mg]**	**V [μL]**
BrF-I	1,2	0,211	958	202	/
M-IM in toluene (1,18 M)	/	/	/	/	150

Table 4.16: Quantity of product obtained and reaction yield for BrF-MImI.

	W [mg]	**Reaction yield**
BrF-MImI	120,4	60%

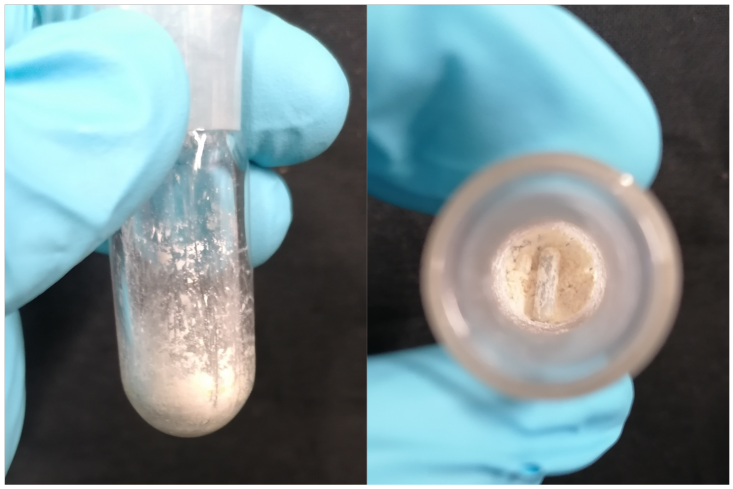

Figure 4.17: Photo of the final product BrF-MImI.

The final product was characterised by ^{1}H NMR and ^{19}F NMR in chloroform-d. As it is possible to see in Figure 4.18 and Figure 4.19 the salt is clean without impurities.

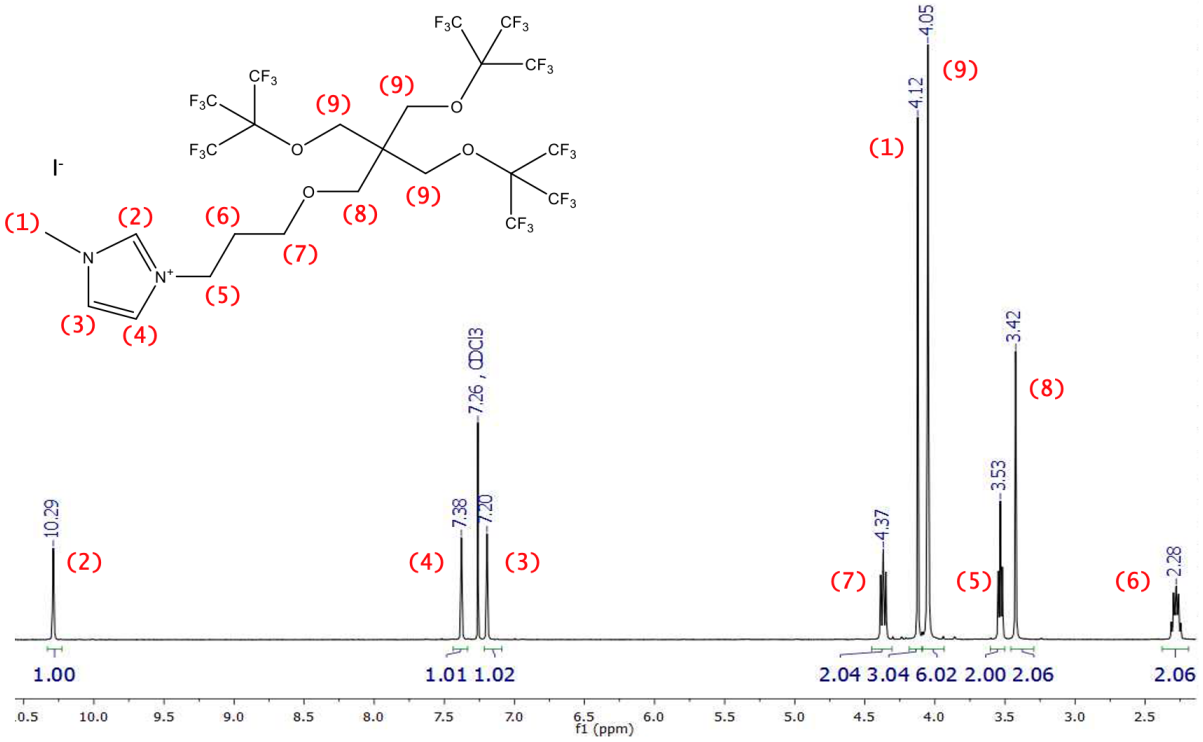

Figure 4.18: ^{1}H NMR spectrum of the BrF-MImI salt in chloroform-d. δ/ppm : 2.28($2H, m, CH_2$), 3.42 (2H,s,CH_2), 3.53 (2H,t,CH_2), 4.05 (6H,s,CH_2), 4.12 (3H,s,-CH_3), 4.37 (2H,t,CH_2), 7.20 (1H,s,NCH), 7.38 (1H,s,NCH), 10.29 (1H,s,NCHN).

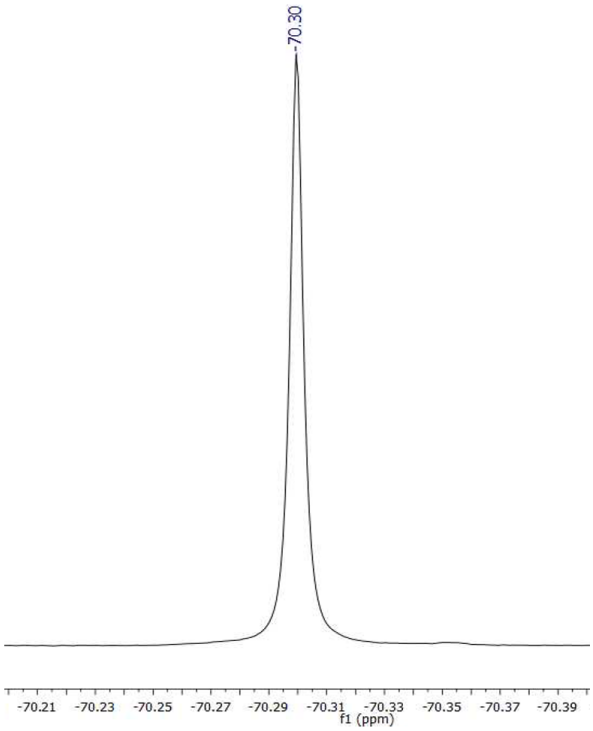

Figure 4.19: ^{19}F NMR spectrum of the BrF-MImI salt. δ/ppm : 70.30($27F, s$).

A further characterization of the sample was done through the mass spectroscopy dissolving 1mg of the product in 1 mL of methanol (Figure 4.20).

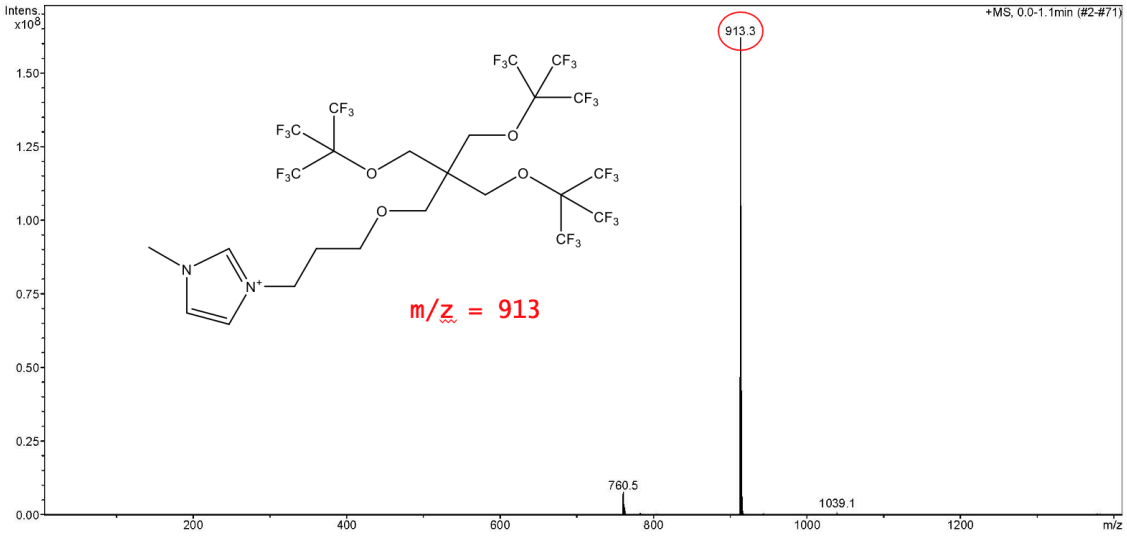

Figure 4.20: Mass spectrum of the BrF-MImI salt. From this spectrum it is possible to see the peak related to the presence of the perfluorinated cation (m/z=913.3).

4.1.4. Perovskites

(PbI_2):(LinF-MImI)

Perovskite synthesis were carried out using imidazolium iodide and PbI_2 with molar ratio 2:1 (PbI_2):(LinF-MImI) [2:1], this reaction happens in excess of HI [90]. Lead (II) iodide (PbI_2, 461.1 g/mol) was purchased from abcr, with purity 98.5% specific for perovskite synthesis. Hydroiodic acid (HI, 127,9 g/mol) was purchased from abcr, as 57% w/w solution stabilized with 1.5% hypophosphorous acid. Imidazolium salt (LinF-MImI) was added to PbI_2 previously dissolved with heating and agitation in a huge excess of HI (30 equivalents with respect to lead iodide). Since in the first reaction was evident the presence of a black byproduct due to the iodide oxidation, the addition of a solution of H_3PO_2 (50 wt.% in H_2O) in the following reactions was necessary in order to prevent this oxidation. Immediately after the addition of H_3PO_2 the solution became clear and the black byproduct was not present anymore. The reaction was first heated at 120°C under stirring and nitrogen atmosphere to enhance the solubility and obtain a clear homogeneous solution of a bright yellow colour. Then, it was left to cool down slowly until the solution became oapque around 100°C. The reaction mixture remained at this temperature overnight and in the next days the temperature was decreased with a controlled cooling rate of 2°C/h. When the solutions reached the room temperature, some thin crystals precipitated in the bottom of the flask. They were collected, dried under vacuum in a sintered glass funnel with the aim of removing the acid mother liquor and subsequently they were washed with methanol. Almost 100mg of shiny yellow platelets were obtained.

Table 4.17: Chemical conditions for the (PbI_2):(LinF-MImI) synthesis.

	Eq.	MW [g/mol]	W [mg]	mmol	V [mL]	M [mmol/mL]
LinF-MImI	2	570.4	247.4	0.434	/	/
PbI_2	1	461.01	100	0.217	/	/
H_2PO_3	45	/	/	/	1	9.4
HI	150	/	/	/	4.3	7.58

(PbI_2):(BrF-MImI)

The perovskite was synthetized starting from the same condition of the PbI_2:$C_9F_{13}MImI^-$ (1:2). Again, the reagents were put in a tube flask with a huge excess of hydroiodic acid (HI, 150eq) with the addition of hypophosphorous acid (H_3PO_2) in order to prevent the oxidation of the HI (Table 4.18). It has to be mentioned that the branched imidazolium

salt was insoluble in the hydroiodic acid. So, in order to improve the reaction conditions and trying to obtain an homogeneous solution to favour the crystallisation of the final product, the branched imidazolium salt was firstly dissolved in methanol (the right quantity to dissolve everything). After that, the lead (II) iodide was placed in a flask with the acids and subsequently the dissolved imidazolium salt was added. Immediately a solid was formed floating in the middle of the flask. The reaction seems to be instantaneous. The solid was left in the solution (the colour of the solution was bright yellow) overnight and under stirring at 120°C. After 24h the solution became clear (probably because all the PbI_2 reacted) still with a yellow solid in the middle. The solid was filtered with Buchner under nitrogen. In this conditions the final product obtained was amorphous and sticky, like a glass. In order to crystallize the final product, it was dissolved in a vial with acetonitrile, the solution was heated until 60°C and the temperature was cooled down slowly until 25°C, then the vial was left in fridge overnight. In this way sharp needles of the final product (Figure 3.5) were obtained. Finally, the solvent was left to evaporate and the needles were collected with a final weight of almost 30mg.

Table 4.18: Chemical conditions for the (PbI_2):(BrF-MImI) synthesis.

	Eq.	MW [g/mol]	W [mg]	mmol	V [μL]	M [mmol/mL]
BrF-MImI	2	1040	30	0.029	/	/
PbI_2	1	461	6.65	0.014	/	/
H_2PO_3	45	/	/	/	23	9.4
HI	150	/	/	/	95	7.58

4.1.5. (PbI_2):(BrF-N_2)

As in the previous reactions the reagents were placed in a tube flask with an excess of hydroiodic acid (HI, 150eq) with the addition of hypophosphorous acid (H_3PO_2) to prevent the oxidation of the HI (Table 4.19). The reaction was left under stirring at 120°C overnight. The day after, a white solid was floating inside the solution and some white solid on top. The solid was collected and checked with the IR (Infrared spectroscopy) and the POM (Polarized Optical Microscope). Probably the white solid was a mixture of the branched amine and the ammonium salt, so it didn't react with the lead iodide. At this point 0,6 mL of methanol were added to dissolve the ammonium salt inside until the solution became homogeneous and the solid stucked at the edges went inside the solution. The reaction mioxture was left overnight under stirring at 100°C. The day after the solution was colourless and the solid inside was yellow. Finally the solid was filtrated

with Buckner under nitrogen, obtaining 30mg of yellow powder (Figure 3.7).

Table 4.19: Chemical conditions for the (PbI_2):($BrF\text{-}N_2$) synthesis.

	Eq.	**MW [g/mol]**	**W [mg]**	**mmol**	**V [μL]**	**M [mmol/mL]**
BrF-N_2	2	847	30	0.035	/	/
PbI_2	1	461	8.16	0.018	/	/
H_2PO_3	45	/	/	/	84	9.4
HI	150	/	/	/	351	7.58

4.2. Characterization

4.2.1. Thin Layer Chromatography (TLC)

TLC was used to qualitative verify the purity of the products before and after Chromatography column. The solution samples were spotted on Silica gel F254, the thin absorber material layer representing the stationary phase, coated onto aluminum sheet substrate. The mobile phase was represented by the samples dissolved in dichloromethane or chloroform. TLC plate was developed under exposure to UV lamp (λ = 254 nm) to detect aromatic species and/or by dipping into potassium permanganate solution to detect the different groups.

4.2.2. Nuclear Magnetic Resonance (NMR)

Brucker Avance III Nanobay 400 MHz and Brucker TopSpin 3.2 were used as instrument and software, respectively, for NMR analysis of samples in solution. Three types of experiments were done: ^{1}H NMR, ^{19}F NMR and ^{13}C NMR. Experiments details are provided in Table 4.20. MestReNova was adopted for elaboration of data, with the eventual help of simulations by Chemdraw.

Table 4.20: NMR experiments parameters.

	^{1}H	^{19}F	^{13}C
Solvent	$CDCl_3$	$CDCl_3$	$CDCl_3$
Size of fid	65 536	562 480	65 536
Temperature [K]	302	305	302
Number of scans	80	8	3072
Relaxation delay [s]	1	2	2
Spectral width [ppm]	20.02541	398.448	238.897
Transmitter frequency offset [ppm]	6.175	-100	99.995

4.2.3. Fourier Transform Infrared (FT-IR) Spectroscopy

Varian 640-IR was used to perform FT-IR measurements. Transmittance scanning type selected with laser wavelength of 632.8 nm. PIKE Technologies MIRacle accessory allowed for attenuated total reflectance (ATR) mode analysis. The samples were placed onto ZnSe crystal plate and pressed hard against it by flat pressure tip. Dry nitrogen was used as

purge gas. Varian Resolution Pro Software was used to elaborate data. Imidazolium salts and perovskite spectra were collected with 64 scans in 400-4000 cm^{-1} wavenumber range. Coating spectra were collected with 512 scans in 400-4000 cm^{-1} wavenumber range.

4.2.4. X-Ray Diffraction (XRD)

The single crystal data of the compounds were collected at 293 K using a Bruker SMART APEX II CCD area detector diffractometer. Data collection, unit cell refinement and data reduction were performed using Bruker SAINT. Powder X-Ray diffraction data of compounds were collected on Bruker AXS D8 powder diffractometer with experimental parameters as follows: Cu-Kα radiation (λ = 1.54056 Å), scanning interval 4-40° at 2θ, step size 0.016°, exposure time 1.5 s per step.

4.2.5. Polarized Optical Microscope (POM)

The crystals and powders textures during phase transitions were studied with an Olympus BX51 polarized optical microscope equipped with a Linkam Scientific LTS 350 heating stage and a Sony CCD-IRIS/RGB video camera. Samples were measured from room T to 250°C with heating and cooling rates of 10°C/min.

4.2.6. Optical Microscope

Binocular Olympus BX41 Microscope was used to verify the crystallinity of single-crystal samples.

4.2.7. Thermogravimetric Analysis (TGA)

TGA was employed to study degradation temperature of samples and to verify their stoichiometry. TA Instruments Q500 and TA Instruments Software were used to perform TGA and to elaborate data. Aluminum standard pans (75 μL) were used for samples insertion in the furnace.

4.2.8. Differential Scanning Calorimetry (DSC)

DSC analyses were performed by Mettler Toledo DSC823^e instrument at a scan rate of 10K/min in sealed aluminum standard crucibles (40 μL) under air. An electrical resistance and nitrogen cooling system controlled the temperature. The furnace temperature was in the maximum range of -225K and 573K for these samples. STAR^e Software (Version 12.10) was used for data elaboration.

4.2.9. Mass Spectroscopy (MS)

The ESI (Electrospray Ionization) MS experiments were performed using a Bruker Esquire 3000 PLUS (ESI Ion Trap LC/MSn System), equipped with an ESI source and a quadrupole ion trap detector (QIT). Some acquisition parameters are 4.5 kV of needle voltage and 40 V of cone voltage, with nitrogen flow rate of 10 L/h. Scan resolution was 13 000 (m/z)/s over the mass range m/z 35–900, obtained by direct infusion of methanol solution (1 mg/1 mL) or dichloromethane (1 mg/1 mL) of compounds at rate 4 μL/min. The assignment of some of species detected was confirmed by collision-activated decomposition (CID) mass spectrometry experiments (MS^2).

4.2.10. Small Angles X-Ray Scattering (SAXS)

Small-angle X-ray scattering (SAXS) measurements were performed to investigate the structure of the imidazolim salts and the perovskites over wide length scales. The X-ray wavelength was λ(Cu Kα2)=1.54 Å. The available q ranges were 0.015 nm^1 < q < 24.189 nm^1, where q is the absolute value of the scattering vector and is defined as $q = (4\pi sin\theta)/\lambda$, and 2θ is the scattering angle. A CCD camera with an image intensifier and an X-ray flat panel sensor were used as detector system for SAXS. Samples were gently pressed and sealed between two aluminium foils, which was then placed onto the hot stage of the microscope mounted on the sample holder on the beamline. The accumulation time required for one measurement for SAXS was 15 min for each sample. The collected scattering intensity data were corrected to remove the contribution of background scattering.

5 | Conclusions

5.1. Conclusions of the experimental work

New lead iodide perovskites containing imidazolium cations decorated with linear (LinF-MImI) or branched (BrF-MImI) fluorinated chains were synthesized and characterized. The X-ray analysis of (PbI_2):(LinF-MImI) single crystals revealed a quasi-0D low - dimensional structure with discrete $(Pb_3I_{12})^{6-}$ anions surrounded by six $(LinF\text{-}MIm)^+$ cations. Within the trinuclear cluster, each Pb^{2+} cation is hexacoordinated by six iodine atoms and adopts a distorted octahedral geometry with a face-sharing connection. Florous-florous interactions result in a partial interdigitation and segregation of fluorinated chains. This interaction pattern promotes the nanoscale separation into a lamellar structure of fluorinated chains and inorganic clusters. Notably, the LinF-MImI salt is a thermotropic liquid crystal with a smectic A phase, and the same behavior is maintained upon incorporation into the perovskite, as demonstrated by DSC, POM, and SAXS analyses. This suggests that the lamellar structure seen in the solid state is preserved even in the molten state and is responsible for the thermotropic liquid crystalline behavior. Formation of a Smectic A phase was observed at 134°C with transition to isotropic liquid at 242°C. For the first time, thermotropic liquid crystalline behavior in bulk low dimensional perovskite was observed and the formation of F···F interactions between fluorinated tails plays a key role in the assembly and stabilization of the observed SmA phases. Starting from these results, a new perovskite containing multibranched fluorinated imidazolium cation was synthesized and characterized as an eco-friendly alternative to perluoroalkyl compounds with linear chains longer than six carbon atoms, whose environmental impact and bioaccumulative potential are of concern. FTIR, NMR, and PXRD analyses confirmed that the reaction between the BrF-MImI salt and lead iodide was successful. Also in this case, POM, DSC and SAXS analysis proved the emergence of a liquid-crystalline behavior, suggesting that the fluorophobic effect and segragation of fluorinated chains should promote the formation of ordered structures with lamellar order. Again, the lamellar order is maintained in the molten state, and a thermotropic liquid crystalline behavior with a Cr-to-LC transition at 65°C and an LC-to-Iso transition at 215°C has been observed. Notably, the Cr-to-LC

transition in the perovskite containing the branched perfluoalkyl imidazolium cation is shifted to much lower temperatures with respect to the (PbI_2):(Linf-MImI) perovskite. Both the perovskites show a high stability in open air at room temperature. Our results pave the way towards new design principles for the construction of thermally stable perovskites endowed with new functional properties.

5.1.1. Future perspectives

To better comprehend the crystalline structure of a perovskite containing a multibranched fluorinated imidazolium cation, its single crystal XRD must be characterized. Furthermore, the presence of fluorinated cations should induce a hydrophobic behavior in these materials, resulting in intriguing properties in terms of moisture resistance of these perovskites; however, contact angle measurements must still be performed. Studying ferromagnetic properties, conductivity and dielectric constant of these quasi-0D perovskites would be also interesting in order to determine how these structural features can affect their electrical properties. These findings initiate a new line of research into the use of perovskite as thermotropic liquid crystals, including the optimization of these materials and their application in optoelectronic or electronic domains, such as polarized light detectors. In order to evaluate this effect, future optoelectronic devices must also undergo stability evaluations. In addition, future research on low-dimensional perovskites must consider these results, particularly the effect of fluorinated chains with various cations on the crystal structure and properties of perovskite lattices. Instead of Pb, non-toxic metals such as Sn could be utilized for the same reactions.
Notewothy, the multibranched fluorinated chain of the imidazolium cation shifted the Cr-to-LC transition to significantly lower temperatures. A further research could be done on perovskites with fluorinated imidazolium cation with a branched group in substitution of the methyl group. If this trend is confirmed, perovskite could be LC at temperatures close to room temperature, making it a more desirable material for optoelectronic applications. In general it would be interesting to determine whether it is possible to establish a design rule according to which it is always possible to obtain LC perovskites when starting with cations that tend to form LC phases. Particularly, the ability to synthesize LC perovskites with nematic phases would be advantageous in terms of the material's conductivity, since nematic LC phase has been already used for example to reorient nanotubes [111] with enhanced performances.

Bibliography

[1] "2022, https://www.whitehouse.gov/build-back-better/.,"

[2] "Renewables 2022 global status report, 2022, https://www.ren21. net/gsr-2022/.,"

[3] "Iea, world energy outlook 2021, 2021, https://www.iea.org/reports/world- energy-outlook-2021 (visited on 10/30/2021,"

[4] M. Petrović, V. Chellappan, and S. Ramakrishna, "Perovskites: solar cells & engineering applications–materials and device developments," *Solar Energy*, vol. 122, pp. 678–699, 2015.

[5] "Nrel. best research cell efficiency chart. https://www.nrel.gov/pv/cell-efficiency.html (accessed august 2019).,"

[6] S. Brittman, G. W. P. Adhyaksa, and E. C. Garnett, "The expanding world of hybrid perovskites: materials properties and emerging applications," *MRS communications*, vol. 5, no. 1, pp. 7–26, 2015.

[7] P. Gao, M. Grätzel, and M. K. Nazeeruddin, "Organohalide lead perovskites for photovoltaic applications," *Energy & Environmental Science*, vol. 7, no. 8, pp. 2448–2463, 2014.

[8] H.-S. Kim, S. H. Im, and N.-G. Park, "Organolead halide perovskite: new horizons in solar cell research," *The Journal of Physical Chemistry C*, vol. 118, no. 11, pp. 5615–5625, 2014.

[9] W. Ke and M. G. Kanatzidis, "Prospects for low-toxicity lead-free perovskite solar cells," *Nature communications*, vol. 10, no. 1, pp. 1–4, 2019.

[10] M. S. Ozório, M. Srikanth, R. Besse, and J. L. Da Silva, "The role of the a-cations in the polymorphic stability and optoelectronic properties of lead-free asni 3 perovskites," *Physical Chemistry Chemical Physics*, vol. 23, no. 3, pp. 2286–2297, 2021.

[11] Y. Liu, Z. Yang, and S. Liu, "Recent progress in single-crystalline perovskite research

including crystal preparation, property evaluation, and applications," *Advanced Science*, vol. 5, no. 1, p. 1700471, 2018.

[12] A. K. Jena, A. Kulkarni, and T. Miyasaka, "Halide perovskite photovoltaics: background, status, and future prospects," *Chemical reviews*, vol. 119, no. 5, pp. 3036–3103, 2019.

[13] D. Liu, Y. Guo, M. Que, X. Yin, J. Liu, H. Xie, C. Zhang, and W. Que, "Metal halide perovskite nanocrystals: application in high-performance photodetectors," *Materials Advances*, vol. 2, no. 3, pp. 856–879, 2021.

[14] J. Chen, S. Zhou, S. Jin, H. Li, and T. Zhai, "Crystal organometal halide perovskites with promising optoelectronic applications," *Journal of Materials Chemistry C*, vol. 4, no. 1, pp. 11–27, 2016.

[15] M. Saliba, S. Orlandi, T. Matsui, S. Aghazada, M. Cavazzini, J.-P. Correa-Baena, P. Gao, R. Scopelliti, E. Mosconi, K.-H. Dahmen, *et al.*, "A molecularly engineered hole-transporting material for efficient perovskite solar cells," *Nature energy*, vol. 1, no. 2, pp. 1–7, 2016.

[16] W. S. Yang, J. H. Noh, N. J. Jeon, Y. C. Kim, S. Ryu, J. Seo, and S. I. Seok, "High-performance photovoltaic perovskite layers fabricated through intramolecular exchange," *Science*, vol. 348, no. 6240, pp. 1234–1237, 2015.

[17] H. Shen, J. Peng, D. Jacobs, N. Wu, J. Gong, Y. Wu, S. K. Karuturi, X. Fu, K. Weber, X. Xiao, *et al.*, "Mechanically-stacked perovskite/cigs tandem solar cells with efficiency of 23.9% and reduced oxygen sensitivity," *Energy & Environmental Science*, vol. 11, no. 2, pp. 394–406, 2018.

[18] J. H. Noh, S. H. Im, J. H. Heo, T. N. Mandal, and S. I. Seok, "Chemical management for colorful, efficient, and stable inorganic–organic hybrid nanostructured solar cells," *Nano letters*, vol. 13, no. 4, pp. 1764–1769, 2013.

[19] Y. Wei, Z. Cheng, and J. Lin, "An overview on enhancing the stability of lead halide perovskite quantum dots and their applications in phosphor-converted leds," *Chemical Society Reviews*, vol. 48, no. 1, pp. 310–350, 2019.

[20] K. Ji, M. Anaya, A. Abfalterer, and S. D. Stranks, "Halide perovskite light-emitting diode technologies," *Advanced Optical Materials*, vol. 9, no. 18, p. 2002128, 2021.

[21] P. Zhu and J. Zhu, "Low-dimensional metal halide perovskites and related optoelectronic applications," *InfoMat*, vol. 2, no. 2, pp. 341–378, 2020.

[22] D.-N. Jeong, J.-M. Yang, and N.-G. Park, "Roadmap on halide perovskite and related devices," *Nanotechnology*, vol. 31, no. 15, p. 152001, 2020.

[23] K. Zhang, N. Zhu, M. Zhang, L. Wang, and J. Xing, "Opportunities and challenges in perovskite led commercialization," *Journal of Materials Chemistry C*, vol. 9, no. 11, pp. 3795–3799, 2021.

[24] J. Lu, C. Yan, W. Feng, X. Guan, K. Lin, and Z. Wei, "Lead-free metal halide perovskites for light-emitting diodes," *EcoMat*, vol. 3, no. 2, p. e12082, 2021.

[25] R. L. Hoye, A. Fakharuddin, D. N. Congreve, J. Wang, and L. Schmidt-Mende, "Light emission from perovskite materials," 2020.

[26] M. Worku, L.-J. Xu, M. Chaaban, A. Ben-Akacha, and B. Ma, "Optically pumped white light-emitting diodes based on metal halide perovskites and perovskite-related materials," *Apl Materials*, vol. 8, no. 1, p. 010902, 2020.

[27] V. Agranovich, D. Basko, G. La Rocca, and F. Bassani, "Excitons and optical nonlinearities in hybrid organic-inorganic nanostructures," *Journal of Physics: Condensed Matter*, vol. 10, no. 42, p. 9369, 1998.

[28] D. Basko, G. La Rocca, F. Bassani, and V. Agranovich, "Förster energy transfer from a semiconductor quantum well to an organic material overlayer," *The European Physical Journal B-Condensed Matter and Complex Systems*, vol. 8, no. 3, pp. 353–362, 1999.

[29] A. F. Akbulatov, L. A. Frolova, N. N. Dremova, I. Zhidkov, V. M. Martynenko, S. A. Tsarev, S. Y. Luchkin, E. Z. Kurmaev, S. M. Aldoshin, K. J. Stevenson, *et al.*, "Light or heat: What is killing lead halide perovskites under solar cell operation conditions?," *The Journal of Physical Chemistry Letters*, vol. 11, no. 1, pp. 333–339, 2019.

[30] A. M. Leguy, Y. Hu, M. Campoy-Quiles, M. I. Alonso, O. J. Weber, P. Azarhoosh, M. Van Schilfgaarde, M. T. Weller, T. Bein, J. Nelson, *et al.*, "Reversible hydration of ch3nh3pbi3 in films, single crystals, and solar cells," *Chemistry of Materials*, vol. 27, no. 9, pp. 3397–3407, 2015.

[31] J. M. Frost, K. T. Butler, F. Brivio, C. H. Hendon, M. Van Schilfgaarde, and A. Walsh, "Atomistic origins of high-performance in hybrid halide perovskite solar cells," *Nano letters*, vol. 14, no. 5, pp. 2584–2590, 2014.

[32] N. Aristidou, C. Eames, I. Sanchez-Molina, X. Bu, J. Kosco, M. S. Islam, and S. A. Haque, "Fast oxygen diffusion and iodide defects mediate oxygen-induced

degradation of perovskite solar cells," *Nature communications*, vol. 8, no. 1, pp. 1–10, 2017.

[33] Y. Han, S. Yue, and B.-B. Cui, "Low-dimensional metal halide perovskite crystal materials: Structure strategies and luminescence applications," *Advanced Science*, vol. 8, no. 15, p. 2004805, 2021.

[34] M. Zhu, C. Li, B. Li, J. Zhang, Y. Sun, W. Guo, Z. Zhou, S. Pang, and Y. Yan, "Interaction engineering in organic–inorganic hybrid perovskite solar cells," *Materials Horizons*, vol. 7, no. 9, pp. 2208–2236, 2020.

[35] J. Kundu and D. K. Das, "Low dimensional, broadband, luminescent organic-inorganic hybrid materials for lighting applications," *European Journal of Inorganic Chemistry*, vol. 2021, no. 44, pp. 4508–4520, 2021.

[36] L. N. Quan, M. Yuan, R. Comin, O. Voznyy, E. M. Beauregard, S. Hoogland, A. Buin, A. R. Kirmani, K. Zhao, A. Amassian, *et al.*, "Ligand-stabilized reduced-dimensionality perovskites," *Journal of the American Chemical Society*, vol. 138, no. 8, pp. 2649–2655, 2016.

[37] C. Zhou, H. Lin, Q. He, L. Xu, M. Worku, M. Chaaban, S. Lee, X. Shi, M.-H. Du, and B. Ma, "Low dimensional metal halide perovskites and hybrids," *Materials Science and Engineering: R: Reports*, vol. 137, pp. 38–65, 2019.

[38] X. Jiang, J. Zhang, S. Ahmad, D. Tu, X. Liu, G. Jia, X. Guo, and C. Li, "Dion-jacobson 2d-3d perovskite solar cells with improved efficiency and stability," *Nano Energy*, vol. 75, p. 104892, 2020.

[39] X. Fu, T. He, S. Zhang, X. Lei, Y. Jiang, D. Wang, P. Sun, D. Zhao, H.-Y. Hsu, X. Li, *et al.*, "Halogen-halogen bonds enable improved long-term operational stability of mixed-halide perovskite photovoltaics," *Chem*, vol. 7, no. 11, pp. 3131–3143, 2021.

[40] M. D. Smith and H. I. Karunadasa, "White-light emission from layered halide perovskites," *Accounts of chemical research*, vol. 51, no. 3, pp. 619–627, 2018.

[41] N. Selivanov, Y. A. Rozhkova, R. Kevorkyants, A. Emeline, and D. Bahnemann, "The effect of organic cations on the electronic, optical and luminescence properties of 1d piperidinium, pyridinium, and 3-hydroxypyridinium lead trihalides," *Dalton Transactions*, vol. 49, no. 14, pp. 4390–4403, 2020.

[42] I. García-Benito, C. Quarti, V. I. Queloz, S. Orlandi, I. Zimmermann, M. Cavazzini, A. Lesch, S. Marras, D. Beljonne, G. Pozzi, *et al.*, "Fashioning fluorous organic

spacers for tunable and stable layered hybrid perovskites," *Chemistry of Materials*, vol. 30, no. 22, pp. 8211–8220, 2018.

[43] V. I. Queloz, M. E. Bouduban, I. García-Benito, A. Fedorovskiy, S. Orlandi, M. Cavazzini, G. Pozzi, H. Trivedi, D. C. Lupascu, D. Beljonne, *et al.*, "Spatial charge separation as the origin of anomalous stark effect in fluorous 2d hybrid perovskites," *Advanced functional materials*, vol. 30, no. 28, p. 2000228, 2020.

[44] L. Wang, Q. Zhou, Z. Zhang, W. Li, X. Wang, Q. Tian, X. Yu, T. Sun, J. Wu, B. Zhang, *et al.*, "A guide to use fluorinated aromatic bulky cations for stable and high-performance 2d/3d perovskite solar cells: The more fluorination the better?," *Journal of Energy Chemistry*, vol. 64, pp. 179–189, 2022.

[45] H.-Y. Zhang, Z.-X. Zhang, X.-J. Song, X.-G. Chen, and R.-G. Xiong, "Two-dimensional hybrid perovskite ferroelectric induced by perfluorinated substitution," *Journal of the American Chemical Society*, vol. 142, no. 47, pp. 20208–20215, 2020.

[46] P.-P. Shi, S.-Q. Lu, X.-J. Song, X.-G. Chen, W.-Q. Liao, P.-F. Li, Y.-Y. Tang, and R.-G. Xiong, "Two-dimensional organic–inorganic perovskite ferroelectric semiconductors with fluorinated aromatic spacers," *Journal of the American Chemical Society*, vol. 141, no. 45, pp. 18334–18340, 2019.

[47] F. Zhang, D. H. Kim, H. Lu, J.-S. Park, B. W. Larson, J. Hu, L. Gao, C. Xiao, O. G. Reid, X. Chen, *et al.*, "Enhanced charge transport in 2d perovskites via fluorination of organic cation," *Journal of the American Chemical Society*, vol. 141, no. 14, pp. 5972–5979, 2019.

[48] M.-H. Tremblay, J. Bacsa, B. Zhao, F. Pulvirenti, S. Barlow, and S. R. Marder, "Structures of (4-y-c6h4ch2nh3) 2pbi4 {Y= H, F, Cl, Br, I}: tuning of hybrid organic inorganic perovskite structures from ruddlesden–popper to dion–jacobson limits," *Chemistry of Materials*, vol. 31, no. 16, pp. 6145–6153, 2019.

[49] M. A. Ruiz-Preciado, D. J. Kubicki, A. Hofstetter, L. McGovern, M. H. Futscher, A. Ummadisingu, R. Gershoni-Poranne, S. M. Zakeeruddin, B. Ehrler, L. Emsley, *et al.*, "Supramolecular modulation of hybrid perovskite solar cells via bifunctional halogen bonding revealed by two-dimensional 19f solid-state nmr spectroscopy," *Journal of the American Chemical Society*, vol. 142, no. 3, pp. 1645–1654, 2020.

[50] B. Luo, Y. Guo, Y. Xiao, X. Lian, T. Tan, D. Liang, X. Li, and X. Huang, "Fluorinated spacers regulate the emission and bandgap of two-dimensional single-layered lead bromide perovskites by hydrogen bonding," *The Journal of Physical Chemistry Letters*, vol. 10, no. 17, pp. 5271–5276, 2019.

[51] X. Li, C. Li, X. Zhao, Y. Zhang, G. Liu, Z. Zhang, D. Wang, L. Xiao, Z. Chen, and B. Qu, "Enhancing the photovoltaic performance and moisture stability of perovskite solar cells via polyfluoroalkylated imidazolium additives," *ACS Applied Materials & Interfaces*, vol. 13, no. 3, pp. 4553–4559, 2021.

[52] R. Atasiei, M. Raicopol, C. Andronescu, A. Hanganu, A. Alexe-Ionescu, and G. Barbero, "Investigation of the conduction properties of ionic liquid crystal electrolyte used in dye sensitized solar cells," *Journal of Molecular Liquids*, vol. 267, pp. 81–88, 2018.

[53] N. Yamanaka, R. Kawano, W. Kubo, T. Kitamura, Y. Wada, M. Watanabe, and S. Yanagida, "Ionic liquid crystal as a hole transport layer of dye-sensitized solar cells," *Chemical communications*, no. 6, pp. 740–742, 2005.

[54] M. Khanmirzaei, S. Ramesh, and K. Ramesh, "Effect of 1-hexyl-3-methylimidazolium iodide ionic liquid on ionic conductivity and energy conversion efficiency of solid polymer electrolyte-based nano-crystalline dye-sensitized solar cells," *Journal of nanoscience and nanotechnology*, vol. 20, no. 4, pp. 2423–2429, 2020.

[55] R. Taniki, N. Kenmochi, K. Matsumoto, and R. Hagiwara, "Effects of the polyfluoroalkyl side-chain on the properties of 1-methyl-3-polyfluoroalkylimidazolium fluorohydrogenate ionic liquids," *Journal of Fluorine Chemistry*, vol. 149, pp. 112–118, 2013.

[56] G. Cavallo, A. Abate, M. Rosati, G. Paolo Venuti, T. Pilati, G. Terraneo, G. Resnati, and P. Metrangolo, "Tuning of ionic liquid crystal properties by combining halogen bonding and fluorous effect," *ChemPlusChem*, vol. 86, no. 3, pp. 469–474, 2021.

[57] S. Yamada, K. Kinoshita, S. Iwama, T. Yamazaki, T. Kubota, T. Yajima, K. Yamamoto, and S. Tahara, "Synthesis of perfluoroalkylated pentacenes and evaluation of their fundamental physical properties," *Organic & Biomolecular Chemistry*, vol. 15, no. 12, pp. 2522–2535, 2017.

[58] A. G. Tomulescu, L. N. Leonat, F. Neațu, V. Stancu, V. Toma, S. Derbali, Neațu, A. M. Rostas, C. Beșleagă, R. Pătru, *et al.*, "Enhancing stability of hybrid perovskite solar cells by imidazolium incorporation," *Solar Energy Materials and Solar Cells*, vol. 227, p. 111096, 2021.

[59] M. Salado, F. J. Ramos, V. M. Manzanares, P. Gao, M. K. Nazeeruddin, P. J. Dyson, and S. Ahmad, "Extending the lifetime of perovskite solar cells using a perfluorinated dopant," *ChemSusChem*, vol. 9, no. 18, pp. 2708–2714, 2016.

[60] X. Zhu, M. Du, J. Feng, H. Wang, Z. Xu, L. Wang, S. Zuo, C. Wang, Z. Wang, C. Zhang, *et al.*, "High-efficiency perovskite solar cells with imidazolium-based ionic liquid for surface passivation and charge transport," *Angewandte Chemie International Edition*, vol. 60, no. 8, pp. 4238–4244, 2021.

[61] C. Luo, G. Li, L. Chen, J. Dong, M. Yu, C. Xu, Y. Yao, M. Wang, Q. Song, and S. Zhang, "Passivation of defects in inverted perovskite solar cells using an imidazolium-based ionic liquid," *Sustainable Energy & Fuels*, vol. 4, no. 8, pp. 3971–3978, 2020.

[62] S. Bai, P. Da, C. Li, Z. Wang, Z. Yuan, F. Fu, M. Kawecki, X. Liu, N. Sakai, J. T.-W. Wang, *et al.*, "Planar perovskite solar cells with long-term stability using ionic liquid additives," *Nature*, vol. 571, no. 7764, pp. 245–250, 2019.

[63] Q. Wang, F. Lin, C.-C. Chueh, T. Zhao, M. Eslamian, and A. K.-Y. Jen, "Enhancing efficiency of perovskite solar cells by reducing defects through imidazolium cation incorporation," *Materials today energy*, vol. 7, pp. 161–168, 2018.

[64] B. Saparov and D. B. Mitzi, "Organic–inorganic perovskites: structural versatility for functional materials design," *Chemical reviews*, vol. 116, no. 7, pp. 4558–4596, 2016.

[65] C. Seth, D. Jana, V. Jindal, D. Khushalani, and S. Ghosh, "One-dimensional behavior of imidazolium lead iodide," *The Journal of Physical Chemistry C*, vol. 123, no. 26, pp. 16449–16455, 2019.

[66] A. Thirumurugan and C. Rao, "Supramolecular organization in lead bromide salts of imidazolium-based ionic liquids," *Crystal Growth and Design*, vol. 8, no. 5, pp. 1640–1644, 2008.

[67] F. Coleman, G. Feng, R. W. Murphy, P. Nockemann, K. R. Seddon, and M. Swadźba-Kwaśny, "Lead (ii) chloride ionic liquids and organic/inorganic hybrid materials–a study of chloroplumbate (ii) speciation," *Dalton Transactions*, vol. 42, no. 14, pp. 5025–5035, 2013.

[68] M. Shi, S.-S. Yu, H. Zhang, S.-X. Liu, and H.-B. Duan, "A hybrid molecular rotor crystal with dielectric relaxation and thermochromic luminescence," *Journal of Molecular Structure*, vol. 1206, p. 127650, 2020.

[69] S.-S. Yu, S.-X. Jiang, H. Zhang, and H.-B. Duan, "Crystal structural and thermochromic luminescence properties modulation by ion liquid cations in bromo-

plumbate perovskites," *Inorganic Chemistry Communications*, vol. 112, p. 107690, 2020.

[70] K.-M. Wan, Y.-B. Tong, Y. Zou, H.-B. Duan, J.-L. Liu, X.-M. Ren, *et al.*, "Investigation of thermochromic photoluminescent, dielectric and crystal structural properties for an inorganic–organic hybrid solid of [1-hexyl-3-methylimidazolium][pbbr 3]," *New Journal of Chemistry*, vol. 40, no. 10, pp. 8664–8672, 2016.

[71] I. Tirotta, A. Mastropietro, C. Cordiglieri, L. Gazzera, F. Baggi, G. Baselli, M. G. Bruzzone, I. Zucca, G. Cavallo, G. Terraneo, *et al.*, "A superfluorinated molecular probe for highly sensitive in vivo 19f-mri," *Journal of the American Chemical Society*, vol. 136, no. 24, pp. 8524–8527, 2014.

[72] Z.-X. Jiang and Y. B. Yu, "The design and synthesis of highly branched and spherically symmetric fluorinated oils and amphiles," *Tetrahedron*, vol. 63, no. 19, pp. 3982–3988, 2007.

[73] G. Pozzi, S. Quici, M. C. Raffo, C. A. Bignozzi, S. Caramori, and M. Orlandi, "Fluorous molecules for dye-sensitized solar cells: synthesis and photoelectrochemistry of unsymmetrical zinc phthalocyanine sensitizers with bulky fluorophilic donor groups," *The Journal of Physical Chemistry C*, vol. 115, no. 9, pp. 3777–3788, 2011.

[74] S. Decato, T. Bemis, E. Madsen, and S. Mecozzi, "Synthesis and characterization of perfluoro-tert-butyl semifluorinated amphiphilic polymers and their potential application in hydrophobic drug delivery," *Polymer chemistry*, vol. 5, no. 22, pp. 6461–6471, 2014.

[75] H. Jiang, P. Taranekar, J. R. Reynolds, and K. S. Schanze, "Conjugated polyelectrolytes: synthesis, photophysics, and applications," *Angewandte Chemie International Edition*, vol. 48, no. 24, pp. 4300–4316, 2009.

[76] M. B. Taraban, L. Yu, Y. Feng, E. V. Jouravleva, M. A. Anisimov, Z.-X. Jiang, and Y. B. Yu, "Conformational transition of a non-associative fluorinated amphiphile in aqueous solution," *RSC Advances*, vol. 4, no. 97, pp. 54565–54575, 2014.

[77] M. B. Taraban, D. J. Deredge, M. E. Smith, K. T. Briggs, Y. Li, Z.-X. Jiang, P. L. Wintrode, and Y. B. Yu, "Monitoring dendrimer conformational transition using 19f and 1h2o nmr," *Magnetic Resonance in Chemistry*, vol. 57, no. 10, pp. 861–872, 2019.

[78] A. M. Huynh, A. Müller, S. M. Kessler, S. Henrikus, C. Hoffmann, A. K. Kiemer,

A. Bücker, and G. Jung, "Small bodipy probes for combined dual 19f mri and fluorescence imaging," *ChemMedChem*, vol. 11, no. 14, pp. 1568–1575, 2016.

[79] H. Shi, B. Lai, S. Chen, X. Zhou, J. Nie, and J.-A. Ma, "Facile synthesis of novel perfluorocarbon-modulated 4-anilinoquinazoline analogues," *Chinese Journal of Chemistry*, vol. 35, no. 11, pp. 1693–1700, 2017.

[80] V. Dichiarante, I. Tirotta, L. Catalano, G. Terraneo, G. Raffaini, M. R. Chierotti, R. Gobetto, F. B. Bombelli, and P. Metrangolo, "Superfluorinated and nir-luminescent gold nanoclusters," *Chemical Communications*, vol. 53, no. 3, pp. 621–624, 2017.

[81] Q. Peng, Y. Li, S. Bo, Y. Yuan, Z. Yang, S. Chen, X. Zhou, and Z.-X. Jiang, "Paramagnetic nanoemulsions with unified signals for sensitive 19f mri cell tracking," *Chemical communications*, vol. 54, no. 47, pp. 6000–6003, 2018.

[82] S. Bo, Y. Yuan, Y. Chen, Z. Yang, S. Chen, X. Zhou, and Z.-X. Jiang, "In vivo drug tracking with 19 f mri at therapeutic dose," *Chemical Communications*, vol. 54, no. 31, pp. 3875–3878, 2018.

[83] H. Zhang, S. Bo, K. Zeng, J. Wang, Y. Li, Z. Yang, X. Zhou, S. Chen, and Z.-X. Jiang, "Fluorinated porphyrin-based theranostics for dual imaging and chemo-photodynamic therapy," *Journal of Materials Chemistry B*, vol. 8, no. 20, pp. 4469–4474, 2020.

[84] M. I. Martinez Espinoza, L. Sori, A. Pizzi, G. Terraneo, I. Moggio, E. Arias, G. Pozzi, S. Orlandi, V. Dichiarante, P. Metrangolo, *et al.*, "Bodipy dyes bearing multibranched fluorinated chains: Synthesis, structural, and spectroscopic studies," *Chemistry–A European Journal*, vol. 25, no. 38, pp. 9078–9087, 2019.

[85] O. Munkhbat, M. Canakci, S. Zheng, W. Hu, B. Osborne, A. A. Bogdanov, and S. Thayumanavan, "19f mri of polymer nanogels aided by improved segmental mobility of embedded fluorine moieties," *Biomacromolecules*, vol. 20, no. 2, pp. 790–800, 2018.

[86] T. Niu, L. Chao, W. Gao, C. Ran, L. Song, Y. Chen, L. Fu, and W. Huang, "Ionic liquids-enabled efficient and stable perovskite photovoltaics: progress and challenges," *ACS Energy Letters*, vol. 6, no. 4, pp. 1453–1479, 2021.

[87] M. Kumar and S. Kumar, "Liquid crystals in photovoltaics: a new generation of organic photovoltaics," *Polymer Journal*, vol. 49, no. 1, pp. 85–111, 2017.

[88] A. Abate, A. Petrozza, G. Cavallo, G. Lanzani, F. Matteucci, D. W. Bruce,

N. Houbenov, P. Metrangolo, and G. Resnati, "Anisotropic ionic conductivity in fluorinated ionic liquid crystals suitable for optoelectronic applications," *Journal of Materials Chemistry A*, vol. 1, no. 22, pp. 6572–6578, 2013.

[89] V. Dichiarante, M. I. Martinez Espinoza, L. Gazzera, M. Vuckovac, M. Latikka, G. Cavallo, G. Raffaini, R. Oropesa-Nuñez, C. Canale, S. Dante, *et al.*, "A short-chain multibranched perfluoroalkyl thiol for more sustainable hydrophobic coatings," *Acs Sustainable Chemistry & Engineering*, vol. 6, no. 8, pp. 9734–9743, 2018.

[90] C. Seth and D. Khushalani, "Non-perovskite hybrid material, imidazolium lead iodide, with enhanced stability," *ChemNanoMat*, vol. 5, no. 1, pp. 85–91, 2019.

[91] W. A. Hendrickson, "Synchrotron crystallography," *Trends in biochemical sciences*, vol. 25, no. 12, pp. 637–643, 2000.

[92] "https://www.diamond.ac.uk/home/about/faqs/about-synchrotrons.html.,"

[93] B. Haddad, D. Mokhtar, M. Goussem, E.-h. Belarbi, D. Villemin, S. Bresson, M. Rahmouni, N. R. Dhumal, H. J. Kim, and J. Kiefer, "Influence of methyl and propyl groups on the vibrational spectra of two imidazolium ionic liquids and their non-ionic precursors," *Journal of Molecular Structure*, vol. 1134, pp. 582–590, 2017.

[94] Y. Jeon, J. Sung, C. Seo, H. Lim, H. Cheong, M. Kang, B. Moon, Y. Ouchi, and D. Kim, "Structures of ionic liquids with different anions studied by infrared vibration spectroscopy," *The Journal of Physical Chemistry B*, vol. 112, no. 15, pp. 4735–4740, 2008.

[95] I. Jerman, V. Jovanovski, A. Š. Vuk, S. Hočevar, M. Gaberšček, A. Jesih, and B. Orel, "Ionic conductivity, infrared and raman spectroscopic studies of 1-methyl-3-propylimidazolium iodide ionic liquid with added iodine," *Electrochimica Acta*, vol. 53, no. 5, pp. 2281–2288, 2008.

[96] J. Kiefer, J. Fries, and A. Leipertz, "Experimental vibrational study of imidazolium-based ionic liquids: Raman and infrared spectra of 1-ethyl-3-methylimidazolium bis (trifluoromethylsulfonyl) imide and 1-ethyl-3-methylimidazolium ethylsulfate," *Applied spectroscopy*, vol. 61, no. 12, pp. 1306–1311, 2007.

[97] W. Yang, X. Cheng, H. Wang, Y. Liu, and Z. Du, "Surface and mechanical properties of waterborne polyurethane films reinforced by hydroxyl-terminated poly (fluoroalkyl methacrylates)," *Polymer*, vol. 133, pp. 68–77, 2017.

[98] G. Socrates, *Infrared and Raman characteristic group frequencies: tables and charts*. John Wiley & Sons, 2004.

[99] L. Dimesso, A. Quintilla, Y.-M. Kim, U. Lemmer, and W. Jaegermann, "Investigation of formamidinium and guanidinium lead tri-iodide powders as precursors for solar cells," *Materials Science and Engineering: B*, vol. 204, pp. 27–33, 2016.

[100] M. Acik, T. M. Alam, F. Guo, Y. Ren, B. Lee, R. A. Rosenberg, J. F. Mitchell, I. K. Park, G. Lee, and S. B. Darling, "Substitutional growth of methylammonium lead iodide perovskites in alcohols," *Advanced Energy Materials*, vol. 8, no. 5, p. 1701726, 2018.

[101] C. Worsley, D. Raptis, S. Meroni, A. Doolin, R. Garcia-Rodriguez, M. Davies, and T. Watson, "γ-valerolactone: A nontoxic green solvent for highly stable printed mesoporous perovskite solar cells," *Energy Technology*, vol. 9, no. 7, p. 2100312, 2021.

[102] G. Nagabhushana, R. Shivaramaiah, and A. Navrotsky, "Direct calorimetric verification of thermodynamic instability of lead halide hybrid perovskites," *Proceedings of the National Academy of Sciences*, vol. 113, no. 28, pp. 7717–7721, 2016.

[103] G. Singh, S. Kumar, and S.-W. Kang, "Structures: Liquid crystals," in *Reference Module in Materials Science and Materials Engineering*, Elsevier, 2016.

[104] T. Li, A. J. Senesi, and B. Lee, "Small angle x-ray scattering for nanoparticle research," *Chemical reviews*, vol. 116, no. 18, pp. 11128–11180, 2016.

[105] B. Chu and B. S. Hsiao, "Small-angle x-ray scattering of polymers," *Chemical reviews*, vol. 101, no. 6, pp. 1727–1762, 2001.

[106] A. Bradley, C. Hardacre, J. Holbrey, S. Johnston, S. McMath, and M. Nieuwenhuyzen, "Small-angle x-ray scattering studies of liquid crystalline 1-alkyl-3-methylimidazolium salts," *Chemistry of materials*, vol. 14, no. 2, pp. 629–635, 2002.

[107] S. Das, N. Kashyap, S. Kalita, D. B. Bora, and R. Borah, "A brief insight into the physicochemical properties of room-temperature acidic ionic liquids and their catalytic applications in cc bond formation reactions," *Advances in Physical Organic Chemistry*, vol. 54, pp. 1–98, 2020.

[108] S. J. Williams and R. V. Stick, *Carbohydrates: The Essential Molecules of Life Ed. 2*. Elsevier Science, 2009.

[109] W. Q. Tian and Y. A. Wang, "Mechanisms of staudinger reactions within density functional theory," *The Journal of organic chemistry*, vol. 69, no. 13, pp. 4299–4308, 2004.

[110] F. L. Lin, H. M. Hoyt, H. van Halbeek, R. G. Bergman, and C. R. Bertozzi, "Mechanistic investigation of the staudinger ligation," *Journal of the American Chemical Society*, vol. 127, no. 8, pp. 2686–2695, 2005.

[111] I. Dierking, G. Scalia, P. Morales, and D. LeClere, "Aligning and reorienting carbon nanotubes with nematic liquid crystals," *Advanced materials*, vol. 16, no. 11, pp. 865–869, 2004.

A | Appendix A

Table A.1: Crystal data for the (PbI_2):(LinF-MImI) perovskite.

(PbI_2):(LinF-MImI)	
Chemical formula	$(C_9F_{13}MIm)_6(Pb_3I_{12})$
Formula weight	7623
Temperature	296.15 K
Space group	P1
a	11.299 Å
b	19.471 Å
c	30.997 Å
α	98.55°
β	93.18°
γ	98.77°
Volume	6602.3 $Å^3$

List of Figures

List of Tables

Acknowledgements

First of all, a special thanks to Prof. Gabriella Cavallo who guided me throughout this research work with her advices and assistance. I would like also to thank prof. Giancarlo Terraneo, prof. Francesca Baldelli, and prof. Pierangelo Metrangolo for their precious contributions. Finally, I want to express my heartfelt gratitude to Anastasios Stergiou, Marta Rosati and all the other members of the SBNlab with whom I had the pleasure of working; they are all helpful and friendly people capable of creating a positive working atmosphere. I wish them the best for the future.